Numerical simulations of the Lattice Boltzmann method for determination of hydrodynamic properties of fractal aggregates

Nguyen, Phi Hung

UNIVERSITÉ DE GENÈVE — FACULTÉ DES SCIENCES

Département d'informatique — Professeur B. Chopard

Département de chimie minérale, analytique et appliquée (CABE) — Docteur S. Stoll

Numerical Simulations of the Lattice Boltzmann Method for Determination of Hydrodynamic Properties of Fractal Aggregates

THÈSE

présentée à la Faculté des sciences de Université de Genève
pour obtenir le grade de Docteur ès sciences, mention interdisciplinaire

par

NGUYEN Phi Hung

de

Hanoi (Vietnam)

Thèse N° 3877

GENÈVE
Atelier de reprodution de la Section de physique
2007

La Faculté des sciences, sur le préavis de Messieurs B. CHOPARD, professeur adjoint et directeur de thèse (Département d'informatique), S.STOLL, docteur et co-directeur de thèse (Département de chimie minérale, analytique et appliquée), J. BUFFLE, professeur ordinaire (Département de chimie minérale, analytique et appliquée), et S. DURAND VIDAL, docteur (Université Pierre & Marie Curie - Paris, France), autorise l'impression de la présente thèse, sans exprimer d'opinion sur les propositions qui y sont énoncées.

Genève, le 11 juillet 2007

Thèse - 3877 -

Acknowledgment

During this work, I was supported by many people that I would like to thank them all.
First, I sincerely thank my supervisors, Prof. Bastien Chopard and Dr. Serge Stoll, for their tremendous and continuous helps in my work. They both offered me a motivating environment and valuable discussions to fulfill the research.
I would like to thank Davide Alemani for sharing with me a friendly and unforgettable time in office 302 with a lot coffee and for his Italian lards. I thank Vincent Keller for the nice time he shared the office with us. I would like to thank Alexandre Dupuis for his first lesson in the lattice Boltzmann method at the beginning of my thesis.
I would like to take this chance to thank Dr. Serge Durand Vidal and Prof. Jacques Buffle for accepting to be the members of my jury.
I also thank all other colleagues of SPC and CABE group for all their helps in different ways during my thesis. I would therefore like to thank David Kony, Jonas Latt, Bernhard Sonderegger, Andrea Parmigiani, Marianne Seijo, Serge Ulrich, Parthasarathy Nalini.
And last but not least, I thank my dear Fred Isler for always standing beside me when in need as a second father to take care of me. I specially thank my parents, my sister and my dear Hanh for what they have done and supported. Special love to my dear "Tho già" Minh-Anh whose smiles always make me happy and my life more beautiful.

Contents

List of Figures

List of Tables

Résumé en français

Ce travail de thèse a porté sur le développement et l'utilisation de simulations numériques par la méthode de Boltzmann sur réseau (Lattice Boltzmann) pour l'étude des propriétés hydrodynamiques d'agrégats fractals. Les agrégats fractals sont des objets composés de particules élémentaires qui suite à leur diffusion et collage sous l'influence de forces attractives forment des structures complexes. Il s'agit d'un travail interdisciplinaire qui concerne à la fois la physico-chimie de l'environnement, plus particulièrement l'étude du comportement de la matière colloïdale en suspension, et la modélisation informatique dans le cadre du développement de modèles numériques pour étudier les interactions fluide-solides complexes.
Le but du travail de thèse a consisté à déterminer par simulations numériques les paramètres qui influencent les vitesses de sédimentation d'agrégats colloïdaux de type fractal en se focalisant sur leurs propriétés géométriques et hydrodynamiques. C'est un problème de très grande importance en physico-chimie de l'environnement qui contribue au fonctionnement des écosystèmes aquatiques et conditionne les processus de production d'eau potable. L'idée générale consiste à rapidement former de larges agrégats qui seront ensuite éliminés des colonnes d'eau.

L'introduction (chapitre 1) présente l'ensemble des problèmes importants qui permettent de bien situer l'étude dans son cadre général et montre que la détermination des propriétés hydrodynamiques d'agrégats fractals est essentielle pour élucider leurs rôles dans les milieux naturels et que cette problématique peut être avantagement abordée sur la base de simulations numériques en particulier les modèles du type Lattice Boltzmann.

Dans le chapitre 2, le travail se concentre sur la notion de dimension fractale, une description des agrégats fractals et de leurs propriétés géométriques. Des exemples d'agrégats fractals qui couvrent les fractales régulières, irrégulières et les différents types d'agrégats que l'on peut obtenir en fonction des mécanismes d'agrégation que l'on retrouve dans les systèmes naturels sont donnés.
L'importance des préfacteurs dans les lois d'échelle qui permettent de relier la masse des agrégats, à leurs dimensions géométriques au travers de la dimension

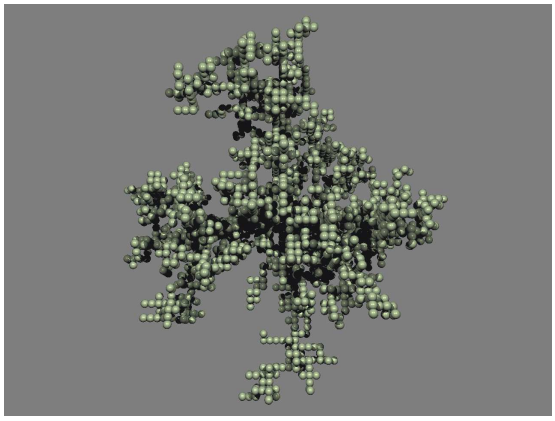

Figure 1: Agrégat autosimilaire du type Witten-Sander constitué de 3000 particules élémentaires et de dimension fractale 2.49

fractale est abordée. C'est un point important qui permet de faire un lien quantitatif entre tous les paramètres géométriques qui permettent de décrire un agrégat fractal malheureusement souvent passé sous silence dans la littérature. Une description des différents modèles d'agrégation, à savoir le modèle de la particule et du germe et le modèle d'autoassemblage d'agrégats est présentée. Nous discutons ensuite les principaux modèles de la littérature pour l'étude de la relation entre le rayon de giration des agrégats Rg et le rayon hydrodynamique Rh. En comparant les différentes valeurs du rapport $\frac{R_h}{R_g}$ trouvées dans la littérature nous avons pu clairement mettre en avant, au regard de la polydispersité des valeurs que la détermination des propriétés hydrodynamiques restait un problème ardu et ouvert que se soit au niveau numérique (dans le choix des tenseurs d'interaction hydrodynamique) ou au niveau expérimental afin d'établir la relation entre vitesse de sédimentation et structure fractale.

Dans le chapitre 3 nous discutons de la dynamique des fluides (notion de flux uniforme et non uniforme, de flux compressible et incompréssible, de flux laminaire et turbulent, de fluide newtonien et non newtonien, définition du nombre de Reynolds, équation de Navier-Stokes) et abordons les aspects théoriques nécessaires pour aborder un sujet somme toute assez vaste et complexe tout en discutant l'exemple du profil de Poiseuille.

Dans le chapitre 4 nous discutons en détail la méthode Lattice Boltzmann pour la simulation des fluides ainsi que les paramètres et les choix effectués dans le cadre de ce travail. Les différents modèles de réseaux sont présentés tout en discutant leurs avantages et inconvénients et les règles de collision sont établies. Les choix concernant la paramétrisation de notre modèle, en terme de déplacement

du fluide, de géométrie de réseau, l'importance des conditions périodiques, des sources d'erreurs liées par exemple à la discrétisation des agrégats sont discutés en détail. En particulier l'effet de la discrétisation sur un réseau carré d'une sphère est évalué en utilisant deux modèles de réseaux. Nous démontrons que la prèsence de frontières en bordures de simulations présente inévitablement des sources d'erreurs qu'il convient d'évaluer pour chaque modèle de simulations. Nous montrons qu'en respectivement deux et trois dimensions les modèles D2Q9 et D3Q15 constituent des choix raisonnables en terme de résolution et temps de calculs.

Le chapitre 5 concerne l'application des simulations Lattice Boltzmann pour la détermination des propriétés hydrodynamiques d'agrégats fractals en deux dimensions. Dans un premier temps, le passage d'un fluide à travers un réseau de disques est abordé ce qui permet de confronter le modèle utilisé avec une solution analytique, celle de Sangani et al.

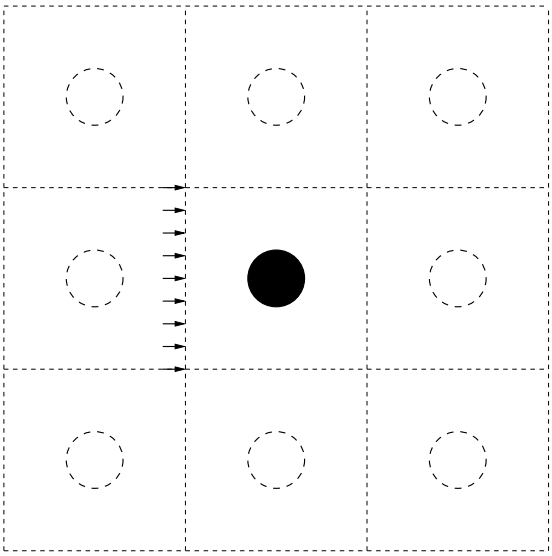

Figure 2: Passage d'un fluide à travers un réseau de cylindres

La méthode de calcul de la force de traînée, élément clef de ce travail, est discutée à ce moment là. Avant d'effectuer des calculs sur des agrégats fractals, l'influence de la description des particules élémentaires composant les agrégats sous la forme d'un point ou d'un ensemble de points est étudiée. Nous montrons qu'à partir du moment où la taille de l'agrégat est suffisamment grande par rapport à la taille de ses grains élémentaires, l'agrégat peut être assimilé à un assemblage de points de réseau. Dans un troisième temps les simulations sont effectuées sur des agrégats fractals en deux dimensions. Nos simulations permettent de montrer qu'afin d'établir le lien avec la solution analytique, il

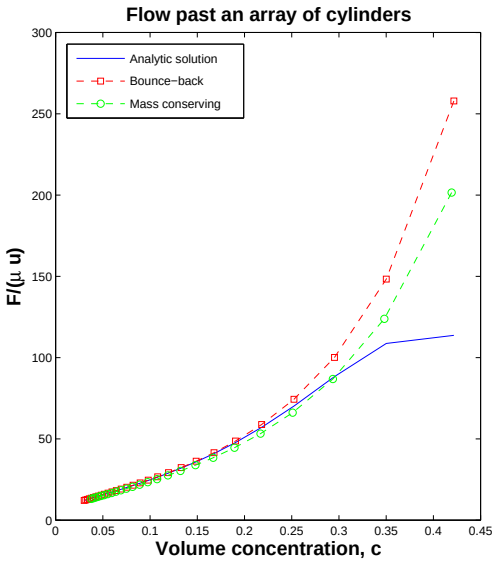

Figure 3: Variation de la force de trainée en fonction de la concentration volumique

est nécessaire d'introduire un facteur d'échelle qui permet de remonter au rayon hydrodynamique des agrégats fractals. Dans le cas d'agrégats du type Witten et Sanders, l'analyse de la variation du rapport $\frac{R_h}{R_g}$ est effectuée. Les résultats suggèrent que la dimension fractale n'intervient pas dans le le rapport $\frac{R_h}{R_g}$ mais aucune conclusion définitive ne peut être clairement établie, probablement en raison de l'effet important de l'orientation et anisotropie relative des structures utilisées.

Dans le chapitre 6 nous discutons du comportement d'agrégats 3D et tirons des conclusions directes quant au rôle de la dimension fractale. Dans un premier temps le comportement d'un réseau de sphères est comparé avec la solution analytique d'Hasimoto-Sangani. L'importance de la discrétisation des sphères et les domaines de validité en fraction volumique sont analysés. Dans un deuxième temps, les calculs effectués sur des agrégats fractals mettent en évidence que deux paramètres d'échelle sont nécessaires afin de s'accorder à la solution analytique. Le premier permet d'établir la valeur du rayon hydrodynamique tandis que le second permet de mesurer le volume effectif de l'agrégat dans lequel la vitesse du fluide est égale à zéro.

Un autre résultat important concerne la variation du rapport $\frac{R_h}{R_g}$ en fonction de

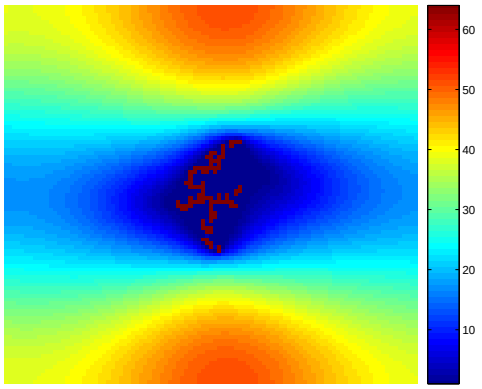

Figure 4: Passage d'un fluide à travers un agrégat fractal

la masse des agrégats. Nous démontrons que ce rapport n'est pas sensible à la masse des agrégats ce qui constitue un résultat très important. L'importance des préfacteurs γ_g et γ_h dans le calcul du rapport $\frac{R_h}{R_g}$ est ensuite mise en évidence ainsi que celui de la connectivité des agrégats.
En générant des agrégats artificiels, dont nous pouvons ajuster la dimension fractale et la valeur des préfacteurs dans les relations reliant le nombre de particules élémentaires aux dimensions géométriques et dimensions fractales des agrégats, nous avons établi que deux agrégats de même dimension fractale mais de connectivité différente possèderont des propriétés hydrodynamiques différentes.

C'est un résultat fondamental et qui va un peu à l'encontre d'idées reçues. D'autre part une analyse plus détaillée et explicite de la variation du rapport Rg/Rh en fonction des dimensions fractales et de la taille des agrégats figure dans l'appendice C. Il est à noter que des centaines d'agrégats auront été nécessaires dans le cadre de cette étude.

Dans le chapitre 7 nous nous intéressons au rôle de la perméabilité des agrégats et sa variation à l'intérieur de ces derniers. Sur la base d'un modèle mathématique développé par Veerapaneni, basé sur l'image d'une sphère solide entourée d'une couronne poreuse, en supposant que la viscosité effective est égale à la viscosité du fluide et que la perméabilité varie radialement selon le modèle de Happel, nous montrons que le rayon hydrodynamique calculé est en bon accord avec celui déterminé par simulations numériques. A partir des simulations, les mesures de la viscosité intrinsèque et de la perméabilité, montrent que l'équation de Darcy est certainement plus adaptée que l'équation de Brinkman pour décrire le com-

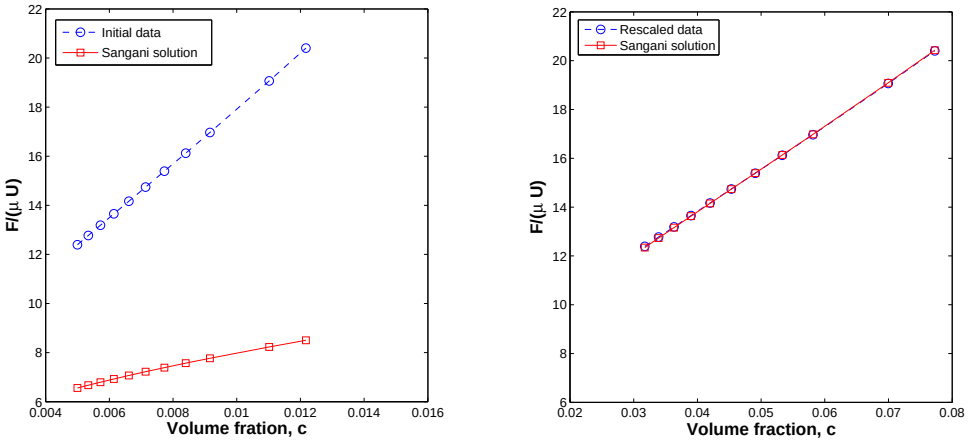

Figure 5: LB simulation pour un agrégat du type RLA (gauche) et comparaison après scaling avec la solution analytique de Sangani-Acrivos

portement du fluide à l'intérieur de la structure fractale.

Le chapitre 8 clôt cette thèse en donnant un aperçu des différents développements et perspectives possibles. Finalement, dans les appendices nous trouvons une description mathématique détaillée des rayons caractéristiques des agrégats, des calculs concernant les erreurs que l'on retrouve en deux dimensions sur les règles de collision, les valeurs des rapports Rg/Rh pour toutes les simulations effectuées, le modèle et sa résolution mathématique de perméabilité non uniforme à l'intérieur des agrégats.

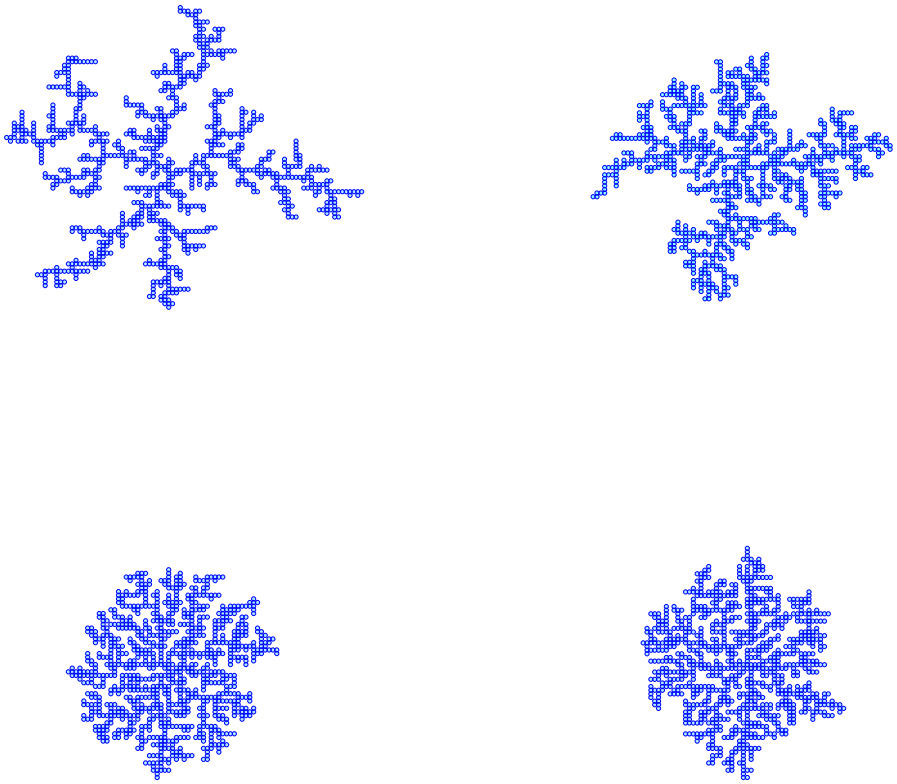

Figure 6: Exemples d'agrégats du type Witten et Sanders obtenus pour différentes dimensions fractales

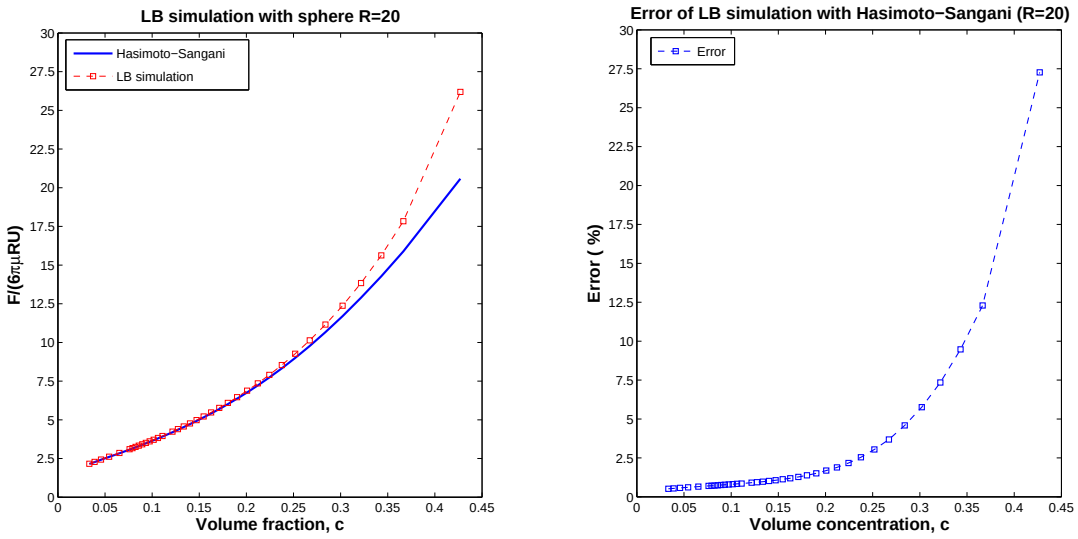

Figure 7: Comparaison de résultats issus de simulations avec la solution analytique et estimation de l'erreur sur le calcul de la force de trainée en fonction de la concentration volumique.

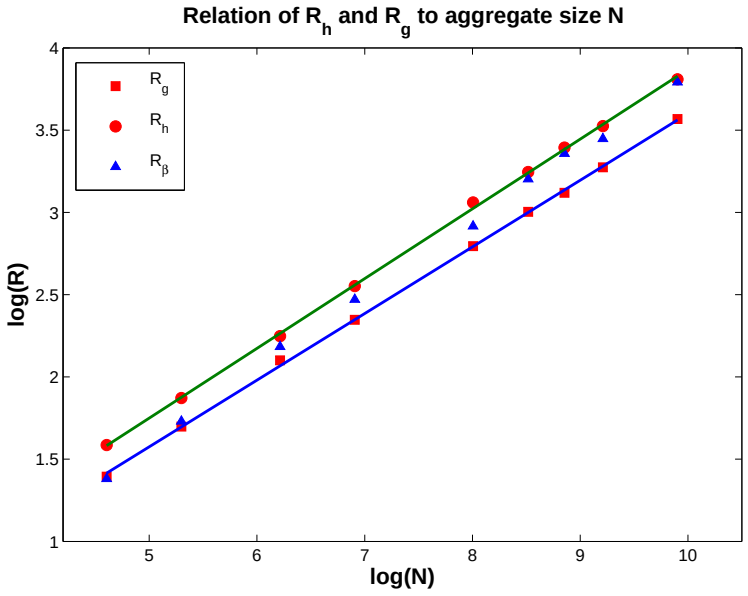

Figure 8: Représentation de la variation du rayon hydrodynamique, rayon de giration en fonction de la masse des agrégats de dimension fractale égale à 2.49

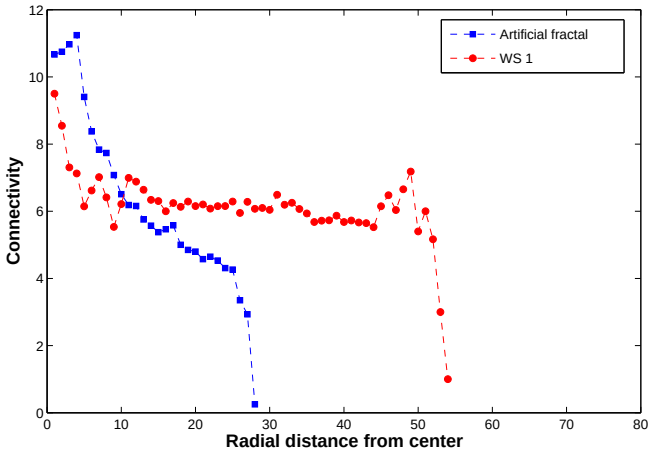

Figure 9: Variation de la connectivité en fonction de la distance radiale au centre de masse pour un agrégat du type Witten et Sanders et un agrégat artificiel de même dimension fractale et valeur de préfacteur

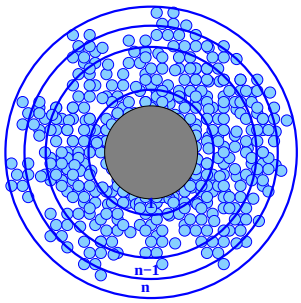

Figure 10: Modèle de perméabilité pour un agrégat fractal (noyau imperméable entouré d'une couronne poreuse).

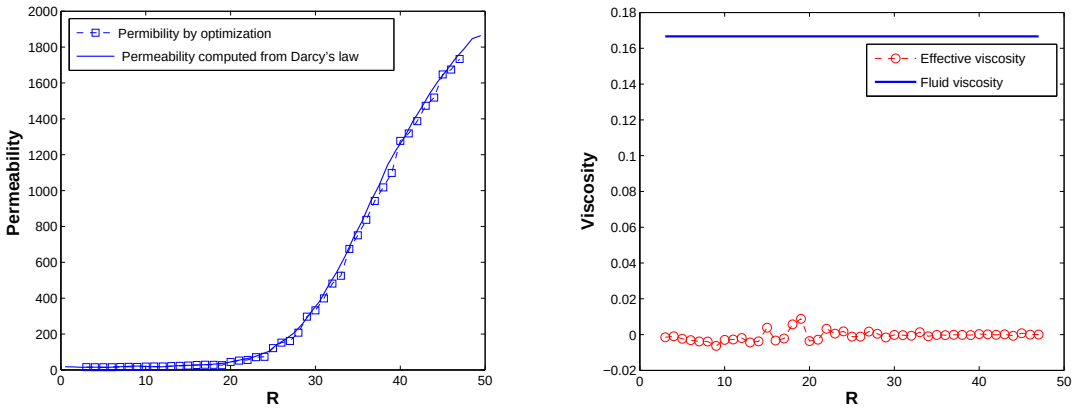

Figure 11: Variation de la perméabilité et viscosité en fonction du rayon à l'intérieur d'une structure fractale

Chapter 1

Introduction

The world of nature contains a huge number of mysteries behind various physical processes happening around us. For many common processes, which we accept as usual phenomena, we may not have exact explanations. The study of physical processes has been a main topic of natural science which is involved in using different sources of knowledge. Environmental processes and bio-chemical processes are among the most common that we can find frequently in our daily life. One of the most important environmental processes, the sedimentation rate of flocculated materials and aggregates has attracted attention of scientists. There are two main reasons for this. The first is for the rational design or the effective operation of water treatment and the second is for the prediction of suspended matter diffusion, sediment fluxes and particle residence time in aquatic systems. Hydrodynamic properties of natural aggregates (or fractal aggregates) are in most cases very complex and ill understood.
To understand the sedimentation process of fractal aggregates and flocculated material and their hydrodynamic properties, one can experimentally measure the quantities of interest, then use mathematical and physical knowledge to build a theory or a model to enable further predictions. However, such work is not always possible. For example, the mathematical equations applied to model settling velocities are usually based on the descriptions of the settling materials (mainly aggregates composed of inorganic particles) as permeable or impermeable spheres using relationships derived from Stokes' Law. Nevertheless, experimental results for settling rates of aggregates clearly demonstrate that, natural aggregates settle 5-10 times faster than those predicted by mathematical models, the deviations being most pronounced for less dense structures. Even after accounting for aggregate size-porosity relationships, it is still not clear which is the best approach for the development of a mathematical model which considers varying permeability inside an aggregate.

Numerical modelling based on computer simulations provides another approach to study the problem without using directly experimental measurements or a

mathematical formulation of the problem. This is the method adopted to investigate the hydrodynamic properties of fractal aggregates in this thesis, by considering the lattice Boltzmann method. The concept of this method is to build a model which reproduces the phenomenon with correct macroscopic physics using elements at mesoscopic level. With the development of computing power and the parallel computing technique, the method has a lot of advantages in the study of complex phenomena over traditional treatments.
In this thesis, we use the lattice Boltzmann method to make a model for simulating fluid flow with solid-fluid interactions and then to obtain quantitative information on the hydrodynamic properties of fractal aggregates. A key quantity, the settling velocity of fractal aggregates is found by estimating their hydrodynamic radius. The results should be directly applicable to understanding the transport, the circulation and the fate of colloids in aquatic systems. The thesis is organised as follows:

Chapter 2 provides an overview of the hydrodynamic properties of fractal aggregates. First, fractal aggregates and their main properties are presented together with aggregation processes and resulting fractal aggregates. Then the hydrodynamic properties of fractal aggregates are reviewed and discussed by considering the relation between the hydrodynamic radius and the gyration radius.

Chapter 3 introduces some key concepts dealing with fluid dynamics which help readers to better understand the fluid flows which are presented in the following chapters.

Chapter 4 presents the lattice Boltzmann method for the simulation of fluid flow. The method is employed to build 2D and 3D fluid models in the context of incompressible flow at a low Reynolds number. The main issues of the method are discussed including boundary conditions and fluid acceleration. Sources of error in the lattice Boltzmann simulations are also addressed.

Chapter 5 investigates fractal aggregates in two dimensions using lattice Boltzmann simulations. First, a simulation of the flow past a square array of cylinders is considered. An advantage of the bounce-back boundary over the mass-conserving boundary is discussed using simulations and the analytic solution of Sangani-Acrivos. Then, simulations are made with 2D fractal aggregates for a preliminary understanding of the effect of the fractal dimension on hydrodynamic properties. A concept of the hydrodynamic radius of 2D fractal aggregates is introduced. We discuss the effect of the fractal dimension by considering the calculation of R_h/R_g for some fractal aggregates having different compactness.

Chapter 6 presents a method to estimate, numerically, the hydrodynamic radius of 3D fractal aggregates. Simulation results considering various fractal ag-

gregates are obtained and some key conclusions are made on the hydrodynamic properties of fractal aggregates. Further investigations with artificial fractal aggregates are made and a novel parameter emerges to describe the hydrodynamic properties.

Chapter 7 presents another aspect of the hydrodynamic behaviour of fractal aggregates. Using an existing permeability model and classical governing equations inside porous objects, the Happel model is recovered from our lattice Boltzmann simulation results. Then, by fitting the lattice Boltzmann simulation data with the Brinkman equation, an estimation of the permeability and the effective viscosity is made. New important conclusions on the governing equations of the flow inside fractal aggregates are given at the end of the chapter.

Chapter 8 gives final conclusions of the work and possible further developments are discussed.

This thesis work has resulted in several publications:

- H. Nguyen, B. Chopard and S. Stoll. *Hydrodynamic properties and permeability of fractal objects*, Int. J. Mod. Phys. C, Vol. **18**, No. 4 (2007) 732-738

- H. Nguyen, B. Chopard and S. Stoll, *A lattice Boltzmann study of the hydrodynamic properties of 3D fractal aggregates*, Mathematics and Computers in Simulation, **72**, 103-107 (2006)

- Hung Phi Nguyen, B. Chopard and S. Stoll, *Hydrodynamic properties of fractal aggregates in 2D using lattice Boltzmann simulation*, Future Generation Computer Systems, **20**, 981:991 (2004)

- Hung P Nguyen, B. Chopard and S. Stoll, *Lattice Boltzmann Method to Study Hydrodynamic Properties of 2D Fractal Aggregates*, LNCS (book chapter), **2657**, 947-956, Springer, 2003)

Chapter 2

Fractal aggregates

2.1 Fractals and fractal geometry

People started using geometry to describe the surrounding world a very long time ago. Literally, geometry is the measurement of objects and their properties in space. Early in time, geometry referred to Euclidean geometry where objects were described as simple elements: points, lines, curves ... etc, having properties in space well defined.

For examples: a building can be represented as a cube composed of lines, whereas a river can be imagined as a curve... However, real geometries of objects in nature are more complicated. Indeed, when looking at a given magnification, we can find rugged profiles everywhere: the structures of familiar objects (mountains, coastline, rivers, etc.) or materials of scientific interests (colloids, gels, etc.). They cannot easily be described in terms of Euclidean geometry, with points, lines or curves. In a publication in 1967 [1] " How Long is the Coast of Great Britain?" Mandelbrot discussed the problem in measuring the length of the coastline of Great Britain. If we calculate the length in the usual way by approximating it to a polygonal path, each side of it having a length ϵ, then evaluating the total length of the polygonal when $\epsilon \to 0$ would never give a correct estimation as the result will go to infinity. The reason is that: the coastline has an inherent roughness at any magnification scale, although it is a continuous curve, it is not smooth

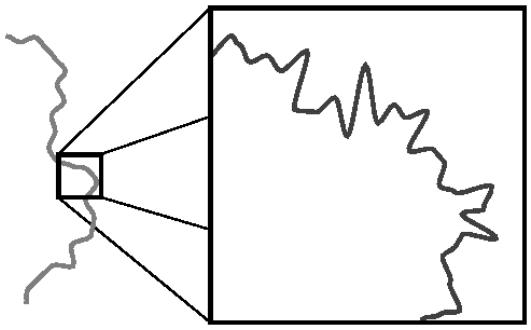

Figure 2.1: Each increase in scale reveals new degrees of roughness *(from Fractal geometry of John Hoggard)*

at any point. Thus, when looking at the coastline at finer and finer resolutions, more and more lengths have to be approximated and the total length appears to increase infinitely. Attempts of modelling other natural objects like mountains, clouds, etc. would go to the same conclusion that, for such irregular-shape objects, Euclidean geometries cannot help. As a result, we need geometries that are very far from lines, triangles, circles... For that purpose, a new geometry called *fractal geometry* was introduced.

2.1.1 What are fractals?

The concept of fractals was first mentioned in the book by Mandelbrot [2] in 1975 as he coined *"Fractals are geometrical shapes that, contrary to those of Euclid, are not regular at all. First, they are irregular all over. Secondly, they have the same degree of irregularity on all scales. A fractal object looks the same when examined from far away or nearby-it is self-similar. As you approach it, however, you find that small pieces of the whole, which seemed from a distance to be formless blobs, become well-defined objects whose shape is roughly that of the previously examined whole.* Thus a fractal is a geometrical shape that exhibits self-similarity across all scales.

Self-similarity means that the object shape is the same at any magnification scale or scaling invariance.
A classical and simple model to understand how fractals work is the Koch curve. It gives an intuitive picture of fractal length and self-similarity. The Koch curve is generated as shown in figure 2.2. The first step of the generating process begins with a straight line, called *initiator*. The second step consists to replace the initiator by a *generator*. The generator is a curve with 4 segments, each segment has a length equal to 1/3 length of the initiator.The next following steps consist to replace repeatedly each straight line (segment) of the curve with a copy of the generator.The Koch curve is a linearly self-similar fractal. However, these perfect fractal structures which mostly exist in theoretical models, belong to *regular* fractal structure family. There are also many fractals in nature which deviate from linear self-similarity, they are called *irregular* fractal structures. Some of these are fractals that describe random processes, while others are fractals that describe chaotic, or nonlinear systems. For these structures, successively magnifying a part of the fractal reveals a further structure that is nearly a copy of the original

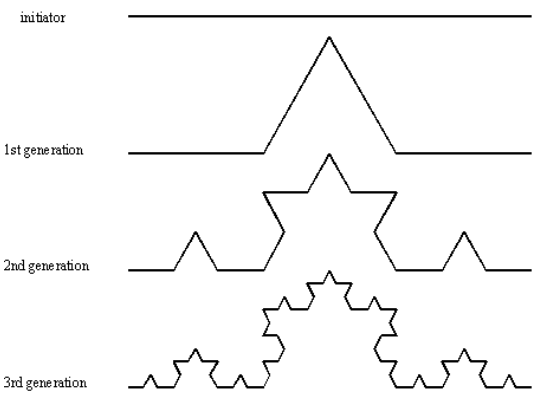

Figure 2.2: Koch curve

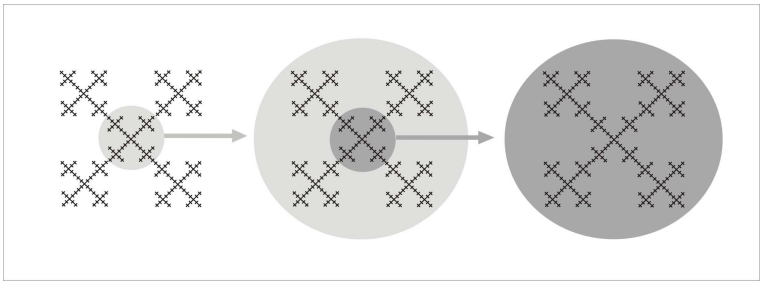

Figure 2.3: Regular fractal

with which we started. Fractal geometry is thus concerned with geometric scaling relationships and the symmetries associated with them. Basically it is applied to real systems which Euclidean geometry sometimes cannot describe.

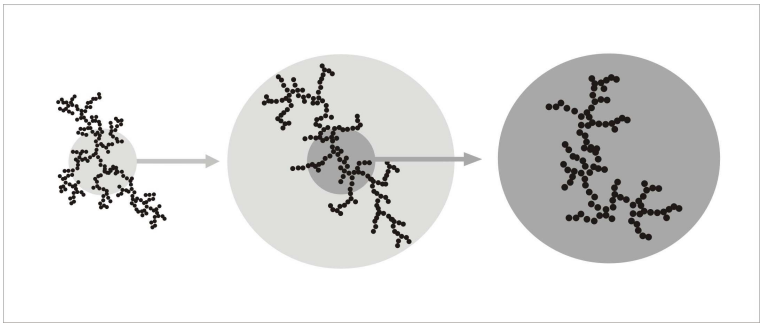

Figure 2.4: Irregular fractal

2.2 Fractal dimension

2.2.1 Topological dimension

By definition, dimensions represent the total number of parameters required to define the positions of any objects and their relevant characteristics in a conceptual space. In our real space, or three-dimensional space, the dimension of an object is the number of coordinates required to define one point in the space: a point has zero dimension, a line has one dimension, a plane has two dimensions while a solid volume has three dimensions. The role of the topological dimensions in a topological space is similar to that of the three-dimensional space. There are definitions for topological dimension, but most of them are presented in a mathematical way. We express here a more intuitive concept for topological dimension as "the number of independent ways one can move within an object" [3]. We can

intuitively think of a line as one-dimensional as there is only one way to move on the line. This is the same as a curve showing only one-topological dimension. A square can exhibit two dimensions but a circle will have one dimension. A cube may have three while a sphere has only two in terms of topological dimensions. A topological dimension is always a non-negative integer. In some special cases the topological dimension coincides with Euclidean dimension in 3-dimensional space.

2.2.2 Fractal dimension

Topological dimension is usually useful in the study of one-to-one transformation or homeomorphisms of objects. A homeomorphism is the smooth deformation of one space into another without tearing, puncturing, or welding it. However, for such highly irregular objects like fractals, the topological dimension behaves in quite unexpected ways. To characterise such objects, we have to refer to the Hausdorff-Besicovitch dimension. In fact, the Hausdorff Besicovitch dimension of an object is the parameter that gives a scaled-independent measurement of the object [4]. An illustration of the Hausdorff-Besicovitch dimension and the way to calculate it is given in the following example:
We consider several objects and each of them is broken into small copies reduced by a scaling factor:

1. A line segment is broken into 4 smaller segments. Each of these segments is similar to the original one, but they are all 1/4 shorter. The scaling factor here is equal to 4. This is also the idea of self similarity.

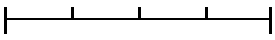

2. The square below is also broken into smaller pieces. Each piece is 1/4th the side of the original one. In this case it takes 16 of the smaller pieces to create the original.

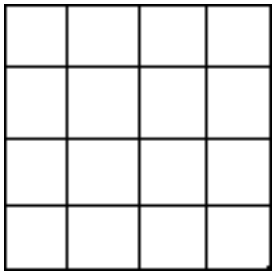

3. A cube is also broken down into smaller cubes of 1/4 the side of the original. It takes 64 of these smaller cubes to create the original cube.

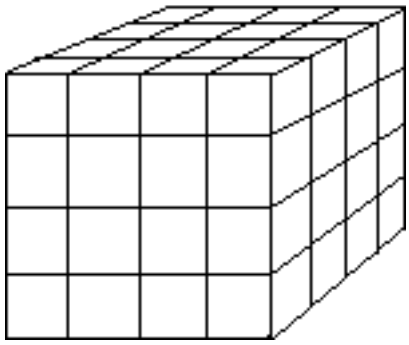

If we call N the total number of small pieces (copies of original object), S the scaling factor to which a small piece compares to the big one, then:

$$N = S^D.$$

Thus we obtain the Hausdorff-Besicovitch dimension of the object as

$$D = \frac{log(N)}{log(S)}.$$

For the line: $D = 1$ as $4 = 4^1$, for the square: $D = 2$ as $16 = 4^2$ and for the cube $D = 3$ as $64 = 4^3$.
In general, the Hausdorff-Besicovitch dimension of an arbitrary object in a metric space is given by the formula

$$D = -\lim_{r \to 0} \frac{log(N(r))}{log(1/r)},$$

where $N(r)$ is the total number of disks of size r needed to cover the object. In the above example, $r = 1/S$. If we come back to the estimation of the Hausdorff-Besicovitch dimension of Koch curve, one finds $N = 4$ and $S = 3$ and thus

$$D = \frac{log(4)}{log(3)} = 1.2619.$$

The Hausdorff-Besicovitch dimension of the Koch curve is no longer an integer like the topological dimension but a real number exceeding its topological dimension. It is worth noting that the topological dimension of the Koch curve is equal to one. The non-integer value of the Hausdorff dimension is revealed by the fact that: the Koch curve is a fractal. The Hausdorff-Besicovitch dimension of a fractal is then called the *fractal dimension*. One could revisit the definition of fractals with a connection to the concept of Hausdorff-Besicovitch dimension in the

book by Mandelbrot [4]: *"Every set with a non-integer Hausdorff-Besicovitch dimension (D) is a fractal. However not every fractal has a non-integer Hausdorff-Besicovitch dimension. A fractal is by definition a set for which D strictly exceeds the topological dimension."*.
We can see that, in fractal geometry, one might expect a similar parameter to quantify their characteristics and shapes as of topological dimension in topological space, that is fractal dimension. A qualitative definition for the fractal dimension in a clear way is also given: *The fractal dimension is a statistical quantity that gives an indication of how completely a fractal appears to fill space, as one zooms down to finer and finer scales.*

2.3 Fractal aggregates

Usually, aggregates are objects which result from processes in which small particles stick together irreversibly to form larger structures. We consider the aggregates formed in nature (those formed in rivers, lakes, oceans ...) by the coagulation of small inorganic and organic particles [5] as well as in laboratories, or those generated by computer simulations [6]. These aggregates exhibit complex structures and have relatively low average density. They are considered having random structures and geometrical characteristics which can be conveniently described by using fractal geometry. The processes to form these fractal aggregates are called *aggregation processes*. When mentioning fractal aggregates in this thesis, we are particularly interested in aggregates built with identical elementary particles, as shown in figure 2.4, where the elementary particle is considered as a solid sphere.

2.3.1 Characteristic radii of fractal aggregates

The geometry of fractal aggregates is clearly a key factor to define their behaviour in fluid or hydrodynamic properties. To quantify their geometry and hydrodynamic behaviour, it is common to use several quantities that are given in terms of radii of the fractal aggregates. The first important radius of a fractal aggregate that should be mentioned is the radius of gyration or gyration radius.
The gyration radius of an object is a parameter to quantify its mass distribution within the object and thus is a geometrical parameter to characterise the object's size. In the context of fractal aggregates, it is expected to be related to the hydrodynamic behaviour. If we consider a discrete distribution of masses m_i, as point-like masses, at the location $\mathbf{r_i}$, then the location of the mass center for this

distribution $\mathbf{r_{cm}}$ is given by

$$\mathbf{r}_{cm} = \frac{\sum_{i=1}^{N} m_i \mathbf{r_i}}{\sum_{i=1}^{N} m_i}. \tag{2.1}$$

The radius of gyration, usually noted as R_g , of the distribution is calculated using the center of mass as

$${R_g}^2 = \frac{\sum_{i}^{N} m_i (\mathbf{r_i} - \mathbf{r_{cm}})^2}{\sum_{i}^{N} m_i}. \tag{2.2}$$

In the case of a solid continuous object, the calculation of the gyration radius is given in terms of the mass density function

$${R_g}^2 = \frac{\int_V \rho(r) dV (r - r_{cm})^2}{\int_V \rho(r) dV}, \tag{2.3}$$

where dV is a differential volume at position r of the object having a mass density $\rho(r)$. This equation (2.3) can be used in the derivation of gyration radius of an homogeneous sphere (given in the appendix A). For a fractal aggregate composed of N identical elementary particles, the gyration radius becomes simpler since the masses of elementary particles are the same. Equation (2.2) then becomes

$${R_g}^2 = \frac{1}{N} \sum_{i=1}^{N} (\mathbf{r_i} - \mathbf{r_{cm}})^2. \tag{2.4}$$

Sometimes it is also convenient to write the gyration radius equation using the distance among the particles, according to

$${R_g}^2 = \frac{1}{2N^2} \sum_{i=1}^{N} \sum_{j=1}^{N} (\mathbf{r_i} - \mathbf{r_j})^2, \tag{2.5}$$

where $\mathbf{r_i}$ and $\mathbf{r_j}$ are the coordinates of particles i and j respectively of the aggregate.

It is also usual to use the outer radius of fractal aggregates as a characteristic value, particularly for spherical aggregates. The outer radius of a fractal aggregate is commonly defined as the radius of the circumscribed sphere of the aggregate centered at its mass center. Basically it is useful for highly symmetric

and spherical aggregates since the outer radius, R_{out}, is related to the gyration radius and the fractal dimension as (see appendix A for the detailed mathematical derivation)

$$R_{out} = \sqrt{\frac{D_f + 2}{D_f}} R_g. \tag{2.6}$$

Besides the geometrical radii, another important radius of fractal aggregates to quantify their hydrodynamic behaviour is the *hydrodynamic radius*. The hydrodynamic radius of a fractal aggregate, R_h, is defined as the radius of an impermeable sphere experiencing the same drag force F in the same fluid when moving with the same velocity as the fractal aggregate. It is direct to understand that the hydrodynamic radius of a hard and impermeable sphere is its radius. In the limit of low Reynolds numbers, it is calculated by the Stokes' Law,

$$F = 6\pi\mu u R, \tag{2.7}$$

where R is the radius of the sphere and is equal to its hydrodynamic radius, R_h . u represents the settling velocity of the sphere in the fluid while μ is the fluid viscosity. F is the drag force of the fluid on the sphere.
For complex structures, like fractal aggregates or colloids, it is not easy to determine the hydrodynamic radius. Some people may try to experimentally measure the settling velocity of the object in fluid, then make experiments with spheres in order to find out the corresponding hydrodynamic sphere. However, this task is very difficult.
Using experiments to determine the hydrodynamic radius of colloids or aggregates, it is more common to consider the translational diffusion coefficient of the aggregates in liquids. The translational diffusion coefficient D of the aggregates is found in the Stokes-Einstein relation [7]. In fact, the Stokes-Einstein equation describes how diffusion increases in proportion to temperature, and indicates that it is inversely proportional to the frictional force (drag force) experienced by a particle.

$$D = \frac{kT}{f_T} = \frac{kT}{6\pi\mu R_h} \tag{2.8}$$

where k is the Boltzmann constant, T is the temperature. f_T is called the translational friction coefficient that describes the interaction of the object with the fluid. The translational diffusion coefficient of fractal aggregates is usually measured experimentally by Dynamic Light Scattering technique (DLS).

2.3.2 Mass scaling principle

The most important property of fractal aggregates concerns the mass scaling property. Recall the self-similar fractals, the total number of copies of an original

object at a certain scale, is calculated by the power law relationship of the scale with the fractal dimension. The relationship which embodies the concept of fractal structure of aggregates is simply given as:

$$M \sim l^D, \tag{2.9}$$

where M is the mass of the aggregate, l is a characteristic length or size and D is a dimensionality factor, usually called mass fractal dimension. This relationship shows that: the mass M contained within a distance l from a position which is occupied by one particle is a power-law relationship between the length and a dimensionality parameter [8]. If we take an arbitrary particle within the aggregate and center an imaginary sphere on it with a radius l, then the mass contained inside the sphere should be related to the linear size of the sphere l in formula (2.9). For example: if the gyration radius is measured as a function of the aggregate mass, then:

$$M \sim {R_g}^{D_g}. \tag{2.10}$$

For fractal aggregates (as considered self-similar), the power exponent D or D_g should be the same for "all purpose" and equal to fractal dimension D_f of the object $D = D_g = D_f$. Note that the mass scaling principle (2.9) is asymptotically correct, as the size of the aggregates increases to a large limit. Mass scaling principle also implies that the average density of fractal aggregates in space dimension d decreases when the size of the aggregate increases, owing to

$$\rho \sim l^{D_f - d}, \tag{2.11}$$

where D_f is always smaller than d. For fractal aggregates, it is usual to write equation (2.9) using the total number of particles N as the mass and number of particles are clearly the same thing. To describe the mass scaling principle of fractal aggregates which are composed of N spherically identical particles, we can express it as:

$$N = \gamma_g (\frac{R_g}{a})^{D_f}, \tag{2.12}$$

where γ_g is normally called the *prefactor*. The subscript g reveals that it is associated with a linear size defined in terms of the gyration radius R_g. a is the radius of the elementary particle composing the aggregate. The fractal dimension of fractal aggregates, either formed in nature or in the laboratory experiments, have their fractal dimension lying between 1 and 3, $1 \leqslant D_f \leqslant 3$ [9].

2.3.3 Prefactor of fractal aggregates

As mentioned, the coefficient γ_g in the scaling relationship in equation (2.12) is called a *prefactor*. In general, the prefactor deals with the coefficient that appears in the scaling relationship of the mass of fractal aggregates with a characteristic

length (equation (2.9)). Thus the prefactor is associated to a given characteristic length i.e. γ_g for the gyration radius R_g , γ_{out} for the outer radius, γ_h for the hydrodynamic radius R_h ...etc. The prefactor is expected to depend on the space dimensionality and aggregation mechanism [10]. The role and importance of the prefactor will be investigated in details in chapter 6.

2.4 Aggregation models

Fractal aggregates are not only formed in nature (such as in aquatic systems) but can also be generated in the laboratory or by computer simulations using appropriate aggregation models. The aggregation models in the laboratory as well as computer simulations can reproduce fractal aggregates such as those found in natural systems in a convenient way. Usually computer simulation is preferred to generate fractal aggregates as it is easier to control. Different aggregation models have been introduced and mainly classified into two groups: particle-cluster and cluster-cluster models.

2.4.1 Particle-Cluster aggregation

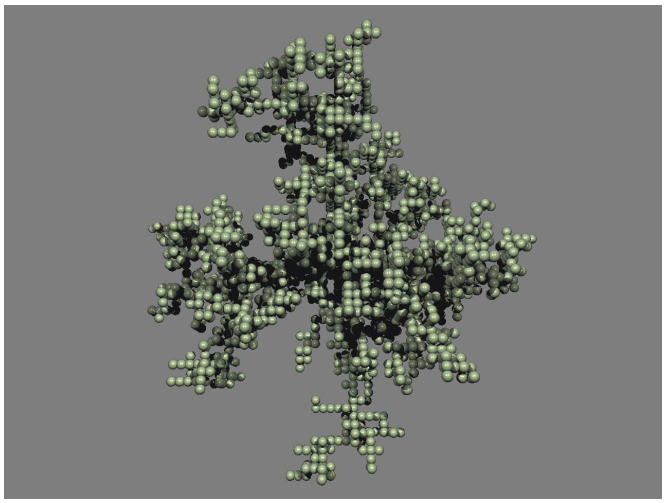

Figure 2.5: A Witten Sander fractal aggregate made of 3000 particles with $D_f = 2.49$ (using computer modelling data of CABE group)

The first aggregation model is the Eden model. The model is well described in the book by Jullien and Botet [11], in which it starts with a single seed on a site of a lattice and an aggregate is developed by filling randomly particles one by one to unoccupied sites around the seed with equal probability. Thus any empty neighbouring site of the aggregate has the same chance to accept the new

particle. However, this model does not lead to fractal structures though it is still considered as a basic model for aggregation [11]
The second model, which is more realistic, of particle-cluster aggregation is the Witten-Sander model by T.A. Witten and L.M.Sander [12]. In this model, the aggregates are formed by adding particles, one at a time, to a seed via random walk trajectories. The particles originate far away from the developing structure and perform random walks in the surrounding space. Once a particle encounters the structure, it then sticks to it. This model has been termed diffusion-limited aggregation (DLA for short) since the random walk of the particles can be viewed as a simulation of diffusion at the molecular level. Though the model is a little different from the Eden model, the difference in the resulting aggregates is striking. However, behind the applications of the Witten Sander aggregation model (e.g. in electro-deposition processes), such a model still has some limitations for the study of real aggregation processes, since in real systems, the aggregates can diffuse and stick to each other to form growing larger clusters.

2.4.2 Cluster-Cluster aggregation

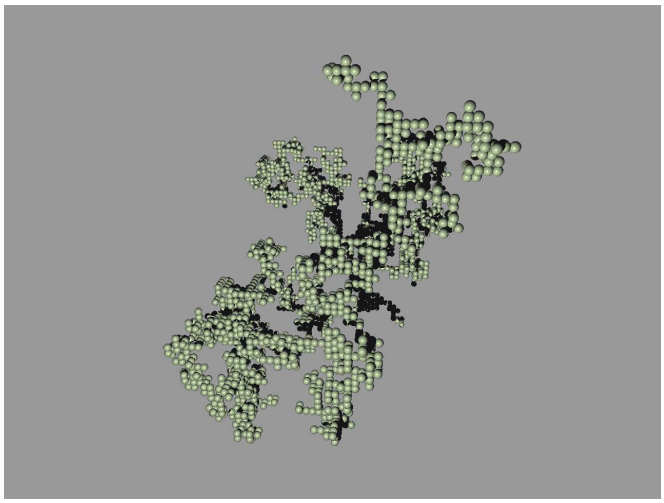

Figure 2.6: A CCA fractal aggregate made of 3000 elementary particles with $D_f \approx 2$ (using computer modelling data of CABE group)

The Cluster-Cluster Aggregation (CCA) model was introduced by both Kolb et al [13] and P. Meakin [14] in 1983 to provide a more realistic model of aggregation process. In the CCA model, the elementary particles are distributed randomly in a box where they move in all directions to mimic Brownian motion. When two particles come into contact, they stick to each other irreversibly and form a new aggregate (or dimer). The new aggregate thus diffuses in the box

with a given diffusion coefficient depending on its size and geometry. It can come into contact with another aggregate and stick to form a larger aggregate. The aggregate becomes larger and larger with time until all the aggregates stick together and it remains the only aggregate in the box.
Aggregates obtained from this model can be well described by using fractal geometry concepts [15]. The obtained fractal aggregates have fractal dimension depending either on the diffusion rate of the clusters or the chemical reactivity at the collision time. Therefore, the CCA fractal aggregates can be classified in two subsets of aggregation process: Diffusion Limited Cluster-Cluster Aggregation (DLCA) and Reaction Limited Aggregation (RLCA).
The DLCA process is considered as an extension of the DLA Witten Sander model where, instead of particles diffusing in a random walk process, the cluster can diffuse and form the fractal aggregate with a sticking probability $P_0 = 1$. The RLCA process is then somehow related to a sticking probability P_0. Unlike the DLCA process where the sticking probability remains equal or very close to 1, in this process, the sticking probability is reduced to less than 1 owing to the decrease of the chemical reactivity of the particles. It is due to the presence of electro repulsive interactions, for example, if charged particles having the same charge are considered. Therefore, the sticking probability is less than 1. In more details, thermal motion is not sufficient to overcome the electrostatic repulsive barrier, as a result, the particle bounce off each other many times before attaching together. It is also the reason why RLCA aggregates exhibit higher fractal dimensions than DLCA aggregates as the particles can penetrate deeply inside the structure and make it more compact.
In our experiments, both Witten Sander and CCA fractal aggregates are employed in the investigation of hydrodynamic properties.

2.5 Hydrodynamic properties of fractal aggregates

The hydrodynamic properties of fractal aggregates have attracted the interests of scientists for a long time. Much have been done to contribute to the understanding of the hydrodynamics of fractal aggregates on different sides and using different methods or models. Basically, the hydrodynamics of fractal aggregates is related to the aggregate behaviour in fluids in motion. The phenomena can be formulated simply as such: let an impermeable solid object be immersed in an incompressible fluid such as water. A drag force will be exerted on the object due to gravity. While staying in the fluid, there is also a force of fluid acting on it in terms of buoyancy force. These forces result in a total drag acting on the object as a whole and and the initiation of its motion in the fluid This in turn creates the hydrodynamic effects: interaction of the fluid with the object, friction of the

fluid on it, movement of the object in the fluid ...
To predict the correct answer on the hydrodynamic behaviour of an arbitrary object, or a fractal aggregate moving in a fluid, however, is difficult. To quantify the hydrodynamic behaviour of fractal aggregates, it is usual to measure some related hydrodynamic quantities .i.e settling velocities, hydrodynamic radius, permeability ... We now summarise the results of previous studies on hydrodynamic properties of fractal aggregates to obtain an overview.

2.5.1 State of the art

There have been numerous publications on the hydrodynamics of fractal aggregates on different aspects. Here we focus on studies where the hydrodynamic properties of fractal aggregates are considered such as the hydrodynamic radius, the settling velocity, the permeability or the drag force ... These studies are based on different theories or models and if we classify them, they can be divided into: Kirkwood-Riseman based models, porous media (sphere) models, direct simulations and experiments.

Kirkwood Riseman model

In this model, the Kirkwood Riseman theory [16] is the main principle to construct the calculations. Here, a cluster consisting of N particles of radius a is placed in the quiescent fluid and moves with velocity $\mathbf{u}$. Considering an elementary particle i of the fractal aggregate, it experiences a force $\mathbf{F_i}$ from the fluid (in other words the frictional force acting on the particle). If the particle was alone in the fluid, it would move with velocity $\mathbf{u_i}$. The force $\mathbf{F_i}$ is then related to $\mathbf{u_i}$ as

$$\mathbf{F_i} = -\zeta_i \mathbf{u_i}, \tag{2.13}$$

where ζ_i is the friction coefficient of elementary particle i.
The total drag on the whole fractal aggregate can thus be estimated as the sum of the forces $\mathbf{F_i}$

$$\mathbf{F} = \sum_{\mathbf{i=1}}^{\mathbf{N}} \mathbf{F_i}. \tag{2.14}$$

The main point in the Kirkwood Riseman theory is that: the particle i attached to the fractal aggregate moves with the velocity $\mathbf{u}$ of the fractal aggregate, and the change of the velocity is due to the perturbations induced by the presence of the other particles of the fractal aggregate. Thus, the force acting on each elementary particle $\mathbf{F_i}$ can be written as the sum of the force exerted on the particle as if it was alone and the forces created from the perturbations. First, the velocity $\mathbf{u}$ is calculated from a perturbation velocity $\mathbf{v_i'}$ as

$$\mathbf{u} = \mathbf{u_i} + \mathbf{v_i'}. \tag{2.15}$$

Then replacing (2.14) to equation (2.13) we have

$$\mathbf{F_i} = \zeta_\mathbf{i}(\mathbf{v'_i} - \mathbf{u}). \tag{2.16}$$

The perturbation velocity $\mathbf{v'_i}$ is given by Oseen and Burgers [17]

$$\mathbf{v'_i} = -\sum_{\mathbf{j=1,j\neq i}}^{\mathbf{N}} \mathbf{T_{ij}} \cdot \mathbf{F_j}, \tag{2.17}$$

where $\mathbf{T_{ij}}$ is Oseen tensor and $\mathbf{F_j}$ is the force of particle jth acting on the fluid. In fact, the perturbation velocity is the sum of disturbance velocity of fluid at position of particle ith due to the presence of particle jth. By replacing (2.17) into (2.16) and (2.14) we have

$$\mathbf{F_i} = -\zeta_\mathbf{i}\big(\mathbf{u} + \sum_{\mathbf{j=1,j\neq i}}^{\mathbf{N}} \mathbf{T_{ij}} \cdot \mathbf{F_j}\big), \tag{2.18}$$

$$\mathbf{F} = -\sum_{\mathbf{i=1}}^{\mathbf{N}} \zeta_\mathbf{i}(\mathbf{u} + \sum_{\mathbf{j=1,j\neq i}}^{\mathbf{N}} \mathbf{T_{ij}} \cdot \mathbf{F_j}). \tag{2.19}$$

Since elementary particles are considered as identical spheres, the friction coefficient ζ_i of particle i is the same as those of other elementary particles and ζ_j of particle j. They are equal to ζ of sphere that is determined by Stokes' Law [17]

$$\zeta_i = \zeta_j = \zeta = 6\pi\mu a \tag{2.20}$$

The Oseen tensor is estimated from the fluid viscosity μ and the distance between particle ith and jth. Basically, there are two expressions used for Oseen tensor, the first one is given by Oseen [18]

$$\mathbf{T_{ij}} = \frac{1}{8\pi\mu r_{ij}}\Big(\mathbf{I} + \frac{\mathbf{r_{ij}}\mathbf{r_{ij}}}{{r_{ij}}^2}\Big) \tag{2.21}$$

and the second one is an extension from Yamakawa, Rotne and Prager [18]

$$\mathbf{T_{ij}} = \frac{1}{8\pi\mu r_{ij}}\left[\Big(\mathbf{I} + \frac{\mathbf{r_{ij}}\mathbf{r_{ij}}}{{r_{ij}}^2}\Big) + \frac{2a^2}{{r_{ij}}^2}\Big(\frac{\mathbf{I}}{3} - \frac{\mathbf{r_{ij}}\mathbf{r_{ij}}}{{r_{ij}}^2}\Big)\right] \tag{2.22}$$

where r_{ij} is the distance from particle i to particle j (center to center) and $\mathbf{r_{ij}}$ is the vector connecting particle i to particle j. $\mathbf{I}$ is the unit tensor. The Oseen tensor in (2.22) is reduced to (2.21) when the size of particle a is approaching 0. This modified version of the Oseen tensor is often preferred to the original one (2.21) which is reported to give an anomalous result [19]. The equation (2.19) can be written in a general form as [17]

$$\mathbf{F} = -\mathbf{f} \cdot \mathbf{u}, \tag{2.23}$$

where $\mathbf{f}$ is a friction coefficient tensor. For translational motions, the translational friction coefficient is related to the diffusion coefficient given by the Stokes-Einstein relation. In the general form of the Einstein relation for an arbitrary object, the diffusion coefficient is expressed as a diffusion coefficient tensor, $\mathcal{D}$, that is related to a friction coefficient tensor as

$$\mathcal{D} = k_B T \mathbf{f^{-1}}, \tag{2.24}$$

where k_B is the Boltzmann constant and T is the temperature. Both $\mathcal{D}$ and $\mathbf{f}$ can be partitioned in 3x3x3 blocks, which correspond to translation (tt), rotation (rr) and translation rotation coupling (tr) [20]. The translational coefficient, D, is estimated from the translational diffusion coefficient tensor by taking the average of the diagonal as

$$D_{tt} = \frac{1}{3} Tr(\mathcal{D}_{tt}). \tag{2.25}$$

As we consider that the motion of the fractal aggregate is purely translational, the friction coefficient tensor $\mathbf{f}$ coincides with the translational friction coefficient tensor. For the sake of convenience, we denote $D \equiv D_{tt}$; hence, the translational diffusion coefficient is written

$$D = \frac{1}{3} Tr(k_B T \mathbf{f^{-1}}) = \frac{k_B T}{3} Tr(\mathbf{f^{-1}}). \tag{2.26}$$

The translational diffusion coefficient is usually written as

$$D = \frac{k_B T}{f_T}, \tag{2.27}$$

where f_T is the friction coefficient. f_T is then given by

$$f_T = \frac{3}{Tr(\mathbf{f^{-1}})}. \tag{2.28}$$

For a given cluster, with a given structure, moving with a given velocity $\mathbf{u}$, the system described in equation (2.18) can be solved numerically in which, the force $\mathbf{F}$ and the friction coefficient tensor $\mathbf{f}$ are determined; so is the translational friction coefficient.

An alternative solution to the scalar form of translational friction coefficient is given by [17]

$$f_T = \frac{6\pi\mu a N}{1 + \dfrac{a}{N} \displaystyle\sum_{i=1}^{N} \sum_{j \neq i, j=1}^{N} \frac{1}{\langle r_{ij} \rangle}}. \tag{2.29}$$

The angular brackets in $\dfrac{1}{\langle r_{ij} \rangle}$ denotes an average taken over internal coordinates [17].

To approximate the friction coefficient in (2.29) for fractal aggregates such as in the analysis of Van Saarloos [21], Wiltzius [22] and Lattuada [18], it is necessary to know the number of particles at a distance r from a given particle of the cluster. This information can be obtained by using the particle-particle correlation function $g(r)$. Thus, the averaging in (2.29) becomes

$$\sum_{j\neq i,j=1}^{N} \frac{1}{\langle r_{ij}\rangle} = \int_0^\infty g(r) 4\pi r dr, \tag{2.30}$$

and the translational fiction coefficient is written as

$$f_T = \frac{6\pi\mu a N}{1 + a\int_0^\infty g(r) 4\pi r dr} \tag{2.31}$$

The translational friction coefficient is usually defined as

$$f_T = 6\pi\mu R_h. \tag{2.32}$$

By replacing (2.31) with (2.32) we finally obtain

$$R_h = \frac{aN}{1 + a\int_0^\infty g(r) 4\pi r dr}. \tag{2.33}$$

It is clear that, to estimate hydrodynamic radius of a fractal aggregate, one needs to model the particle-particle correlation function $g(r)$.
The application of the Kirkwood Riseman scheme is found in several models [17,18,23–25] where both traditional equations (2.19), (2.23) and particle-particle correlation functions $g(r)$ were used.
W. Hess and co-workers [23] used Kirkwood Riseman scheme to estimate the hydrodynamic radius and its ratio with the gyration radius for fractal aggregates. They assumed that the fractal aggregate had a spherically symmetric density distribution. Instead of using particle-particle correlation function $g(r)$, they used the density distribution function. The function was a function of radial distance r and fractal dimension D_f as $\rho(r) = Ar^{D_f-3}$. While using this model Hess derived the following expression for R_h

$$R_h = \frac{2R(D_f - 1)}{D_f}, \tag{2.34}$$

where R was the outer radius that was equal to (see appendix A.3 for more details)

$$R = \sqrt{\frac{D_f + 2}{D_f}} R_g. \tag{2.35}$$

Thus the ratio of R_h over R_g can be expressed as

$$\frac{R_h}{R_g} = \frac{2(D_f - 1)}{D_f}\sqrt{\frac{D_f + 2}{D_f}}. \tag{2.36}$$

This result suggests that the ratio $\frac{R_h}{R_g}$ depends only on the fractal dimension D_f. Chen et al [24] applied the fundamental Kirkwood-Riseman scheme (2.18) with modified the Oseen tensor (Yamakawa, Rotne and Prager) (2.22) where the system of equation was formed on the hydrodynamic interaction between each pair of particles in the cluster

$$\mathbf{F_i} = -\zeta_\mathbf{i}\big(\mathbf{u} + \sum_{\mathbf{j=1, j\neq i}}^{\mathbf{N}} \mathbf{T_{ij}} \cdot \mathbf{F_i}\big). \tag{2.37}$$

Note that, by comparison to equation (2.18), one has the interaction only between each pair of particles in the cluster $\mathbf{F_i} = \mathbf{F_j}$. This system was solved numerically using the method of McCammon and Deutch [26]. Using this scheme, Chen et al made calculations of hydrodynamic radii in two experiments. In the first one, calculation was made for aggregates obtained from an off-lattice model for reaction-limited aggregation having $D_f \sim 2.1$. This D_f was very close to the experimental one of Wiltzius [22], and size up to 400 elementary particles. Resulting value of $\frac{R_h}{R_g}$ for this type of aggregates was equal to 0.97 and assumed to be independent of aggregate sizes. In a later experiment [25], calculation was made for 2 types of aggregates: DLA and bond-percolation aggregates. Both these types of aggregates had bigger sizes than the ones in the first experiment (up to 900 elementary particles). They both have almost the same fractal dimension: $D_f = 2.44$ for DLA and $D_f = 2.49$ for bond-percolation aggregates. For the DLA aggregates, obtained $\frac{R_h}{R_g}$ was equal to 1.14 ± 0.07 and independent of aggregate sizes. For bond-percolation aggregates, the value of $\frac{R_h}{R_g}$ was reported to slightly increase with aggregate sizes and approaches to an asymptotic value bigger than 1.14.

Lattuada et al [18] used Monte-Carlo simulations to model the particle-particle correlation function $g(r)$. They determined this function in an explicit form and derived an analytical expression for hydrodynamic radius in which all coefficients could be estimated numerically. They applied this derivation on both fractal aggregates DLCA and RLCA having fractal dimension D_f equal to 1.86 and 2.05 respectively. Their results claimed a decrease of the $\frac{R_h}{R_g}$ ratio as the cluster size

increases. For large clusters, they found values of $\frac{R_h}{R_g}$ equal to 0.765 for DLCA and 0.831 for RLCA. It was supported that, the decrease of $\frac{R_h}{R_g}$ with cluster size could be due to fluctuations in result at small aggregate sizes before it reaches an asymptotic value at larger sizes, about 1000 particles in this work.

Porous sphere model

The principle of this approach is to model the fractal aggregate as a porous media or porous sphere in a moving fluid at a low Reynolds number. Hydrodynamic study of fractal aggregates is achieved by solving the governing equation of the flow. The flow in the exterior region of an fractal aggregate is usually described by the Stokes equation while the interior region is controlled by Darcy's law or the Brinkman equation. By coupling both interior and exterior regions to solve the system of these governing equations with boundary conditions, hydrodynamic properties of fractal aggregates can be found. Basically, in this model, a permeability model of fractal aggregates is usually required.

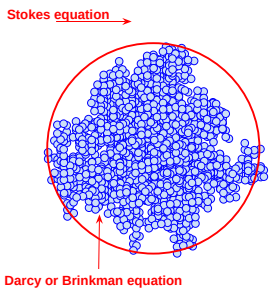

Figure 2.7: Porous sphere model

A number of studies [21, 27–34] have been made on this topic. In fact, the principle originated from previous study by Brinkman [35, (1949)] and was followed by other several researchers [36–39]. They tried to develop a model to explain the flow past a porous sphere at low Reynolds numbers.

Fractal aggregates in this scheme are usually defined as objects consisting of identically spherical particles in which the density distribution is known. In the analysis of Saarloos [21], the fractal aggregate was modelled as a porous sphere where the density distribution $\rho(r)$ was described as a function of distance r. By claiming to use the local permeability [21] as $(6\pi\mu a\rho(r))^{-1}$, Saarloos used the Debye-Brinkman equation of the flow at the interface of the sphere and the continuity equation

$$\nabla \cdot u = 0, \tag{2.38a}$$

$$-6\pi\mu a\rho(r)u + \mu\nabla^2 u = \nabla P, \tag{2.38b}$$

where ∇P is gradient of pressure, a is radius of elementary particle, u represents flow velocity and μ is fluid viscosity. To solve these equations, he used the Faxen theorem that estimates the drag force in terms of flow over the surface. The

volume of the porous sphere, i.e the drag force was approximated from the fractal aggregate velocity and the mean flow velocity over its surface. This allowed the estimate of the hydrodynamic radius as a function of outer radius R_{out} and κ a quantity named inverse permeability:

$$R_h = R_{out}\frac{1-\kappa^{-1/2}\tanh\kappa^{1/2}}{1+\frac{3}{2}\kappa^{-1}-\frac{3}{2}\kappa^{-3/2}\tanh\kappa^{1/2}}, \tag{2.39}$$

where κ was determined as

$$\kappa \equiv (6\pi a^3\rho_0)\Big[\frac{R_{out}}{a}\Big]^{D_f-1}. \tag{2.40}$$

κ has a given value for each fractal aggregate depending on its size (R_c) and its fractal dimension. The behaviour of ratio $\frac{R_h}{R_{out}}$ was developed as a function of κ. Thus, for uniform porosity sphere, the ratio $\frac{R_h}{R_g}$ was given by

$$\frac{R_h}{R_g} = \Big(\frac{D_f+2}{D_f}\Big)\frac{1-\kappa^{-1/2}\tanh\kappa^{1/2}}{1+\frac{3}{2}\kappa^{-1}-\frac{3}{2}\kappa^{-3/2}\tanh\kappa^{1/2}} \tag{2.41}$$

With large aggregate sizes, the ratio of $\frac{R_h}{R_{out}}$ approached an asymptotic value. A detailed derivation can be found in [21]. Results using this model for a fractal aggregate within a range of $[700\overset{o}{A} \leq R_g \leq 7000\overset{o}{A}]$ and $D_f = 2.07$, corresponding to the fractal aggregate set of Wiltzius [22] gave the ratio of $\frac{R_h}{R_g}$ about 1.23
In another attempt, Warren [29] applied the porous model to numerically estimate the $\frac{R_h}{R_g}$ for two types of fractal aggregates: particle-cluster and cluster-cluster aggregates. Using the same method as Saarloos, he wrote the density distribution of fractal aggregates as

$$\rho(r) = \begin{cases} \rho_0 r^{D_f-3} & (r<R) \\ 0 & (r>R) \end{cases} \tag{2.42}$$

and claimed that ρ_0 was estimated from the prefactor γ_g found empirically from the scaling law of R_g with D_f, $R_g = \gamma_g N^{1/D_f}$. The fractal size ranged from 50 to 256 particles for both DLCA and RLCA aggregates. The results demonstrated that the ratio of $\frac{R_h}{R_g}$ depends on the size of fractal aggregates, i.e. the ratio decreased as the size of aggregates increased for both DLCA and RLCA aggregates.

For RLCA aggregates, this ratio approached more rapidly the scaling limit value. At large sizes of fractal aggregate, the ratio $\frac{R_h}{R_g}$ from Warren's model prediction reached 0.81 for DLCA aggregate with $D_f = 1.8$ and 0.88 for RLCA aggregate at $D_f = 2.0$

Another extension based on the porous model was the one used by Veerapaneni and Wiesner [30] and later by Kim [34]. The flow in the exterior region of the fractal aggregate was described by the Stokes equation as usual, and the interior flow was governed by the Brinkman equation. As a key point of the model, they assumed that the permeability of the fractal aggregate varies radially from the center to the outer radius. Using this assumption, the fractal aggregate was divided into N spherical shell-layers where the permeability was a constant at a given shell but different from the neighbouring ones. The boundary conditions in the model included are: (i) the velocity very far from the fractal aggregate is uniform; (ii) the velocity at the center of the fractal aggregate is null and (iii) there is a continuity of the stress tensor and the velocity on the surface of each shell, i.e. the normal and the tangential components of the stress tensor and the velocity at the outer surface of porous shells are continuous and they are zero at the surface of the innermost shell. The mathematical description of this model is summarised below

$$\text{Radially varying permeability} \begin{cases} \mu\nabla^2 u = \nabla P & R_{out} \leq r < \infty \\ \nabla \cdot u = 0 & R_{out} \leq r < \infty \\ \mu^*\nabla^2 u^* - \dfrac{\mu}{K_i} u^* = \nabla P^* & r_{i-1} \leq r \leq r_i \\ \nabla \cdot u^* = 0 & r_{i-1} \leq r \leq r_i \end{cases}$$

To solve this system of equations with boundary conditions, Veerapaneni et al used the stream function in spherical coordinate and assumed the effective viscosity equal to fluid viscosity $\mu^* = \mu$. They calculated the drag force F on the fractal aggregate as

$$F = 6\pi\mu u_\infty R_{out}\Omega, \tag{2.43}$$

where

$$\Omega = 2A_2\frac{\sqrt{K_n}}{3R_{out}}. \tag{2.44}$$

A_2 is a coefficient in the stream function that must be computed numerically and K_n is the permeability of the outermost shell. Therefore, by introducing an appropriate permeability model, it is possible to estimate the total drag on the fractal aggregate and then the hydrodynamic radius. It appeared in the work of Veerapaneni et al that the permeability model given by Happel [40] was the most appealing model for fractal aggregates when compared to the others. The ratio $\frac{R_h}{R_g}$ which was calculated for fractal aggregates at $D_f = 2.1$ with the size range

of silica aggregates (as in Wiltzius experiment) was found to be equal to 1.03.
Kim and Yuan [34] formulated the hydrodynamics of an ideal fractal aggregate and solved the problem exactly in the same way as Veerapaneni, i.e. using porous sphere model with the Brinkman equation for the interior flow and using the same boundary conditions. The difference is that they modelled the permeability of this fractal aggregate increasing radially by assuming that the permeability K increases quadratically as $K = k_2 r^2$ from the center of the fractal aggregate . k_2 here is a permeability factor. This factor is calculated from the prefactor k_f and by using an empirical approximation for the permeability [34] of Davies.

$$k_2 = \frac{27}{16}\Big(5k_f\Big)^{-3/2}. \tag{2.45}$$

The prefactor k_f was found in the scaling principle for outer radius

$$N = k_f\Big(\frac{R_{out}}{a}\Big)^{D_f}. \tag{2.46}$$

In fact, k_f represents a simple geometrical factor and is estimated directly from the fractal aggregate . Note that R_{out} is connected to R_g by equation (2.6). With the fractal dimension of this ideal aggregate equal to 1.67, the ratio $\dfrac{R_h}{R_g}$ was found to be equal to 0.875.
It is worth noting that in the works of Chellam [28], Veerapaneni [30], Vanni [32] and Kim [34], a factor was introduced to quantify implicitly the hydrodynamics of fractal aggregates namely the fluid collection efficiency η. This factor was defined as the ratio of the flow rate passing through the fractal aggregate to that of approaching flow. η was usually calculated by using the dimensionless permeability (the permeability is normalised with the radius of elementary particle, $\zeta^2 = k/a^2$) [28]. This fluid collection efficiency was reported as a correlation factor with Ω value found in the model of Veerapaneni [30], Vanni [32] and Kim [34].

Numerical simulations

To the best of our knowledge, there are not many studies done using simulations for investigating the hydrodynamics of fractal aggregates in which the results addressed directly to the drag force, the hydrodynamic radius or the settling velocity of fractal aggregates . One can mention the simulations of Adler [41], Adrover [42] in 2D, Coelho [43] and Binder [44]. The first two studies were carried out in 2D while the others used 3D simulations. In principle, simulations used to investigate the hydrodynamics of fractal aggregates consist of solving the Stokes equation of the flow around the fractal aggregate , either by finite element [41] or lattice Boltzmann [42, 44] methods.
In the early work of Adler [41], the hydrodynamics of fractal aggregates for both

Witten Sander and CCA was investigated in two-dimensional simulations by setting a flow passing a horizontally periodic squared array of fractal aggregates in a channel and at low Reynolds number. The governing equation was the Stokes equation with the boundary conditions of zero velocity on the wall of the channel and on the surface of the fractal aggregate . Elementary particles of the fractal aggregate were represented as a square lattice point while the aggregate size was limited to 64 particles. The hydrodynamics of the fractal aggregate were found in terms of the seepage velocity as a function of the gyration radius, where no effect of the fractal dimension D_f on the seepage velocity was found. The role of D_f was also reported not to be visible on the drag force.

Adrover and Giona [42] used lattice Boltzmann method to simulate two dimensional flow passing a fully periodic square array of DLA aggregates with $D_f = 1.7$ at a low Reynolds number. Their simulation results were compared to the results of the simulation of the flow passing a periodic array of cylinders having the radius circumscribed the DLA aggregates. They showed in both simulations that the fluid set up its motion to the same mean velocity. Thus, the factor controlling the seepage velocity was given by the orthogonal projection of the object to the flow direction, not the fractal dimension. In contrast to the result of Adler, they showed a visible role of D_f on the drag force exerted on the fractal aggregate . It is worth noting that the size of the fractal aggregates , in the simulations of Adrover and Giona, was bigger than ones in Adler's simulations. Furthermore, the simulations of Adler were implemented between 2 plates where the effect of the plates was expected to be considerable.

Coelho et al [43] implemented 3D simulations of the flow past a cubic array of fractal aggregates by solving the Stokes equation. The hydrodynamics of the fractal aggregate were found in terms of R_h and the effect of D_f was investigated. It is worth noting that in the work of Coelho, R_h was defined as the radius of a sphere moving with the same seepage velocity in the simulation domain (unit cell)

$$R_h = \frac{F}{6\pi\mu\bar{v}}, \tag{2.47}$$

where $\bar{v}$ was the seepage velocity along the macroscopic pressure drop. However, this is a slightly different definition since hydrodynamic radius is normally defined as the radius of sphere moving with velocity in the infinite domain (where the effect of the finite size is neglected). Thus, the hydrodynamic radius in the work of Coelho et al, was assumed to be a function of volume concentration ϕ, D_f and to be linearly depending on the gyration radius. Note that the volume concentration was defined as the ratio of the volume of the fractal aggregate to the total volume of the unit cell. The relation between the hydrodynamic and the gyration radius was a linear function, where the coefficients depend only on D_f and volume concentration.

$$R_h = a(\phi, D_f)R_g + b(\phi, D_f) \tag{2.48}$$

These coefficients a and b were found as a function of ϕ by extrapolating from results for different volume concentrations and D_f. Then the ratio $\frac{R_h}{R_g}$ was reported for dilute limit at $D_f = 2.1$ and found equal to 1.03.
Recently Binder et al [44] used lattice Boltzmann simulation to estimate drag force exerting on DLCA aggregates with $D_f = 1.8$ and 1.9. They found a general trend of increasing drag force with projected area of the fractal aggregates . However, no simple geometric parameters of the aggregates were found to achieve a correlation with the drag force. Note that, in their simulations, the simulation domain size was a critical problem since they tried to enlarge it as much as possible in order to reduce errors. Thus, only simulations with rather small aggregates, up to 250 particles, were performed which experienced a big variation in projected area.

Experimental results

Experimental results are used to validate the computational models and theories for hydrodynamics of fractal aggregates. There are several ones on hydrodynamics of fractal aggregates in terms of ratio of $\frac{R_h}{R_g}$ and settling velocities. One should mention here the well-known experimental results of Wiltzius [22]. Wiltzius used the Static and Dynamic Light Scattering technique to study the hydrodynamic behaviour of colloidal silica aggregates having $D_f = 2.08 \pm 0.05$. He found the ratio of $\frac{R_h}{R_g} = 0.72 \pm 0.02$ in a range of $500A \leq R_h \leq 700A$. Both hydrodynamic radius and gyration radius found by Wiltzius exhibited scaling principle with the mass i.e. $M \sim {R_h}^{D_f}, M \sim {R_g}^{D_f}$. The ratio $\frac{R_h}{R_g}$ then did not depend on the size of fractal aggregates. Furthermore, Pusey [45] recommended to re-correct it by taking into account the effect of polydispersity and suggested a value of 0.98 instead of 0.72.
In another similar experiment, Rim et al [46] found the ratio of $\frac{R_h}{R_g}$ equal to 0.52 ± 0.08 for colloidal silica aggregates with $D_f = 1.75$ in a range of $470A \leq R_h \leq 8130A$, suggesting a decrease in $\frac{R_h}{R_g}$ with D_f when comparing to the result of Wiltzius.
Wang and Sorensen [47] estimated $\frac{R_h}{R_g}$ value in the experiment of mobility of TiO_2 aerosol using Static and Dynamic Light Scattering technique, similarly to Wiltzius. The TiO_2 aerosol aggregates were reported having $D_f = 2.15$ and 1.75 respectively where the corresponding ratio of $\frac{R_h}{R_g}$ were found to be equal

to 0.97 ± 0.05 and 0.7 ± 0.05. This resulted in a controversy of the results in comparison with others.
Some other results on the hydrodynamics of fractal aggregates involved in measuring the settling velocities of fractal aggregates showed a considerable difference with mathematical models. Johnson et al [48] showed in their measurements of settling velocity of latex aggregates that the settling velocities of those aggregates were on average 4-8.3 times faster than the ones predicted from models based on Stokes' Law with impermeable or permeable sphere.

2.5.2 Discussion

Going through the models for hydrodynamics of fractal aggregates and their results which are summarised in table 2.1, one can see that there are still no clear conclusions for the hydrodynamic behaviour of fractal aggregates since the results from different models do not agree well with each other and with experimental ones as illustrated in figure 2.8. Experimental values of $\frac{R_h}{R_g}$ still show differences

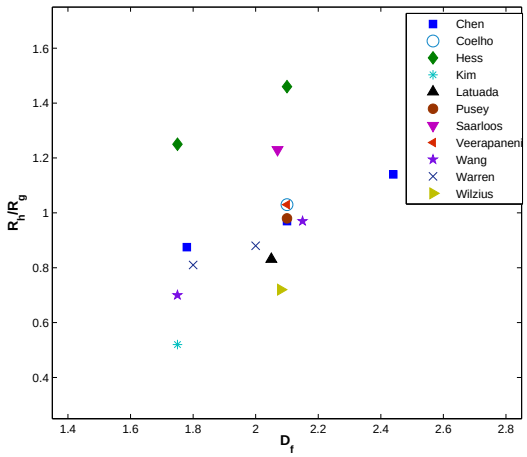

Figure 2.8: Ratio of $\frac{R_h}{R_g}$ by different researches

although the corrected value of $\frac{R_h}{R_g}$ from 0.72 in Wiltzius experiment to 0.98 by Pusey seems to agree with the value from Wang for $D_f = 2.1$ ($\frac{R_h}{R_g}$ =0.97), but for $D_f = 1.75$, $\frac{R_h}{R_g}$ in experiment of Rim is considerably different with the one in Wang's experiment (0.52 compares to 0.7). However, in our opinion, the result

of Wang's experiment seems to be more convincing as it took into account the polydispersity effect, while it is not clear whether Rim's experiment took it into consideration or not. The discrepancy is still visible between experimental results with either the Kirkwood Riseman scheme based models or porous sphere based models or numerical simulations. We can observe that, in each model, there are still limitations. In the Kirkwood Riseman scheme, one needs to calculate or model correctly the particle-particle correlation function $g(r)$. But how to model $g(r)$ correctly is still a cumbersome problem. In some studies, this function appears in calculation of the hydrodynamic radius R_h as [21–23]

$$R_h = \frac{\int drr^2 g(r)}{\int drrg(r)} \tag{2.49}$$

For some aggregates built from a given point, for example the center point of DLA aggregates, $g(r)$ actually becomes a three-particle correlation function. It is also reported [21], that some solutions of $g(r)$ can be used for spherical aggregates at $D_f = 3$. But when applying them to equation (2.49), the results obtained for R_h are different than R_{out}. For densely packed spherical aggregates, having $D_f = 3$, one should obtain $R_h = R_{out}$ since the aggregates are nearly impermeable spheres. It is easy to see in the result of Hess [23] based on the Kirkwood Riseman scheme for spherically symmetrical aggregate, when $D_f = 3$ the ratio $\frac{R_h}{R_g}$ =1.72 is far from the result 1.291 of a hard sphere. And for D_f smaller than 3, $\frac{R_h}{R_g}$ seems to be overestimated when comparing it to other results. With $D_f = 2.1$, $\frac{R_h}{R_g}$ is equal to 1.4638, far from the value 0.97 of Wang [47] or 0.72 of Wilzius.
In another evidence for the discrepancy in researches of hydrodynamics, the result of Wang [47] for fractal aggregates with $D_f = 2.15$ gives a value of $\frac{R_h}{R_g}$ =0.97 which is similar to the one of 0.97 given by Chen et al [24, 25] for fractal aggregates with $D_f = 2.1$ and close to the value of 0.98 given by Pusey [45]. Note that this value of Pusey is the re-corrected one for Wilzius results of fractal aggregates with nearly the same fractal dimension $D_f = 2.1$. However for different fractal aggregates with $D_f = 1.75$, the value of $\frac{R_h}{R_g}$ =0.7 given by Wang shows a clear difference when compared to 0.875 given by Chen for the same aggregates. As a result, the agreement in the results for fractal aggregates with $D_f = 2.15$ given by Wang and Chen could be fortuitous. The discrepancy in the results of Chen [24, 25] with experimental values together with deviated result of Hess [23] show that there are limitations in the Kirkwood Riseman scheme. In addition, another limitation of the Kirkwood Riseman scheme was reported to give singularities to the translational diffusion coefficients when the range of interaction is

large [49].
The porous sphere scheme might be considered a good idea when seeing fractal aggregates as porous media and dealing with the governing equation of fluid motion. The results obtained, however, still do not show a convincing agreement with experiments or with the Kirkwood Riseman scheme. Although the value of $\frac{R_h}{R_g}$ in Veerapaneni seems to converge to the experiment of Wang and the Kirkwood Riseman model of Chen for $D_f = 2.1$ aggregates i.e. $\frac{R_h}{R_g}$ =1.03 compares to 0.97 and 0.98 respectively, but Saarloos' value of $\frac{R_h}{R_g}$ looks overestimated when giving 1.23. The limitation in the porous model scheme lies behind the difficulty of introducing a good model of permeability for fractal aggregates. So far this is too hard a topic to deal with. On the other hand, it is still controversial to see whether the Brinkman equation or simply Darcy's law can really be the governing equation inside fractal aggregates . In fact, the application of the Brinkman equation seems to have gone far from original idea to see it on a thin transitional layer between porous and open media. Furthermore, the validity of Brinkman equation also depends on the porosity of fractal aggregates .
At last, numerical simulations did not play a big part compared to other methods, but it might have overcome the limitations of the Kirkwood Riseman scheme and the porous sphere model, except that the results obtained are still limited i.e. Adrover et al [42], Adler [41] in 2D, Coelho et al [43] and Binder et al [44] in 3D.
In 2D, results still show a contradiction, i.e Adler's simulation gave contradictory conclusions about the role of D_f to the one of Adrover. One can see that the model of Adler was too small and the concept of R_h depended on volume concentration was not the same as the one in the infinite domain.
In 3D, it was also the case of Coelho [43] where the concept of R_h was developed in a limited simulation domain, although they tried to obtain a converged value when the domain approached infinity by some extrapolating procedures. Nevertheless, loss of accuracy could still happen. Therefore, a good way in obtaining the hydrodynamic radius from direct simulations is still missing. The idea to implement simulations in a big domain in order to mimic a nearly infinite model [44] would be very costly and there is no guarantee to obtain convincing results, since there is no analytical solution of fluid flow past a fractal aggregate.
The determination, if the $\frac{R_h}{R_g}$ value is independent of the size N of fractal aggregates , has not yet been clearly made. In many models, this ratio remains constant [22, 24, 46, 47] whilst others claim that it changes with the size of aggregates [18, 23]. The latter might have experienced the fact that the employed fractal aggregates were small; therefor anisotropy of particle distribution exhib-

ited a strong effect.

From all these studies, one can deduce that the $\frac{R_h}{R_g}$ value should be a function of fractal dimension D_f and should increase with D_f up to the limit of the sphere. In some works [28,30,34], an implicit factor, fluid collection efficiency, has emerged. However, in our opinion, it is a correlation factor with D_f, which is difficult to obtain accurately.

2.5.3 Conclusion

We have reviewed most of the key studies dealing with the hydrodynamics of fractal aggregates with their results. These works have been achieved through either experiments, the Kirkwood Riseman scheme, porous sphere scheme or numerical simulations. However, results have not yet shown a full agreement and a clearly convincing argument has not yet been made. Despite this situation, we can conclude some important points about the hydrodynamics of fractal aggregates:

1. The $\frac{R_h}{R_g}$ ratio of fractal aggregates is a function of D_f. In most results, one can see, in overall, the change of $\frac{R_h}{R_g}$ with D_f and a trend of increasing $\frac{R_h}{R_g}$ with an increase of D_f . $\frac{R_h}{R_g}$ thus should be an increasing function of D_f as suggested by Gmachowski [31] with a maximum limit equal to that of a sphere ($D_f = 3$) 1.291.

2. The scaling principle would be conserved for either R_g and R_h ,

$$N \sim {R_g}^{D_f} \sim {R_h}^{D_f}$$

thus the $\frac{R_h}{R_g}$ should not depend on the size of fractal aggregates . It is worth noting that in the results which exhibit a change of $\frac{R_h}{R_g}$ with aggregate sizes, the aggregate sizes were rather small (usually less than 1000 particles) and fluctuations played a considerable role.

3. A convincing way to obtain R_h is still missing. We have seen the limitations of the Kirkwood Riseman model, where R_h depends on modelling the pair correlation function and the Oseen tensor itself. The porous sphere scheme requires a good permeability model as well as appropriate governing equations for the flow in the interior region of fractal aggregates . This is still an open question. Numerical simulations on the hydrodynamics of fractal aggregates are still limited; Coelho's model seems to have developed in a promising direction, however, using linear extrapolation (simply by fitting linear lines) at low volume concentration

might lead to loss of accuracy. A good way to extract R_h of fractal aggregates is needed for further improvement.

4. Beside the fractal dimension, D_f, the hydrodynamics of fractal aggregates , i.e. $\frac{R_h}{R_g}$ might be quantified by other factors; however, which has not yet been made clear previously. Some studies introduced fluid collection efficiency η however it is not easily quantified in terms of the building mechanism or the physical properties of fractal aggregates. More quantitative factors of the physical properties of fractal aggregates should be included in the description of $\frac{R_h}{R_g}$ i.e. where prefactors are expected to play a role.

Finally, a computational model is still required to further develop an understanding of the hydrodynamics of fractal aggregates .

	Scheme	D_f	N	$\frac{R_h}{R_g}$ varies with N	$\frac{R_h}{R_g}$
Wiltzius	experiment	2.08 ± 0.05	$500A \leq Rh \leq 700A$	No	0.72 ± 0.02
Kim	experiment	1.75	$470A \leq Rh \leq 8130A$	No	0.52 ± 0.08
Wang	experiment	2.15	$500nm \leq Rg \leq 2000nm$	No	0.97 ± 0.05
Wang	experiment	1.75	$500nm \leq Rg \leq 2000nm$	-	0.7 ± 0.05
Hess	Kirkwood-Riseman	2.1	-	No	1.46
Hess	Kirkwood-Riseman	1.75	-	No	1.25
Chen	Kirkwood Riseman	1.78	50-350	No	0.875
Chen	Kirkwood Riseman	2.1	400	No	0.97
Chen	Kirkwood Riseman	2.44	900	increases	1.14 ± 0.07
Pusey	Wiltzius correction	2.1	-	-	0.98
Latuada	Kirkwood Riseman	2.05	1000	decreases	0.831
Saarloos	Porous sphere	2.07	$700A \leq Rg \leq 7000A$	increases	1.23
Warren	Porous sphere	2	50-256	decreases	0.88
Warren	Porous sphere	1.8	50-256	decreases	0.81
Veerapaneni	Porous sphere	2.1	-	-	1.03
Coelho	3D simulation	2.1	-	-	1.03

Table 2.1: Hydrodynamics of fractal aggregates

Chapter 3

Basic fluid dynamics

Fluid dynamics is the study of motion of fluids including materials like: liquids, gases or plasma, ... The aim of fluid dynamics is to understand the behaviour of a fluid in motion for a given arrangement. In principle, the study is based on the basic physical laws of mechanics, including three physical principles: conservation of mass, Newton's laws of motion, i.e. second law of Newton, and the laws of thermodynamics. Mathematical statements of these principles lead to the fundamental governing equations of fluid dynamics - the continuity equation, the momentum and the energy equations.
In this chapter we shall give some essentials of fluid dynamics in order to make the connection to the following parts and to help understand the fluid models or fluid concepts, if mentioned. First, we shall give some concepts and definitions of fluid flows. Second, we shall give a brief summary of governing equations of fluid dynamics focusing on those within the scope of our latter fluid model. Detailed descriptions and derivations of the equation can be found in some textbooks of fluid dynamics [50–52].

3.1 Some definitions of flow and fluid

In ordinary life, we often observe a lot of fluid flows around us and may find that they vary from one situation to another. They vary because of the nature of the different fluids as well as the types of flow. For example, we may see the smooth flow of a river but also turbulent flow near a waterfall. We find that the flow of oil slower than that of water. In order to distinguish the different situations, one needs a classification of common flows.

- Uniform and non-uniform flow: an *uniform* flow is a flow having the same velocity in magnitude and direction at every point in the fluid. Other flows violating this condition are naturally considered as *non-uniform*.

- Steady and unsteady flow: a flow is considered as *steady*, when parameters

like velocity, pressure, density ...etc do not change with time. Otherwise it is an *unsteady flow*.

- Compressible and Incompressible flow: when a fluid shows density changes due to a change of pressure, thus making the density no longer a constant, the flow is said to be *compressible*. In contrast, an *incompressible* flow can be considered to have a constant density. A fluid, like water is usually considered as incompressible while gases can be considered compressible fluids, as they can be easily compressed.

- Turbulent and Laminar flow: *Turbulent* is a flow regime in which the flow is dominated by recirculation, eddies and having chaotic, stochastic property changes. The turbulent flow develops a highly random character with rapid irregular fluctuations of velocity in both space and time. On the contrary, the *laminar* flow refers to a flow in which the fluid moves smoothly in parallel layers without disruption from layer to layer. Both turbulent and laminar flows are closely related to a quantity, the Reynolds number (3.1). Usually one can state that, a flow at very high Reynolds numbers is turbulent while small Reynolds numbers produce laminar flows.

- Viscous and Inviscid flow: Viscous flows are flows in which the fluid friction has significant effect. This friction effect of a fluid is usually quantified by its *viscosity*. The viscosity of a fluid is a physical quantity measuring the resistance to flowing; it depends on the type of fluid. One special case of viscous flow is the *Stokes* flow, which is a flow at a very low Reynolds number where inertial forces are too small in comparison to viscous forces and thus can be neglected. On the contrary, when inertial forces are much larger than viscous forces (this occurs at large Reynolds number) the viscous forces can be ignored and the flow becomes *inviscid*. Inviscid flows are normally obtained at high Reynolds numbers.

- Newtonian and Non-Newtonian fluid: These concepts concern a classification of fluid properties. In many fluids (water, gases ...) the components of stress tensor are linearly proportional to the first spatial derivatives of the velocity components. The constant of proportionality is known as the viscosity of the fluid. These fluids are called *Newtonian* fluids. For other materials like emulsions, the behaviour is different, and the viscosity is not a constant for all shear rates; these fluids are known as *non-Newtonian* fluids.

The fluid flows of interest in this thesis do not cover all of these. Actually, we limit our scope of fluid flow in application of the settling phenomena of fractal aggregates in water, thus the fluid is considered Newtonian and the flow is mentioned as a viscous and incompressible flow at low Reynolds number.

The Reynolds number

The Reynolds number is an important parameter in fluid dynamics to quantify a flow and is considered as a flow classificator. Let us consider a simple example of a flow in a pipe. For this flow, it is characterised by several parameters including: the density ρ of the fluid, the dynamic viscosity μ, the average velocity u and the diameter of the pipe d. Now, people may ask: what type of flow do we obtain for given values of the above parameters? Thus, we see that it is not relevant to derive an equation, then associate the "type of flow" to given values of those dimensional quantities. A parameter is introduced to answer this question: the Reynolds number. Actually, the Reynolds number (abbreviated as Re) is a non-dimensional parameter and defined as

$$Re = \frac{\rho u d}{\mu} \tag{3.1}$$

This is known as the Reynolds number of the flow in the pipe. In general situation, the Reynolds number is written as

$$Re = \frac{\rho \mathcal{U} \mathcal{L}}{\mu} = \frac{\mathcal{U} \mathcal{L}}{\nu} \tag{3.2}$$

where $\nu = \dfrac{\rho}{\mu}$ is kinematic viscosity of the fluid, $\mathcal{U}$ is the characteristic velocity of flow and $\mathcal{L}$ is the characteristic length scale of the flow. The Reynolds number gives us relative information of how fast a given fluid is moving in a given size of the system. As mentioned, at high Reynolds numbers, the flow is likely to be turbulent while at very low Reynolds numbers the flow becomes laminar.

3.2 Governing equations

Fundamental governing equations of fluid dynamics are actually based on one three basic physical principles including: 1. The principle of mass conservation; 2. The Newton's second law $\mathbf{F} = m\mathbf{a}$; 3. The principle of energy conservation. Note that, here we mention only the equations based on the first two principles, i.e. mass conservation and Newton's second law. The energy conservation principle leading to the energy equation will not be presented since it is out of the scope of our application. Detailed derivations of all equations can be found in technical books on fluid dynamics like [51,52] . It is also worth noting that the fundamental physical principles are applied to the *fluid elements* themselves. A fluid element can be considered as an infinitesimally small volume of fluid dV, which has the same sense as in differential calculus. However, it is large enough to contain a huge number of molecules so that it is still viewed as continuous medium. The

fluid element can be considered to be fixed in space with fluid moving through it or moving along a streamline of flow.
The first governing equation of flow motion is obtained by considering the mass flux through a fluid element dV fixed in space where the mass is conserved. It is called the continuity equation or mass conservation equation, since the physical principle of mass conservation has been applied to derive the equation

$$\partial_t \rho + \nabla \cdot (\rho \mathbf{u}) = 0. \tag{3.3}$$

When the flow is incompressible (ρ is constant), the continuity equation becomes

$$\nabla \cdot \mathbf{u} = 0. \tag{3.4}$$

The second governing equation of fluid flow is obtained from another physical principle: the second law of Newton. When considering a fluid element (infinitesimal volume), the second law of Newton states that the force acting on the element is equal to the rate of change of momentum of a fluid element. The mathematical expression of this principle can be written as follow (more details of the derivation for this equation can be found in [51, 52])

$$\rho \partial_t \mathbf{u} + \rho \mathbf{u} \cdot \nabla \mathbf{u} = \sum \mathbf{F}. \tag{3.5}$$

The total force acting on the fluid element $\sum \mathbf{F}$ has two sources:
1. Body forces: which act directly on the volumetric mass of fluid element (e.g. gravitational force , electric or magnetic forces ...).
2. Surface forces: which act directly on the surface of the fluid element due to either the pressure gradient surrounding the fluid element or the shear and the normal stress from friction.
If we look at a viscous flow, with the viscosity effect playing a role, then the viscous force should be considered together with the pressure gradient and the body force. The spatial components of the viscous force are given by

$$F_{vx} = \mu\big(\frac{\partial \tau_{xx}}{\partial x} + \frac{\partial \tau_{yx}}{\partial y} + \frac{\partial \tau_{zx}}{\partial z}\big) = \mu\big(\frac{\partial^2 U_x}{\partial x^2} + \frac{\partial^2 U_x}{\partial y^2} + \frac{\partial^2 U_x}{\partial z^2}\big) = \mu \nabla^2 U_x, \tag{3.6}$$

$$F_{vy} = \mu\big(\frac{\partial \tau_{xy}}{\partial x} + \frac{\partial \tau_{yy}}{\partial y} + \frac{\partial \tau_{zy}}{\partial z}\big) = \mu\big(\frac{\partial^2 U_y}{\partial x^2} + \frac{\partial^2 U_y}{\partial y^2} + \frac{\partial^2 U_y}{\partial z^2}\big) = \mu \nabla^2 U_y, \tag{3.7}$$

$$F_{vz} = \mu\big(\frac{\partial \tau_{xz}}{\partial x} + \frac{\partial \tau_{yz}}{\partial y} + \frac{\partial \tau_{zz}}{\partial z}\big) = \mu\big(\frac{\partial^2 U_z}{\partial x^2} + \frac{\partial^2 U_z}{\partial y^2} + \frac{\partial^2 U_z}{\partial z^2}\big) = \mu \nabla^2 U_z. \tag{3.8}$$

The total forces $\sum \mathbf{F}$ is now equal to

$$\sum \mathbf{F} = -\nabla P + \mu \nabla^2 \mathbf{u} + \mathbf{F}. \tag{3.9}$$

∇P and $\mathbf{F}$ are the pressure gradient and the body force respectively where $\mu\nabla^2\mathbf{u}$ contributes the viscous term. Replacing (3.9) into (3.5) we obtain the Navier-Stokes equation

$$\partial_t\mathbf{u} + \mathbf{u}\cdot\nabla\mathbf{u} = -\frac{1}{\rho}\nabla P + \nu\nabla^2\mathbf{u} + \frac{1}{\rho}\mathbf{F} \tag{3.10}$$

In special cases, by considering a flow in a stationary state at low Reynolds numbers (so that the inertial force is very small), the terms $\partial_t\mathbf{u}$ and $\mathbf{u}\cdot\nabla\mathbf{u}$ disappear and the left-hand side of the equation 3.10 can be neglected. Hence we obtain the Stokes equation

$$\mu\nabla^2\mathbf{u} = \nabla P - \mathbf{F} \tag{3.11}$$

Traditionally, the Stokes equation is written with the presence of the pressure gradient term. However, if the flow is initiated only by a body force, one can write the Stokes equation 3.11 as

$$\mu\nabla^2\mathbf{u} = -\mathbf{F} = \nabla P_{ind} \tag{3.12}$$

where the pressure gradient ∇P_{ind} substitutes for the body force $\mathbf{F}$ and is conceived as a pressure gradient induced by the imposed body force, and not the one imposed by an external factor.
On the other hand, the flow is inviscid, when the viscous term is negligible, and hence the momentum equation becomes the Euler equation

$$\partial_t(\rho\mathbf{u}) + \nabla\cdot(\rho u\mathbf{u}) = -\nabla P + \mathbf{F} \tag{3.13}$$

3.3 An example: Poiseuille flow

We give here a basic example of a fluid flow, namely the Poiseuille flow as it is often used to validate many computational fluid models due to the simplicity of the flow description and its analytical solution of the Navier-Stokes equation. The Poiseuille flow is actually a flow in a pipe at a low Reynolds number ($Re < 30$ [51]) so that it is considered to be a laminar flow. The flow is steady and a pressure gradient or a body force is applied to the direction x. In 2D it is represented as the flow in a channel as shown in figure 3.1. As the Reynolds number is low, the Stokes equation 3.11 is supposed to govern the flow and we can easily derive the solution for it. Considering the 2D situation as shown in the figure 3.1, we combine the effect of pressure gradient ∇P and $\mathbf{F}$ to a total force G_x as both are acting along the same x direction

$$-\nabla P + \mathbf{F} = -\nabla_x P + F_x = G_x \tag{3.14}$$

For symmetry reason the flow is only in the x direction, and the velocity $\mathbf{u}$ is then $(\mathbf{u_x}, 0, 0)$. Therefore, equation (3.11) is written only for component $\mathbf{u_x}$

$$\mu\nabla^2\mathbf{u_x} = G_x \tag{3.15}$$

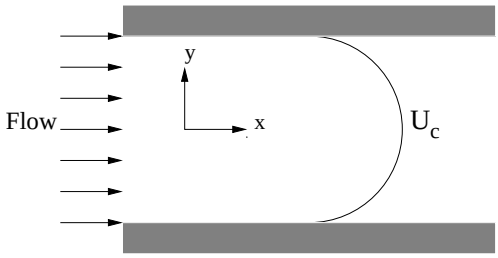

Figure 3.1: Poiseuille flow in 2D

or

$$\mu\big(\frac{\partial^2 \mathbf{u_x}}{\partial x^2} + \frac{\partial^2 \mathbf{u_x}}{\partial y^2}\big) = G_x \tag{3.16}$$

The component $\dfrac{\partial^2 \mathbf{u_x}}{\partial x^2} = 0$ as there is no gradient of u_x along x in stationary condition, thus becoming

$$\mu \frac{\partial^2 \mathbf{u_x}}{\partial y^2} = G_x \tag{3.17}$$

This equation has a parabolic form solution according to

$$\mathbf{u} = \mathbf{u_x}(y) = \frac{G_x}{2\mu} y\big(L - y\big) \tag{3.18}$$

where L is the width of channel and $y \in [0; L]$. The velocity profile of Poiseuille flow in 2D is a parabola with a maximum value $U_c = \dfrac{G_x L^2}{8\mu}$ obtained when $y = L/2$, at the middle position of the channel.

Chapter 4

The lattice Boltzmann method for fluid dynamics

The lattice Boltzmann method [53–56] has emerged to be a powerful simulation tool for computational fluid dynamics. This method is developed from the Boltzmann equation and is considered as a discrete approach since it simulates a system (e.g fluid) using the particle distribution on a grid or a lattice. The method is well suited to simulate flows around complex geometries and is easy to implement on the computer with a simple algorithm. The concept of this method is to discretize the fluid as mesoscopical fluid particles moving on a lattice. This idea is an interesting aspect of the method as it does not need to describe the microscopic details but aims to conserve the macroscopic dynamics of the system (e.g the macroscopic dynamics of the fluid is recovered to obey the Navier-Stokes equation). The method has gained huge successes due to its capability of modelling a wide variety of complex fluid problems: from single to multiphase flows in complex geometries, from laminar to turbulent models. This method can also model the time evolution of the system and accommodates various boundary conditions. Further, from the computation point of view, this method is easy to parallelise due to the simplicity of its implementation.
In this chapter, we present the idea of the lattice Boltzmann method by firstly giving the introduction of its predecessor: the Lattice Gas Automata. Then the principles of the lattice Boltzmann method are presented focusing on constructing the model for fluid dynamics. Important issues of the lattice Boltzmann method are also considered including boundary conditions and fluid acceleration. Finally, different error sources in a lattice Boltzmann simulation of fluid flow are addressed so that it helps controlling the total error of the simulation.

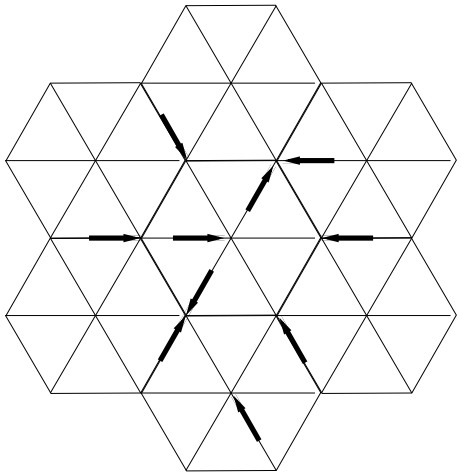

Figure 4.1: A LGA schema

4.1 Lattice Gas Automata

By its name, Lattice Gas Automata (LGA) describes itself. LGA simulates the dynamics of a system in a fully discrete space-time domain. The domain includes a lattice (grid) composed of discrete sites and connecting links between them. One example of a simple model of LBA can be formulated including a hexagonal lattice as a matrix and shown in the figure 4.1. The gas is presented on the lattice as discrete particles which can be imagined to be fictitious. They stay on the lattice sites and move from one site to its neighbours by travelling along the links. The time in LGA is discrete and is represented as time steps, in which the system evolves from one time step to another. In one time step, a particle moves from one site to a neighbouring one and collides with other particles on that site. The dynamics of the system is obtained by letting the gas evolve in a moving-colliding manner. Usually, the rules of the motion of the gas particles are set to conserve the mass and the momentum. In LGA, we often denote d as the spatial dimension of the lattice and z as the number of links connecting one lattice site to its neighbours. The configuration of the lattice is then abbreviated by D_dQ_{z+1}. The shortest link of the lattice, by convention, is assigned as the unit length Δr (or the lattice spacing). Longer links (diagonal links) can be $\sqrt{2}\Delta r$ or $\sqrt{3}\Delta r$ ... depending on topological configuration of the lattice. We abbreviate the number of incoming particles at site r with a velocity $\mathbf{v_i}$ at time t as $N_i(r,t)$. The index i runs from 0 to z indicating the directions of moving particles. $N_0(r,t)$ and $\mathbf{v_0}$ are the number of particles and the velocity at rest. $N_i(r,t)$ representing the number of gas particles is always an integer; in terms of computer programming they can be represented by Boolean variables. The dynamics of a system in LGA is obtained from the evolution of the system including two basic steps: 1. The

collision and 2. The *propagation*.
The collision step describes the collision of particles happening locally at one lattice site. While this step gives the description of the particle distribution, the propagation step actually describes a gas particle propagating or streaming from one site to a next site in one time step. Mathematically, the dynamics of LGA can be written as

$$N_i(\mathbf{r} + \Delta t\mathbf{v_i}, t + \Delta t) = N_i(\mathbf{r}, t) + \Omega_i(N), \tag{4.1}$$

where $\Omega_i(N)$ is a *collision operator*, which describes the details of the physical process and depends on the model. In Lattice Gas Automata, the macroscopic quantities are defined from the ensemble average values, for instance the local density or the local velocity. The local density $\rho(\mathbf{r}, t)$ in LGA is written as

$$\rho(\mathbf{r}, t) = \sum_{i=0}^{z} \langle N_i(\mathbf{r}, t) \rangle \tag{4.2}$$

where the index i runs over the lattice direction. The local velocity $\mathbf{u}(\mathbf{r}, \mathbf{t})$ is defined in the expression

$$\rho(\mathbf{r}, t)\mathbf{u}(\mathbf{r}, t) = \sum_{i=0}^{z} \langle N_i(\mathbf{r}, t) \rangle \mathbf{v_i}. \tag{4.3}$$

An other quantity having an important role is the momentum tensor which is defined as

$$\prod\nolimits_{\alpha\beta} = \sum_{i=1}^{z} \mathbf{v}_{i\alpha}\mathbf{v}_{i\beta}\langle N_i(\mathbf{r}, t) \rangle, \tag{4.4}$$

where it presents the flux of $\alpha-$ components of momentum transported along $\beta-$ axis [57].
The first LGA model is known as the HPP model [58] made by Hardy, Pomeau and de Pazzis which uses the D_2Q_4 configuration: a square lattice with 4 links for one site. It has been applied to simulate the gas with a simple set of rules. This model was proved to be anisotropic since it creates some unphysical anisotropies when rotating the lattice [59]. Another important model of LGA is the FHP model [60], named after its inventors: Frisch, Hasslacher and Pomeau, which uses a hexagonal lattice (the D_2Q_6 and the D_2Q_7). This model is isotropic and can reproduce, in some limit, the hydrodynamics of a fluid, i.e. the Navier Stokes equation.
As we have to deal with the Boolean particles in LGA, the macroscopic behaviour of the system is obtained by averaging the states of each lattice cell over a large path of cells and over a period of time step. It is considered as a disadvantage since it is a time consuming process. In addition, the simulation using LGA is often very noisy. To eliminate this problem, one has been proved that it is more advantageous to average the micro-dynamics of the system **before** simulating it rather than after doing it [57]. This is the idea of the lattice Boltzmann method.

4.2 The lattice Boltzmann method for fluid simulation

The lattice Boltzmann (LB) method follows the same idea as the LGA when it also considers the fluid on a lattice with space and time discrete. However, instead of directly describing the fluid by discrete particles (Boolean variables), it describes the fictitious system in terms of the probabilities of presence of the fluid particles. The lattice Boltzmann equation is obtained by ensemble averaging the equation (4.1)

$$\langle N_i(\mathbf{r} + \Delta t\mathbf{v_i}, t + \Delta t)\rangle = \langle N_i(\mathbf{r}, t)\rangle + \langle \Omega_i(N)\rangle. \tag{4.5}$$

We assume that the system satisfies the Boltzmann molecular chaos hypothesis, i.e. there is no correlation between particles entering a collision. Thus, the collision operator can be expressed as $\langle \Omega_i(N)\rangle = \Omega_i(\langle N\rangle)$ and we obtain the Lattice Boltzmann equation

$$f_i(\mathbf{r} + \Delta t\mathbf{v_i}, t + \Delta t) = f_i(\mathbf{r}, t) + \Omega_i(f), \tag{4.6}$$

where $f_i = \langle N_i\rangle$ denotes the probability to have a fictitious fluid particle of velocity $\mathbf{v_i}$ entering lattice site $\mathbf{r}$ at time t. Commonly f_i is called the fluid field or the particle distribution function. Now $f_i \in [0; 1]$ is no longer a Boolean variable as LGA but a real value, and so is the collision operator. The collision operator is normally a non-linear expression and requires a lot of computation time [57]. In a big lattice, e.g. 3D model, the computation becomes impossible even on a massively parallel computer. To overcome this problem Higuera et al [61, 62] proposed to linearise the collision operator around its local equilibrium solution to reduce the complexity of the operation. Using this idea, a so-called lattice BGK (LBGK) [63] was introduced in which the collision between particles is described in terms of the relaxation towards a local equilibrium distribution [64]. BGK stands for Bhatnager, Gross and Krook, named after the authors. The LBGK is considered to be one of the simplest forms of the Lattice Boltzmann equation which is mathematically expressed as

$$f_i(\mathbf{r} + \Delta t\mathbf{v_i}, t + \Delta t) - f_i(\mathbf{r}, t) = \Omega_i(f) = \frac{1}{\tau}\big(f_i{}^{eq}(\mathbf{r}, t) - f_i(\mathbf{r}, t)\big), \tag{4.7}$$

or it is equivalent to

$$f_i(\mathbf{r} + \Delta t\mathbf{v_i}, t + \Delta t) = \frac{1}{\tau} f_i{}^{eq}(\mathbf{r}, t) + \big(1 - \frac{1}{\tau}\big) f_i(\mathbf{r}, t). \tag{4.8}$$

τ is called the relaxation time, which is a free parameter of the model to determine the fluid viscosity. $f_i{}^{eq}$ is the local equilibrium function and is actually a function of the density and the flow velocity u. Physically, the idea of the equilibrium function f^{eq} corresponds to a situation where the rate of each type of

collision equilibrates, or in other words, the amount of fluid taken in at a given site is equal to the amount of fluid taken out.

When simulating fluid, we consider the LBGK model on a given lattice con-

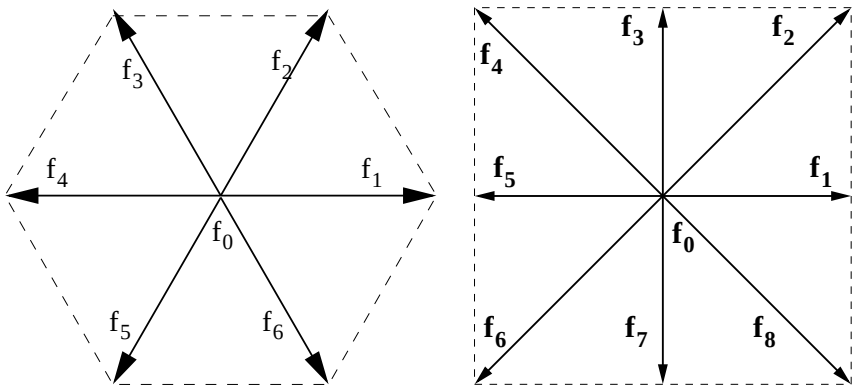

Figure 4.2: 2D lattice models

figuration. For example: D_2Q_9 is a common model of LB for the simulation of fluid in two dimensions. This configuration has the lattice site consisting of 9 velocities: 8 velocities corresponding to 8 directions of motion and one velocity describing particles at rest. The configuration is illustrated in the figure 4.2. Because of the square form, the configuration would create a lattice anisotropy, i.e. the length of diagonal directions is longer than the others which mean that the physical quantities might depend on the lattice orientation, if we did not treat the lattice directions correctly. This lattice isotropy is then solved by associating different weights to the directions of motion. Usually, the weights are interpreted as masses, denoted as m_i, associated with the particles travelling on each direction i [57]. The values of m_i are determined for each lattice configuration to give the appropriate masses.

In general model, $D_dQ_(z+1)$, the actual density is given as

$$\rho(\mathbf{r},t) = \sum_{i=0}^{z} m_i f_i(\mathbf{r},t). \tag{4.9}$$

The fluid velocity $\mathbf{u}(\mathbf{r},t)$ is defined through the momentum expression

$$\rho(\mathbf{r},t)\mathbf{u}(\mathbf{r},t) = \sum_{i=0}^{z} m_i f_i(\mathbf{r},t)\mathbf{v_i}. \tag{4.10}$$

Note that the lattice weights m_i are chosen to ensure the lattice isotropy which is actually related to the isotropy of its tensors. The weights m_i are chosen so

that the following relations hold

$$\sum_{i=1}^{z} m_i = C_0 \tag{4.11}$$

$$\sum_{i=1}^{z} m_i v_{i\alpha} v_{i\beta} = C_2 v^2 \delta_{\alpha\beta} \tag{4.12}$$

$$\sum_{i=1}^{z} m_i v_{i\alpha} v_{i\beta} v_{i\gamma} v_{i\delta} = C_4 v^4 (\delta_{\alpha\beta}\delta_{\gamma\delta} + \delta_{\alpha\gamma}\delta_{\beta\delta} + \delta_{\alpha\delta}\delta_{\beta\gamma}). \tag{4.13}$$

The coefficients C_0, C_2 and C_4 are defined through the lattice weights m_i and are determined numerically for a specific lattice [57].
Now, to make the dynamics of LBGK model, equation (4.8), simulate the fluid flow, the lattice Boltzmann dynamics should be derived in order to obtain the correct macroscopic behaviour. As we want to see the system at larger scales of space and time i.e. $L >> \Delta r$ and $T >> \Delta t$, it is usual to use the multi-scale Chapman-Enskog expansion for f_i in equation (4.8) [53]. The key point is now the choice of the equilibrium functions f^{eq}. With appropriate chosen equilibrium functions f^{eq}, one can recover the fluid governing equations from the lattice Boltzmann dynamics (i.e. the Navier-Stokes equation can be recovered exactly in the condition where Δr and Δt are chosen small enough so that f_i varies smoothly in space and time [55, 57, 63]).
The solution for the equilibrium functions has been proposed by [55, 57, 63, 65] and found to be an appropriate choice to simulate the fluid flow. It is given as

$$\begin{aligned} f_i^{eq} &= \rho\Big[\frac{1}{C_2}\frac{c_s^2}{v^2} + \frac{1}{C_2}\frac{v_{i\alpha}u_\alpha}{v^2} + \frac{1}{2C_4 v^4}\Big(v_{i\alpha}v_{i\beta} - v^2\frac{C_4}{C_2}\delta_{\alpha\beta}\Big)u_\alpha u_\beta\Big], \\ m_0 f_0^{eq} &= \rho\Big[1 - \frac{C_0}{C_2}\frac{c_s^2}{v^2} + \Big(\frac{C_0}{2C_2} - \frac{C_2}{2C_4}\Big)\frac{\mathbf{u}^2}{v^2}\Big], \end{aligned} \tag{4.14}$$

where v is the molecular velocity defined as $v = \Delta r/\Delta t$ and c_s is the speed of sound. Here we use the α and β to present spatial coordinates. The Einstein convention is used for repeating indices [1]. The detailed recovery, up to the order of $O(u^2)$, of the Navier-Stokes equation using LBGK model can be found in [57] and is written in complete form as

$$\begin{aligned} \partial_t \rho u_\alpha + \rho u_\beta \partial_\beta u_\alpha + u_\alpha \nabla\cdot(\rho\mathbf{u}) = -c_s^2\partial_\alpha\rho + v^2\Delta t\frac{C_4}{C_2}\Big(\tau - \frac{1}{2}\Big)\nabla^2\rho u_\alpha \\ + v^2\Delta t\Big(\tau - \frac{1}{2}\Big)\Big[2\frac{C_4}{C_2} - \frac{c_s^2}{v^2}\Big]\partial_\alpha\nabla\cdot(\rho\mathbf{u}). \end{aligned} \tag{4.15}$$

[1] Einstein convention $v_{i\alpha}u_\alpha = \sum_\alpha v_{i\alpha}u_\alpha$

In the incompressible limit (e.g. low Mach number), $\nabla\cdot(\rho\mathbf{u}) = 0$ then the equation (4.15) becomes the usual Navier-Stokes equation for the incompressible flow

$$\partial_t\mathbf{u} + (\mathbf{u}\cdot\nabla)\mathbf{u} = -\frac{1}{\rho}\nabla p + \nu\nabla^2\mathbf{u}. \tag{4.16}$$

p is a pressure term equal to

$$p = c_s^2\rho, \tag{4.17}$$

and ν is the kinematic viscosity of the fluid

$$\nu = v^2\Delta t\frac{C_4}{C_2}\Big(\tau - \frac{1}{2}\Big). \tag{4.18}$$

In equation (4.18), the relaxation time τ has to be greater than 0.5 in order to maintain the viscosity value positive. Experimentally, when the value of τ approaching a value lower than 0.6, the simulation may experience instabilities. For fluid simulations, a standard choice of c_s^2 equal to $c_s^2 = v^2C_4/C_2$, by replacing in the equation (4.14) one can obtain a reduced solution of f^{eq}

$$\begin{aligned} f_i^{eq} &= \rho\frac{C_4}{C_2^2}\Big[1 + \frac{v_{i\alpha}u_\alpha}{c_s^2} + \frac{1}{2}\Big(\frac{v_{i\alpha}u_\alpha}{c_s^2}\Big)^2 - \frac{\mathbf{u}^2}{2c_s^2}\Big], \\ m_0 f_0^{eq} &= \rho\Big(1 - \frac{C_0C_4}{C_2^2}\Big)\Big[1 - \frac{\mathbf{u}^2}{2c_s^2}\Big]. \end{aligned} \tag{4.19}$$

From the numerical point of view, it is faster to replace $f_i = m_i f_i$ and $f_i^{eq} = m_i f_i^{eq}$; then, the density and the momentum can be computed again as

$$\rho = \sum_{i=0}^{z} f_i, \tag{4.20}$$

$$\rho\mathbf{u} = \sum_{i=0}^{z} f_i v_i. \tag{4.21}$$

The equation (4.19) now becomes

$$\begin{aligned} f_i^{eq} &= \rho\Big(m_i\frac{C_4}{C_2^2}\Big)\Big[1 + \frac{v_{i\alpha}u_\alpha}{c_s^2} + \frac{1}{2}\Big(\frac{v_{i\alpha}u_\alpha}{c_s^2}\Big)^2 - \frac{\mathbf{u}^2}{2c_s^2}\Big], \\ f_0^{eq} &= \rho\Big(1 - \frac{C_0C_4}{C_2^2}\Big)\Big[1 - \frac{\mathbf{u}^2}{2c_s^2}\Big] \end{aligned} \tag{4.22}$$

or

$$\begin{aligned} f_i^{eq} &= \rho t_i\Big[1 + \frac{v_{i\alpha}u_\alpha}{c_s^2} + \frac{1}{2}\Big(\frac{v_{i\alpha}u_\alpha}{c_s^2}\Big)^2 - \frac{\mathbf{u}^2}{2c_s^2}\Big], \\ f_0^{eq} &= \rho t_0\Big[1 - \frac{\mathbf{u}^2}{2c_s^2}\Big], \end{aligned} \tag{4.23}$$

Model	Slow velocities			Fast velocities			C_0	C_2	C_4	c_s^2	t_0	Geometry
	$\|v_i\|$	m_i	t_i	$\|v_i\|$	m_i	t_i						
D2Q7	v	1	$\frac{1}{12}$				6	3	$\frac{3}{4}$	$\frac{1}{4}$	$\frac{1}{2}$	hex
D2Q9	v	4	$\frac{1}{9}$	$\sqrt{2}v$	1	$\frac{1}{36}$	20	12	4	$\frac{1}{3}$	$\frac{4}{9}$	square
D3Q15	v	1	$\frac{1}{9}$	$\sqrt{3}v$	$\frac{1}{8}$	$\frac{1}{72}$	7	3	1	$\frac{1}{3}$	$\frac{2}{9}$	cubic
D3Q19	v	2	$\frac{1}{18}$	$\sqrt{2}v$	1	$\frac{1}{36}$	24	12	4	$\frac{1}{3}$	$\frac{1}{3}$	cubic

Table 4.1: Lattice constants to compute f^{eq} for several LB models [57, 59]

where t_i is constant for each lattice

$$\begin{aligned} t_i &= m_i \frac{C_4}{C_2^2}, \\ t_0 &= 1 - \frac{C_0 C_4}{C_2^2}. \end{aligned} \tag{4.24}$$

The lattice constants and the coefficients m_i, t_i to compute f^{eq} for common lattices are summarised in the table 4.1. Some common lattice models of the lattice Boltzmann method are shown in the figures 4.2 and 4.3. Since there is an error stemming from the discretization of the lattice Boltzmann equation and the Navier-Stokes equation is recovered in the incompressible limit, we need to define two dimensionless parameters relevant to deriving the lattice Boltzmann equation. The Knudsen number is defined as the ratio of the lattice spacing over the characteristic length of the system $\epsilon = \Delta r/\mathcal{L}$, the Mach number as the ratio of the characteristic velocity of the fluid flow over the speed of sound c_s, $\mathcal{M} = \mathcal{U}/c_s$. In an analysis of accuracy and stability of the LBGK model [66], Reider and Sterling addressed the Knudsen number and the Mach number attached to the error terms i.e. the term $O(\epsilon^2)$ appears in the continuity equation and the terms $O(\epsilon^2)$ and $O(\mathcal{M}^3)$ appear in the Navier-Stoke equation. The term $O(\epsilon^2)$ is usually the discretization error while the actual Navier Stokes compressibility terms are attached to $O(\mathcal{M}^3)$. It appears that one recovers the incompressible Navier-Stokes equation only if the Mach and the Knudsen number are small enough to reduce the compressibility error. Thus, choosing a small Δr leads to a small Knudsen number and a discretization error; a small Δt makes a higher speed of sound c_s and consequently leads to a small Mach number. However, a small Δr would create a big domain of simulation and a small Δt may require a slow convergence to the stationary state (e.g. the slow convergence of body force); consequently, these require a lot of computation time. In a LB simulation, one

has to balance between the accuracy of simulation and the cost of computation.

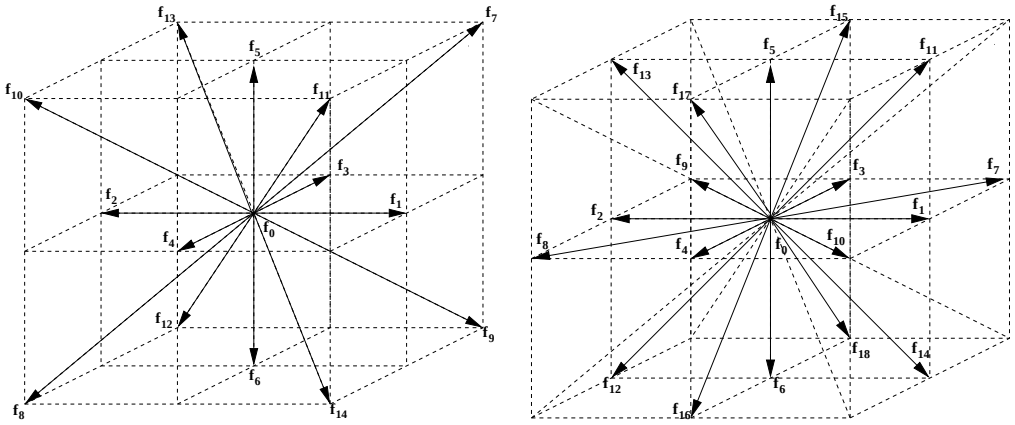

D_3Q_{15} D_3Q_{19}

Figure 4.3: 3D lattice models

4.3 Fluid acceleration and body force

In fluid flow simulation, it is necessary to initiate and accelerate the fluid to obtain the desired flow. For the implementation of lattice Boltzmann simulations, the flow can be accelerated in several ways including: body force, pressure gradient, velocity profile. Readers will find some details for fluid acceleration in [59]. Brief descriptions of these methods are summarised below and comparison between them are made for a given case of Poiseuille flow (in section 3.3).

Pressure gradient
The idea of a pressure gradient method is to maintain a pressure gradient ∇P between the inlet and the outlet of the flow. However, from the equation (4.17) for incompressible flow there is no density variation and thus the pressure gradient must remain constant. It raises the question of how to create the pressure gradient or "where does it come from?". The answer is that the pressure gradient is entirely due to the pressure fluctuations acting on top of a uniform pressure background [54]. Although the fluctuations of pressure violate the incompressibility rule and lead to compressibility error, as reported in [66], the convergence to incompressible equations can be obtained if the compressibility error is smaller than the discretization error. Thus, in some extents of lattice Boltzmann simulations, if we have small enough lattice spacing (discretization error), the pressure gradient can still be applicable. Practically, pressure gradient in LB simulations can be obtained by using the difference of fluid density between inlet and outlet

of the flow $\nabla\rho = \dfrac{\nabla P}{c_s^2}$.For an example of Poiseuille flow, the pressure gradient is implemented by imposing the lattice Boltzmann equation of the inlet of flow $\mathbf{r_{inlet}}$ as

$$f_i(\mathbf{r}_{inlet} + \Delta t\mathbf{v_i}, t + \Delta t) = \frac{1}{\tau}f_i^{eq}(\mathbf{r}_{inlet}, t) + (1 - \frac{1}{\tau})f_i(\mathbf{r}_{inlet}, t) + p_i \tag{4.25}$$

where p_i is a small quantity to present pressure gradient. Numerical results of Poiseuille flow show an artificial jump in density and velocity profile at the inlet.

Velocity profile
Velocity profile is another way to accelerate the flow. In general, the idea is to impose a velocity profile to a given position of flow, thus making the whole flow accelerate. Usually, the velocity profile is imposed at the inlet of the simulation domain by imposing a given velocity and density in the equation of equilibrium function (4.23). This implementation is easy. However, depending on the geometry and boundary condition of flow, it is necessary to treat the outlet of the flow to avoid numerical instability. The lattice Boltzmann equation for the inlet lattice sites can be written

$$f_i(\mathbf{r}_{inlet} + \Delta t\mathbf{v_i}, t + \Delta t) = \frac{1}{\tau}f_i^{eq}(\mathbf{u}_{inlet}, \rho_{inlet}) + (1 - \frac{1}{\tau})f_i(\mathbf{r}_{inlet}, t) \tag{4.26}$$

Again, numerical simulation of Poiseuille flow shows an artificial effect to velocity profile when using this way of acceleration.

Body force
More frequently than pressure gradient and velocity profile, body force is used as a common way to accelerate the flow. We can see it is quite natural to have a flow which is subject to an external force (e.g. gravitational force). This external force thus initiates the motion of the flow. When we look at the sedimentation processes, the sediments settle down under the gravitational effect, e.g. in a lake, fractal aggregates settle down because of gravitational force. This phenomena can be conveniently reproduced in simulations by using body force. The body force is implemented in the lattice Boltzmann simulations by imposing at each fluid lattice sites a constant quantity $\mathbf{F}$ which presents the body force. To include the body force in lattice Boltzmann equation, the equation (4.8) can be rewritten as

$$f_i(\mathbf{r} + \Delta t\mathbf{v_i}, t + \Delta t) = \frac{1}{\tau}f_i{}^{eq}(\mathbf{r}, t) + \big(1 - \frac{1}{\tau}\big)f_i(\mathbf{r}, t) + t_i\frac{\Delta t}{c_s^2}\mathbf{F}\cdot\mathbf{v_i} \tag{4.27}$$

or using the Einstein convention, equation (4.28) can be written as

$$f_i(\mathbf{r} + \Delta t\mathbf{v_i}, t + \Delta t) = \frac{1}{\tau}f_i{}^{eq}(\mathbf{r}, t) + \big(1 - \frac{1}{\tau}\big)f_i(\mathbf{r}, t) + t_i\frac{\Delta t C_2}{C_4 v^2}v_{i\alpha}F_\alpha \tag{4.28}$$

By including the body force this way, one can obtain the correct hydrodynamics and the resulting Navier Stokes equation in the correct form as

$$\partial_t \mathbf{u} + \mathbf{u} \cdot \nabla \mathbf{u} = -\frac{1}{\rho}\nabla P + \nu \nabla^2 \mathbf{u} + \frac{1}{\rho}\mathbf{F} \tag{4.29}$$

Detailed analysis can be found in [67]. Summing the equation (4.28) over i, one can see that the density of the system does not change. However, the momentum (obtained by multiplying with $v_{i\alpha}$ and summing over i) is increased to $\Delta t\mathbf{F}$ at each lattice site. It is worth noting that using body force is also a way to mimic the effect of pressure gradient without explicitly introducing density gradient. Under the body force, a pressure gradient is induced in the system as

$$\nabla P_\alpha = -F_\alpha \tag{4.30}$$

Accelerating fluid by including body force is appropriate for some simple flows e.g. Poiseuille flow and is supposed to work well with complicated ones at low Reynolds numbers. Numerical simulations of Poiseuille flow with body force do not experience artificial effects like pressure gradient and velocity profile approach. However, one can see in a simulation using body force, that it requires a lot of iterations to reach to the stationary state. The number of iterations is usually proportional to Reynolds fluid viscosity and thus Reynolds number. In an analysis of Poiseuille flow in [57], the time needed to reach the stationary state is proportional to the channel width square due to the fact that the Reynolds number is also proportional to this width of channel.

Discussion

It turns out that, using body force for accelerating the fluid is a good choice for our simulation since it is a natural way to mimic the gravitational effect and does not create artificial effects like other methods. In fact, it is a reasonable and convenient way for low Reynolds number flow simulations. Although, the disadvantage is that the body force is time consuming but we see later, with our simulations, that the method of body force is still acceptable.

4.4 Boundary conditions

In another issue of the lattice Boltzmann simulation, it is usual to simulate a flow having an interface between different mediums, e.g. solid-fluid interface of flow in a channel with solid walls or flow past a solid object. At this interface, behaviour of fluid-solid must be treated in suitable conditions. Also, the domain of a simulation is always finite, thus there are boundaries of the simulation domain which also need to be treated with appropriate conditions. The conditions

at the interfaces, boundaries ... etc are called boundary conditions. In the lattice Boltzmann simulations, one has to distinguish the boundary conditions at the interface, i.e. aiming to describe the behaviour of fluid between two mediums, with some special boundaries reference to the imposed conditions (e.g. a velocity profile is imposed at the boundary of the simulation domain in a lattice Boltzmann simulation). Here we look at the boundary conditions which describe the behaviour of the fluid at the interface or boundaries.
Boundary conditions have been discussed in various works; readers may refer to works such as [54, 56, 57, 59] for more details. Some specific analysis of given boundary conditions can also be found in [68–72]. In general, boundary conditions can be divided into some main categories: periodic, bounce-back, collision-at-boundary and interpolation boundary.

4.4.1 Periodic boundary

This is the simplest of the boundary conditions imaginable. This condition avoids the bulk phenomena from the actual boundaries of the physical system and is usually used when we are not interested in the effects of actual boundaries. In simulations, we always experience the finite size of the computational domain, thus the periodic boundary condition can give a way to simulate infinite systems as if finite physical boundaries are eliminated.
The principle of periodic boundary condition is simple: when a fluid comes to a boundary, it should then appear again in the system but from the opposite side. If we take an example of square simulation domain in 2D with all four boundaries set periodic, the implementation proceeds as follow: A fluid particle, in terms of fluid field f_i, entering the East boundary is set to appear from the West boundary in the next time step. In similar manner, a fluid field entering the North boundary should appear again from the South boundary in the next time step (as illustrated in figure 4.4). Technically, these operations of periodic boundary condition in a LB simulation are implemented in the propagation step.

4.4.2 Bounce-back boundary

This boundary condition is also one of the simple conditions in lattice Boltzmann simulations. In some works, its name occasionally refers to non-slip boundary conditions. The rule is simple: when a fluid comes to a boundary, it just bounces back to the position where it came from. In other words: bounce-back boundary simply reverses the direction of the fluid to the opposite position with the same velocity. The advantage of this boundary is its simplicity of implementation i.e. it does not need to know the shape of the boundary but only whether the point to which the fluid is going to is a boundary or not, thus it can be applied to any shape of boundaries without demanding any computation. There are 2 implementations of bounce-back boundary: **full-way** bounce-back and **half-way**

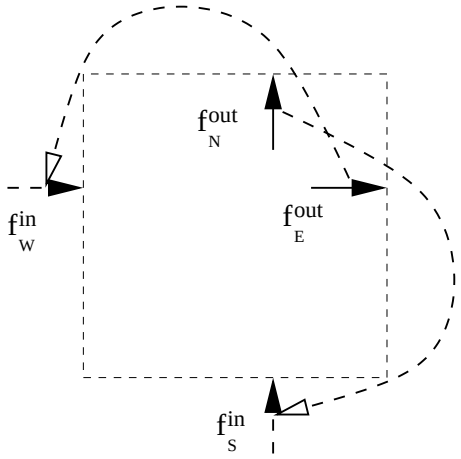

Figure 4.4: Periodic boundary condition

bounce-back. In full-way condition, the boundary is supposed to be located on the lattice sites, meaning that the lattice sites can be defined as the boundary and the bounce-back happens on the sites.

In a lattice Boltzmann simulation, if f_i is the fluid field entering a given boundary site Δr at a given time Δt , then in the collision step, the fluid field is set to reverse its direction and is sent back to the same position in propagation step as shown in figure 4.5. The implementation of lattice Boltzmann simulation is

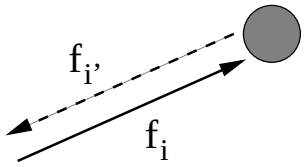

Figure 4.5: Full way bounce back

$$f_{i'}^{out} = f_i^{in} \tag{4.31}$$

where i' denotes the direction opposite to i and f_i^{in} and $f_{i'}^{out}$ denote incoming and outgoing fluid fields respectively. At the boundary sites, the collision phase is replaced by copying the fields to the opposite directions of the incoming fluid. Theoretical discussion and computational experiments indicate that full-way bounce-back introduces an error of first order in terms of lattice spacing, and it actually gives a zero velocity half-way between the bounce-back row and the first row in the flow.

In the second case, half-way bounce-back, the physical boundary is supposed to be located not on the lattice sites but between two of them; thus, in the LB simulation, the fluid field coming to the boundary is copied in the opposite direction as if it had returned to its original position in the same time step. According to the implementation of half-way bounce back, lattice sites of the actual boundary are not needed in computational domain.

Half-way bounce-back shows better accuracy than full-way bounce-back in some simple flow such as Poiseuille flow up to second order while full-way bounce-back

gives first order accuracy in terms of lattice spacing [57].
We can also observe that, the bounce-back boundary is mass conserving as it re-injects the same mass into the system after bouncing from the boundary. One expects in the simulation that the velocity on the boundary should be maintained at null, however, with the bounce-back scheme a slip velocity is observed along the boundary.
Despite its disadvantages, e.g. less accuracy in some flows, the bounce-back scheme is still attractive to simulate flows with complicated boundary shapes since it requires much less computation compared to other boundaries. In some evaluations, with more complicated flow than the Poiseuille, bounce-back boundary turns out to be reasonably accurate with easy implementation [73].

4.4.3 Collision-at-wall

This class of boundary conditions was categorised by Chopard et al [57], and here we again mention some essentials of typical boundaries. The idea of boundaries in this class is to suppress the slip velocity, as introduced in bounce-back condition, by applying a collision operator on it, as its name indicates. However, the collision operator cannot be easily applied in a straight-forward manner. At a given boundary site, there are always fluid fields coming from the fluid; fields coming from outside the system; or from neighbouring boundary sites. Those fields coming from outside or neighbouring boundary sites are clearly unknown. In order to perform correctly the collision, one has to properly define these unknown fields. There are several boundaries which propose how to define those unknown fields where the main idea is to impose zero slip velocity or to maintain mass conservation on the boundary.

Inamuro boundary

This boundary condition was developed by Inamuro et al [70] in which the unknown fluid fields are calculated by using an equilibrium distribution function with a counter slip velocity. This counter slip velocity is determined so that the fluid velocity at the boundary is equal to the boundary velocity. Based on this condition, a set of equations for unknown fields coming into the fluid can be formed using of two new quantities: counter slip velocity u' and a density ρ' whose solutions can be found. Thus, solutions of the unknown fluid fields can be calculated by solving this set of equations. The boundary condition has been introduced and developed for the D_2Q_9 model with a flat boundary. Experiments with Poiseuille flow has shown an accuracy with an exact solution up to the machine precision. In general, this boundary condition can be applied to other lattice models e.g. D_3Q_19, but limited to work only with flat boundaries as it is

very difficult to apply to more complicated situations such as stair case, corner, etc. Therefore it is not of interest for simulations with flows having complicated boundaries.

Mass conserving boundary

Although the Inamuro boundary showed excellent numerical results with simulation of Poiseuille flow, for other simulations of asymmetrical flows (e.g. cavity flow) the mass at the boundary is not conserved [59]. It has shown that, the mass is conserved at the boundary only if the flow is incompressible (where div$\rho u = 0$) and the orthogonal component of momentum gradient is null. To eliminate the slip velocity at the boundary while preserving the mass, Chopard et al [71] introduced a boundary condition named the mass-conserving boundary. The key point of this boundary is to conserve the mass coming into the boundary while maintaining the boundary velocity at zero. Based on this condition, the density of the boundary can be calculated simply from equilibrium functions and a set of equations is formed with respect to unknown fluid fields coming out to the fluid. Thus, by considering that the boundary fields (the fields going to another boundary site and not influencing the system) are free, we can choose their values so as to make the equations symmetrical, the solutions of the equations can be found.
This boundary has been developed for the D_2Q_9 lattice for several geometrical configurations and validated with Poiseuille flow. We here make a brief summary of the solutions and complete the work by adding our derivation for the case of corner. The first three configurations can also be found in [59].
Flat boundary.

$$\left.\begin{aligned} \rho_{in} &= f_2 + f_3 + f_4 \\ f_0 &= 0 \\ f_1 &= f_5 = 2\rho_{in} \\ f_6 &= f_2 \\ f_7 &= f_3 \\ f_8 &= f_4 \end{aligned}\right\} \tag{4.32}$$

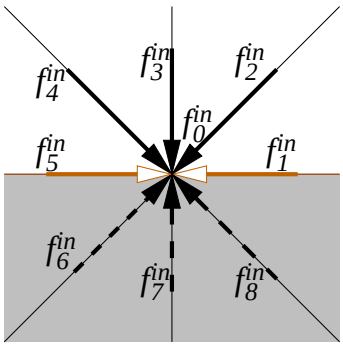

Figure 4.6: Flat boundary

Stair case boundary

$$\left.\begin{aligned} f_0 &= 0 \\ f_1 &= 8f_2 \\ f_3 &= f_7 \\ f_4 &= f_8 \\ f_5 &= 8f_2 \end{aligned}\right\} \tag{4.33}$$

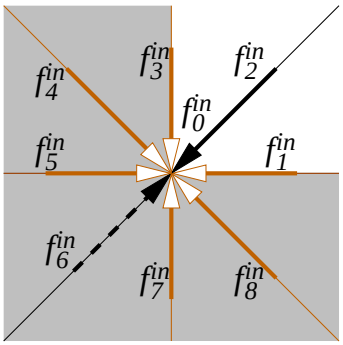

Figure 4.7: Stair case boundary

Steep corner

$$\left.\begin{aligned} f_0 &= \frac{8}{5}(f_8 + f_1 + f_2 + f_3) \\ f_4 &= f_8 \\ f_5 &= f_1 \\ f_6 &= f_2 \\ f_7 &= f_3 \end{aligned}\right\} \tag{4.34}$$

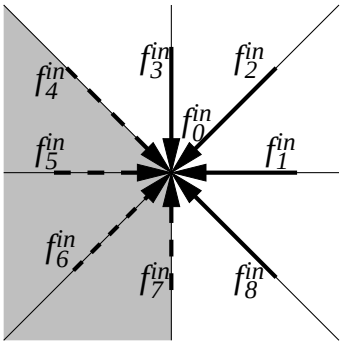

Figure 4.8: Steep corner

Note that, in the figures, the boundary is presented in gray colour. Black solid arrows show incoming fields to boundary while the dashed arrows show the fields going from the boundary to fluid. Gray solid arrows are boundary fields which go from one boundary site to another.
We complete the work by complementing the last configuration of mass conserving boundary for D_2Q_9 for the corner.

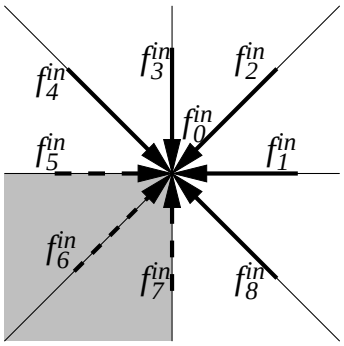

Figure 4.9: Corner boundary

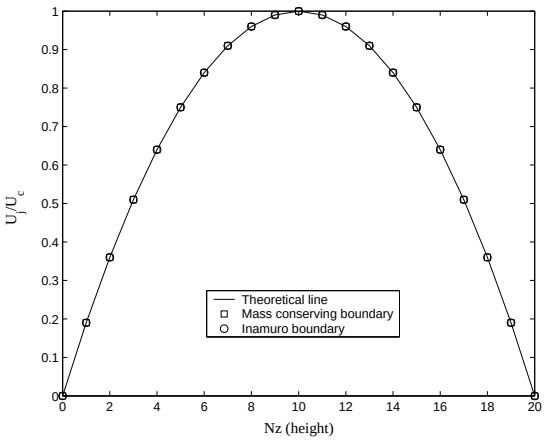

Figure 4.10: Velocity profile of Poiseuille flow using Inamuro and Mass conserving boundaries showing the exact theoretical velocity profile.

$$\left.\begin{aligned} f_0 &= 0 \\ f_5 &= \frac{1}{36\tau-25}\big((36\tau-11)f_1+14f_2+14f_3-(36\tau-50)f_4+36\tau f_8\big) \\ f_6 &= \frac{1}{36\tau-25}\big(-14f_1+(36\tau-39)f_2-14f_3-25f_4-25f_8\big) \\ f_7 &= \frac{1}{36\tau-25}\big(-14f_1+14f_2+(36\tau-11)f_3+36\tau f_4-(36\tau-50)f_8\big) \end{aligned}\right\} \quad (4.35)$$

Like the Inamuro boundary, the validation of mass conserving boundary, with simulation of Poiseuille flow, shows the same accuracy. Besides, it shows an improvement over the Inamuro boundary since the boundary can deal with some more complex shapes. The mass conserving boundary is reported to gain second-order accuracy in terms of lattice spacing for cavity flow. It is worth noting that the bounce-back boundary (full-way and half-way) also gains second-order numerical accuracy in space with cavity flow [59]. It implies that the convergence of bounce-back condition is not always first (or second) order, but depends also on given experiments.
Figure 4.10 shows velocity profiles of Poiseuille flow produced by mass conserving and Inamuro boundaries, both give exactly the theoretical profile.

Interpolation boundaries

These boundary conditions show another way of approximating the boundary where the main idea is to use interpolation. Usually, it is applicable to an off-lattice boundary (e.g. boundary moving off lattice sites and lying somewhere on the links between sites). For examples, the boundary conditions described

in [74, 75] showed interpolation procedures to estimate the fluid fields bounce-back on curved boundaries. The idea is to reconstruct the fluid fields which bounce-back on the boundary lying somewhere on the links. The values of these fields are interpolated with respect to the position of the real boundary on the link. However, numerical implementation of these boundaries is tedious [57] and requires much geometrical interpolation, thus making the computation more complicated than for other boundaries.

4.4.4 Discussion

From simulation of Poiseuille flow, the full-way bounce-back boundary is definitely less accurate when comparing it to the Inamuro or the mass-conserving boundary. However, this confirmation of accuracy is local and it is not clear how much the accuracy of bounce-back gains with other complicated flows. For bounce-back, the accuracy seems not to stem from its nature of bouncing back, since it has been pointed out that the accuracy is actually due to the location of the walls, where actual boundaries should be placed half-way along the wall site and fluid site. We also observe that, although the other boundaries give very accurate results, they require very heavy computation and too complicated treatments. It is not always possible for some boundaries. Thus, it makes the simulation very heavy and infeasible, especially for such simulations with complicated boundaries like fractal aggregates. In fact, we do not need such heavy boundaries in our simulations with fractal aggregates, but the bounce-back. Furthermore, the half-way bounce-back may not be needed, as in general, the exact location of boundary depends on the relaxation time [76] and is difficult to predict. However, several investigations have confirmed, e.g. simulations using impermeable spheres with the relaxation time staying between $0.7 \leq \tau \leq 1.3$ [76] or [73], the simple bounce-back gives quite satisfactory results. Hence, in chapter 5 we shall see that bounce-back does give very reasonable accuracy within the hydrodynamic regime simulation and even shows more advantages than mass-conserving. Supported by the results, we can conclude that, for irregular geometries like fractal aggregates, bounce-back is certainly an useful and reasonable choice.

4.5 Sources of error

Like other numerical methods of simulation, there are a number of sources of error that can affect the accuracy of a lattice Boltzmann simulation. Besides the inevitable error from the discreteness of the lattice model, like other numerical methods, the lattice Boltzmann simulation accuracy experiences other errors like compressibility, boundary implementation, etc. Main parameters contributing to the sources of error include the Mach number, spatial resolution and Knudsen number. Basically, it is not easy to separate the errors in a simulation; instead,

an estimation of the total error should be made. The goal is then to minimise this total error. However, in a simulation one has to compromise the contributing sources: reduce as much as possible the errors from the model like compressibility, discretization or boundary conditions while considering the cost and time of simulation. Therefore, understanding individual sources of error helps to adjust correctly and optimise the total error with regardless to the cost of simulation.

4.5.1 Compressibility errors

As mentioned previously, the compressibility errors originate from the fact that, the divergence of velocity $\nabla \cdot \mathbf{u}$ cannot be made completely zero (requires zero Mach number) and there is a variation of density caused by pressure gradient or body force (or otherwise). The compressibility errors in the lattice Boltzmann simulation is reported to attach to Mach number $O(M^3)$. Hence, to keep the flow incompressible and reduce the compressibility, one has to keep the Mach number as small as possible. Roughly speaking, when choosing $c_s^2 = \frac{1}{3}$ (for D_2Q_9 or D_3Q_19 model) in order to keep the compressibility error less than 1%, the average velocity should be kept roughly less than about 0.12. In addition, it has been proved in [77] that the flow is incompressible when $M < 0.3$ or flow velocity should be in the limit $u < 0.17$. Practically, in the lattice Boltzmann simulation, the limit of flow velocity should be kept at no more than 0.1 to ensure that the compressibility due to the flow velocity is negligible (less than 1%). However, in our lattice Boltzmann simulations, the measured velocity is usually of the order of 10^{-3} or less
Besides, in many flows, when including body force G we inevitably introduce a compressibility error into the system, as the body force actually induces a pressure gradient. Buick et al [78] has shown that the magnitude of body force should be limited in range so that it does not affect the incompressibility as the error terms is about $O(G)$. Thus the condition for the body force is introduced as $LG << c_s^2$ where L is the vertical extent of the simulation. Empirically, the body force injected into the system is maintained at less than 10^{-5} in our LB simulations.

4.5.2 Discretization errors

By discretization errors, we refer to the errors coming from the fact that the size of the simulation domain is limited and the discretization of objects in the simulation e.g. presentation of a curve is replaced by a set of discrete points. Like all grid-based models, any lattice Boltzmann simulation is a spatial approximation of the real domain, e.g. the channel (in Poiseuille flow) is presented as a number of discrete lattice points; thus discretization error due to this procedure is inevitable. This error is reduced when increasing the number of lattice points used

to present it. The error is found to relate to Knudsen number ϵ. The smaller the ϵ, the smoother the domain, and the smaller the error. Another discretization error comes from the discretization of objects presented in the simulation domain. In a simulation, it is quite usual to include objects in the fluid e.g. an impermeable sphere, and the objects are represented approximately by a set of grid points. Clearly, the curved boundaries of the objects are no longer continuous but replaced by a number of lattice points and segments. As an example: a cylinder in a flow past an array of cylinders would be represented in simulation as shown in figure 4.11. In fact, it is not easy to differentiate these discretization

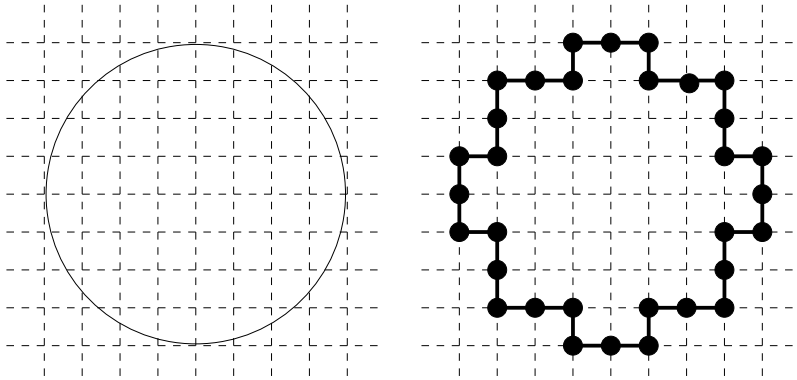

Figure 4.11: A cylinder is presented in a LB simulation

errors. We can see that, when the size of the objects is relatively proportional to the simulation domain, we should see both discretization errors as one and reduce it by refining the domain as smoothly as possible or in other word reducing ϵ as much as possible. Normally, one has to consider the balance between the cost of simulation and the size of the simulation domain (in lattice points).

4.5.3 Errors from implementation

Beside the compressibility and discretization errors, a lattice Boltzmann simulation also experiences errors from implementation including: boundary condition and the lattice model. As mentioned previously, the boundary condition could be seen as a considerable source of error depending on the flow, however it is an inevitable error and we should measure it during the simulations.
Besides, the accuracy of a simulation may also depend on the lattice models it uses. Several authors [69,79] have shown that in 2D simulations the lattice model D_2Q_9 is better and gives higher accuracy than D_2Q_7 in some experiments of cavity flow or Taylor vortex analysis; thus, D_2Q_9 becomes the choice for 2D simulations. Hence, like many discrete models, the lattice Boltzmann models and also LGA models contain some spurious invariants, namely staggered invariants [53]. These

invariants depend on the parity of space and time and may create some unphysical quantities. Although, there is no direct evidence of pernicious effects in fluid flow simulations [53], sometimes unwanted oscillations are created. An example would be the momentum of fluid particles, which may oscillate in time scale [76]. This can be reduced by using proper initial conditions and averaging over several time steps. Hence, there is also an existence of a spurious invariant, directly related to checker-board structure of lattice model. The checker-board effect is visible in several lattice model i.e. it has been confirmed, in the simulation of fluid flow around a sphere by Kandhai et al [76], that the D_3Q_{15} model contains the checker-board effect. The model D_3Q_{19} however does not suffer from this effect.
The checker-board effect can be demonstrated in our simulation of flow in a pipe. We use both D_3Q_{15} and D_3Q_{19} in a simulation of flow at low Reynolds number in a pipe having diameter of 19 lattice spacing. Flow is accelerated using total body force $G_x = 0.05$ along x direction. Bounce-back is applied on the boundary of the pipe and the pipe is set to be periodic along x direction. Velocity profile of flow at the middle of the pipe is extracted and shown in the figure 4.12. While the

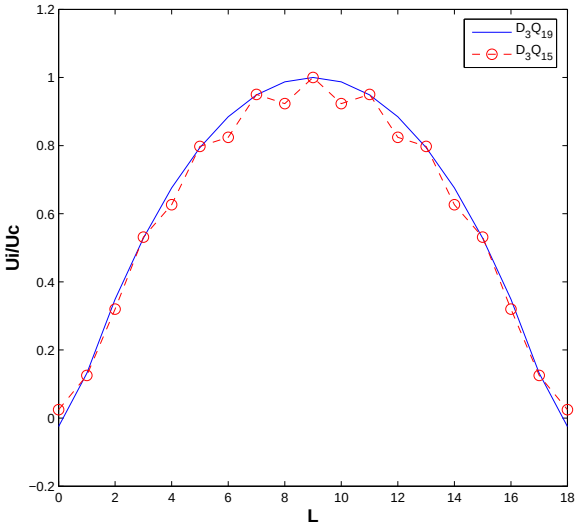

Figure 4.12: Checker-board effect is visible in simulation of flow in a pipe using D_3Q_{15} but not for D_3Q_{19} model.

D_3Q_{19} model gives a smooth velocity profile, the D_3Q_{15} shows a rugged velocity profile due to the checker-board effect. For 3D simulations, certainly D_3Q_{19} is a better choice than D_3Q_{15}.
Another benchmark of our simulations in 3D using both D_3Q_{19} and D_3Q_{27} models is implemented for Poiseuille flow with two parallel walls. The simulations are

made on a domain of $27 \times 27 \times 27$ lattice nodes using body force and bounce-back rule on the walls. We measure the update time for each iteration in both models and find that D_3Q_{19} model is approximately 42% faster than D_3Q_{27}. We also measure the average volumetric difference in the velocity field of simulation in both models. After 3000 iterations, the average volumetric difference of the velocity field is about 0.5% between the two models. Although this difference is local to Poiseuille flow and to a given time, we can see that the difference in accuracy between them is quite small. It demonstrates that the D_3Q_{19} is a good balance between stability and computational efficiency. Therefore D_3Q_{19} model is also a reasonable choice over the D_3Q_{27} model for 3D simulations.

4.5.4 Discussion

As the errors in a lattice Boltzmann simulation come from several sources and are difficult to separate, one should estimate a total error rather than estimate them separately. Thus the quality of the simulation is controlled by keeping the total error at an acceptable level. However, some lower limits of velocity and grid resolution, as well as body force must be obeyed to ensure the validity of Navier-Stokes equation and the meaning of the simulation.

4.6 Summary

In this chapter, we have presented the lattice Boltzmann method for fluid flow simulations. The idea of the lattice Boltzmann method is to represent the fluid on a discretized lattice, where space and time are fully discrete like the LGA method. Unlike LGA, the lattice Boltzmann model describes the fluid in terms of the probability of the presence of fluid particles (fluid fields) f entering (or exiting) a lattice site $\mathbf{r}$ with a given velocity v. The lattice Boltzmann method shows advantages over the LGA method since it reduces considerably the statistical noises and the fluid is simulated more efficiently. Thus, the lattice BGK, using a single relaxation time, can reduce very much the computation of the collision operator. It recovers, up to second order of $O(u^2)$, the continuity and the Navier-Stokes equation. It turns out to be a good model for directly simulating low Reynolds number flows. After that, a review of the boundary conditions in the lattice Boltzmann simulation has been made where we compared the accuracy of the bounce-back, the Inamuro and the mass conserving boundaries using the simulation of Poiseuille flow. We also completed the development for the mass conserving boundary with the case of corner. However, it turns out that for highly irregular geometries like fractal aggregates, the bounce-back is certainly the best candidate. Other boundaries like the Inamuro or the mass-conserving boundary require a lot of computational treatments or are simply impossible. In the simulation of Poiseuille flow, the bounce-back gives a first-order of accuracy

but for other complicated flows, it does give quite satisfactory accuracy, according to some previous studies.
The fluid acceleration has also been considered. We found that for small Reynolds number flows, the body force substitutes well to the pressure gradient and the velocity profile. In addition, the pressure gradient explicitly introduces a compressibility error and the velocity profile certainly introduces an artifact in the density profile. Furthermore, using the body force is an easy way to mimic the gravitational effect.
To sum up the chapter, we addressed several error sources in a lattice Boltzmann simulation. The compressibility and the discretization errors can certainly be reduced by using appropriate parameters, i.e. the flow velocity is kept small in order to obtain a small Mach number while the size of simulation domain (in terms of number of lattice spacing) is large enough. The boundary condition is clearly a source of error, however, it is inevitable and we must quantify these by implementing simulations for given cases. Hence, the lattice model should be used with care due to the fact that some models can give less accuracy than others or contain staggered invariants. For 2D simulations, a reasonable choice is the D_2Q_9 model, since it is easier to do programming with. This model has confirmed to give higher accuracy than the D_2Q_7 model, in some experiments. In 3D the D_3Q_{19} should be the choice as it does not exhibit the checker-board effect like D_3Q_{15}. It also requires less computation than the D_3Q_{27} model. Finally, in our simulations, we would estimate the total error and keep it at an acceptable level rather than estimating the errors separately.

Chapter 5

Hydrodynamics of fractal aggregates in 2D

5.1 Introduction

In this chapter, we start our investigations of the hydrodynamic properties of fractal aggregates using lattice Boltzmann simulations in 2D. The goal is to understand the effect of the fractal shape on hydrodynamic quantities such as: the drag force, the flow velocity, etc. of fractal aggregates. This is an initial step before investigating the hydrodynamics of 3D fractal aggregates which have more realistic structures.
The hydrodynamics is determined by investigating the flow around fractal aggregates. This flow is produced at very low Reynolds number, $Re \sim 0.2$ or less. Obviously, one can see that the ideal model to investigate the hydrodynamic behaviour of a fractal aggregate would be to put it in an infinite domain, with a flow around it. However, this is not possible as the simulation domain size is always finite on a computer. Then, the hydrodynamic quantities we measure from the simulation suffer from this finite size problem: the effect of the boundaries (if we set up boundaries to limit the flow) or the effect from other mirror fractal aggregates (if we let the boundaries be periodic then the situation becomes a flow past an array of fractal aggregates). These effects are always visible even in large domains of simulation due to Stokes paradox [51]. Hence, analytical solutions for estimating these effects are not available. If we limit the domain to two parallel walls, one does not know exactly how to compensate the effects of these walls on the results. Similarly, if we remove the walls and let the phenomenon become the flow past an array of fractal aggregates, then the interaction of one aggregate with others must be considered. However, for the case of cylinders, an analytical solution has been made by Sangani et al [80] in which the mutual effect between mirror cylinders is estimated. Thus, as a reference system, it can give a way to determine the hydrodynamics of fractal aggregates. In this chap-

ter, we first validate our lattice Boltzmann model with the analytical solution of Sangani et al by reproducing the simulation of the flow past an array of cylinders. An estimation of the total error of the lattice Boltzmann simulation is made by considering the deviation with the analytical solution. We then restrict the simulations with fractal aggregates in conditions used where the total error is acceptable. The investigation with fractal aggregates is implemented to find the role of fractal shapes on the drag force, the fluid velocity, etc. for both DLA and RLA fractal aggregates. Hydrodynamic properties of these fractal aggregates are also addressed by considering the ratio of $\frac{R_h}{R_g}$ and its relation to fractal compacity (or the fractal dimension).

5.2 Slow flow past an array of impermeable cylinders

5.2.1 The analytical solution for the flow past a square array of cylinders

The analytical solution for a flow past an array of cylinder has been studied by Sangani et al [80] for the case of dilute arrays. The solution has been found based on numerical approximations from the solution of creeping flows. The drag force and the average velocity of the flow were estimated up to a fourth order accuracy in terms of the volume fraction $O(c^4)$. For detailed derivation of this analytical solution, readers can refer to the article of Sangani et al [80]. This problem obviously can be reproduced again by our lattice Boltzmann simulation. We consider a slow and steady motion of an incompressible viscous fluid through a periodic square array of impermeable cylinders. The cylinder has a radius a and the distance centre-to-centre between two adjacent cylinders is noted as l. u is the average flow velocity and the flow is assumed to direction x. Clearly, the interaction of a cylinder with others in the array should be considered in the flow solution. As the Reynolds number is very small, the equations of the flow are then reduced to the creeping flow equations where Sangani et al present them in terms of a stream function ϕ and a vorticity ω.

$$\nabla^2\phi = \omega \tag{5.1}$$

$$\nabla^2\omega = 0 \tag{5.2}$$

The stream function ϕ and the vorticity ω are determined numerically by applying the Taylor series expansion. This expansion is implemented on ϕ around the surface position of the cylinder, i.e. $r = a$. The solutions for ϕ and ω, found from the expansion as infinite series, are then truncated to a finite number of terms with N unknown coefficients. Using the boundary conditions and several

approximations, i.e. the symmetry of flow and the no-slip boundary condition applied on the surface of the cylinder, a system of equations is formulated to solve the unknown coefficients in the series where the number of equations M is larger than the number of unknowns (coefficients). Sangani et al determined the unknown coefficients in the sense of least-square using the method by Forsythe [80]. Having found the coefficients in the series for the stream function ϕ and the vorticity ω, the connection between the drag force and the average velocity of the flow can be formed, according to [80], as

$$\frac{F}{\mu u} = a \int_0^{2\pi} (\omega sin\theta - Pcos\theta) d\theta \tag{5.3}$$

where F is measured as the force per unit length on the cylinder exerted by the flow, μ is the fluid viscosity, and P is the fluid pressure. The value $\frac{F}{\mu u}$ has been estimated numerically for different a. Actually, it is preferable to present a in terms of a volume fraction c. The volume fraction c is defined as a ratio of the volume of the cylinder over the total volume of the unit cell (or domain)

$$c = \frac{\pi a^2}{4} \tag{5.4}$$

if we consider the volume of the domain to be unit. The numerical values of $\frac{F}{\mu u}$ obtained by Sangani et al for different values of c have then led to two analytical solutions corresponding to two situations of c that accommodate the numerical results.

1. When the arrays are dilute $c << 1$, then

$$\frac{F}{\mu u} = \frac{4\pi}{\ln c^{-1/2} - 0.738 + c - 0.887c^2 + 2.038c^3 + O(c^4)} \tag{5.5}$$

2. When the arrays are concentrated, the approximation is given by

$$\frac{F}{\mu u} \sim \frac{9\pi}{2}\sqrt{2}\big[1 - \big(\frac{c}{c_{max}}\big)^{(1/2)}\big]^{(-5/2)} \tag{5.6}$$

given that $c_{max} - c << 1$ where c_{max} is the volume fraction when the cylinders are touching each other.

5.2.2 Simulation of the flow past an array of cylinders

The simulation is set up on a square lattice with an impermeable cylinder of a radius r placed at the centre of the lattice. Since the lattice boundaries are fully periodic, a flow past a square array of cylinders is achieved as shown in figure 5.1.

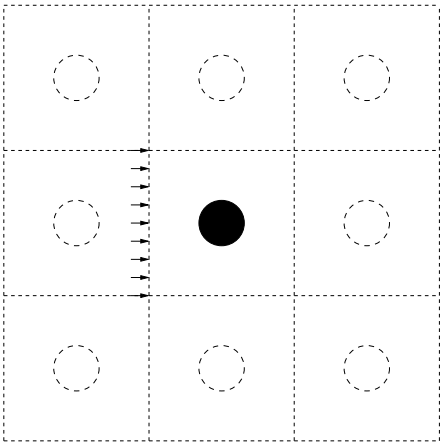

Figure 5.1: Flow past an array of impermeable cylinders in a lattice Boltzmann simulation

The bounce-back rule is applied on the surface of the cylinder and a body force $F_b = (G, 0)$ is applied to accelerate the fluid, i.e. the body force acts on every single fluid particle to x direction. Under the effect of the body force each fluid particle, coming to the cylinder, has a momentum of $f_i\mathbf{v_i}$. When colliding on a surface of the cylinder, the fluid particle holds a momentum of $-f_i\mathbf{v_i}$ due to the reverse of the velocity. Thus, it yields a momentum exchange on the surface equal to $2f_i\mathbf{v_i}$. Summing all momentum exchanges over the surface of the cylinder, it actually gives the drag force F_D of the fluid acting on the cylinder

$$F_D = \sum_{\mathbf{r_s}} \sum_i 2f_i(\mathbf{r_s})\mathbf{v_i} \tag{5.7}$$

where $\mathbf{r_s}$ designates the sites on the cylinder surface. We can see that the drag force in the lattice Boltzmann simulation is calculated very easily with the bounce-back rule. This is also considered as an advantage of the bounce-back boundary. With other boundaries, the drag force may require a more complicated calculation. We denote F_{TB} as the amount of the momentum injected into the system by the body force which is calculated as the sum of body force over all fluid particles as

$$F_{TB} = \sum_{\mathbf{r_f}} F_b \tag{5.8}$$

where $\mathbf{r_f}$ labels the fluid sites. In the stationary regime, this total body force F_{TB} should be equal to the momentum adsorbed by the cylinder. The latter is precisely the drag force F_D. Then, in the stationary regime we have

$$F_D = F_{TB} = \sum_{\mathbf{r_f}} F_b \tag{5.9}$$

Equation (5.9) is illustrated in figure 5.2. One can see from the equation (5.9) that the drag force is a good control parameter in the simulation. The total

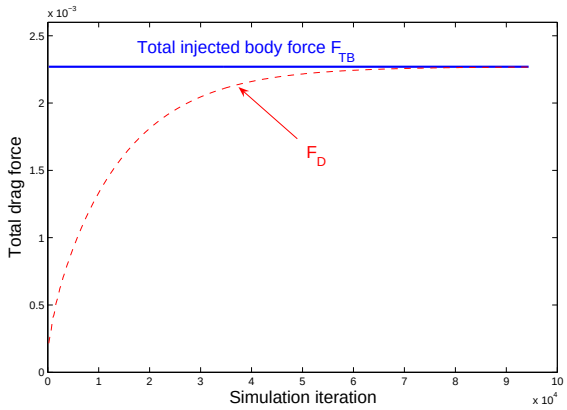

Figure 5.2: Development of total drag force on the cylinder with an applied body force. In the stationary regime, the drag force F_D is equal to the total injected body force F_{TB}.

force acting on the cylinder in the stationary regime amounts to F including the drag force F_D and the buoyancy force F_{BC} (caused by the body force acting on the fluid) [81]. Numerically, this buoyancy force is calculated by multiplying the body force F_b with the number of lattice sites representing the cylinder, hence

$$F_{BC} = \sum_{\mathbf{r_c}} F_b \tag{5.10}$$

where $\mathbf{r_c}$ indicates the sites belonging to the cylinder. Finally, total force acting on the cylinder is computed as

$$\begin{aligned} F = F_D + F_{BC} &= \sum_{\mathbf{r_s}} \sum_{i} 2 f_i(\mathbf{r_s}) \mathbf{v_i} + \sum_{\mathbf{r_c}} F_b \\ &= \sum_{\mathbf{r_f}} F_b + \sum_{\mathbf{r_c}} F_b \\ &= \sum_{\mathbf{r} \in V} F_b \end{aligned} \tag{5.11}$$

where V labels the total volume of the system. The total force F of the fluid acting on the cylinder can be computed by multiplying the body force acting on one fluid site, with the total number of lattice sites in the system including both the fluid and the solid (cylinder) sites.
The average velocity of flow u can be calculated by averaging the velocity of fluid particles vertically at any position of x direction, e.g. in our simulation, the

velocity is chosen to be averaged at the outlet of the flow. In order to reduce the compressibility error (influences on fluid density and thus the viscosity, as $\mu = \rho\nu$), the viscosity μ of the fluid is also estimated in the same manner by averaging vertically at the outlet of the flow.

The discretization effect of the cylinder

As the cylinder is presented in the simulation discretely, we want to know the effect of the discretization of the cylinder on our measurements. In the simulation, the cylinder is discretized by a number of lattice sites, which consequently makes the cylinder shape not perfectly circular. The bigger the radius of the cylinder, the more continuous shape the cylinder has and the smaller the error due to the discretization. Therefore, a minimum size of the cylinder should be determined above which the discretization error in the simulation becomes negligible. Here we study the sensitivity of the drag force and the velocity to this discretization of the cylinder and the convergence of the discretization error with the radius of the cylinder. The analytical solution of Sangani is used to quantify the error.First, we keep the volume fraction of the cylinder small so that the error accommodating inside the analytical solution $O(c^4)$ disappears (i.e. c is chosen to be equal to 0.05 then the error reduced to less than 0.0001%). We then perform many simulations in which we keep the same volume fraction while increasing the system volume or system size L (the radius of the cylinder r increasing accordingly). The Reynolds number of the simulations is kept as low as 0.2. The total force acting on the cylinder, the average velocity and the viscosity are computed from the simulations. Finally, the error is estimated as

$$e = \Big|\frac{F}{\mu u} - \frac{4\pi}{\ln c^{1/2} - 0.738 + c - 0.887c^2 + 2.038c^3}\Big|. \tag{5.12}$$

The estimation is shown in figure 5.3. We observe that the error due to the discretization of the cylinder is decreasing quickly with an increment of the cylinder radius. Between $r = 6$ and $r = 7$ lattice spacing, there is an error of about 0.1%. Hence, for cylinders having a radius bigger than 8, the total error in the simulation comes only from the effects of the volume fraction and the boundary condition.

The effect of the volume fraction

We shall now determine the limit of the volume fraction for the lattice Boltzmann simulation where the deviation from the analytical solution of Sangani et al is still acceptable. This limit is used for making simulations with fractal aggregates.

We take a large cylinder in our simulations with $r = 15$ lattice spacing, so that the discretization error of the cylinder is negligible. A number of simulations

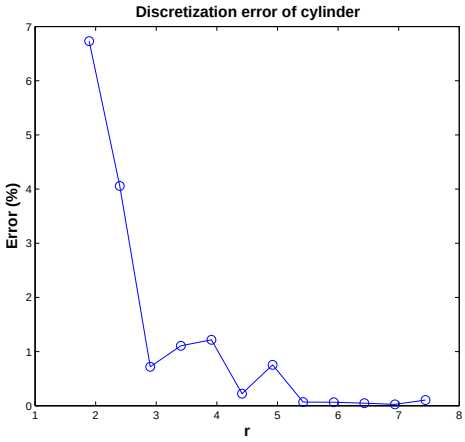

Figure 5.3: Error from discretization of cylinder quickly decreases with an increment of cylinder radius

is implemented for a range of the volume fraction from $c = 0.43 - 0.02$. The volume fraction is adjusted by changing the size of the simulation domain, i.e. $N_x \times N_y = 41 \times 41$ to $N_x \times N_y = 153 \times 153$ cells, while keeping the cylinder radius constant. The total error of the simulation, compared to the analytical solution, mainly comes from the boundary condition. The Reynolds number is still equal to or lower than 0.2. In this experiment both, bounce-back and mass-conserving boundary, are used on the surface of the cylinder, respectively. We want to compare their accuracy. Figure 5.4 shows our simulation results, where we observe that below the volume fraction $c = 0.25$, the results of the lattice Boltzmann simulations agree very well with the analytical solution for both boundaries. From $c = 0.3$, the analytical solution starts breaking and departing from the simulation curves. This is not surprising as the solution of Sangani et al works solely under dilute conditions $c << 1$. We estimate the error between our lattice Boltzmann simulations and the analytical solution like in equation (5.12). We observe that both boundaries give the results which converge to the analytical solution. Within the validity of the solution $c < 0.25$, it is interesting to see that the bounce-back boundary results show a better agreement and converge faster than the ones from the mass conserving boundary. We can also see from the results that the mass conserving boundary seems to under-estimate the drag force in comparison to the analytical solution. Figure 5.5 illustrates the accuracy of the lattice Boltzmann simulations for both boundaries (numerical results can be found in Appendix B). With a volume fraction less than 0.15, simulations using the bounce-back boundary present an error less than 1% while the mass-conserving boundary gives an error of about 5%. Moreover, the implementation of the bounce-back is much simpler and faster than that of the mass conserving

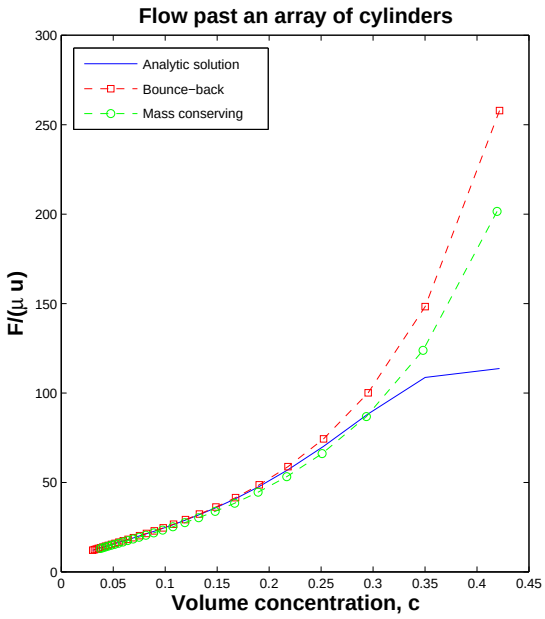

Figure 5.4: LB simulation results compared to the analytical solution. At a volume fraction less than 0.25, simulation results agree well with the analytical solution.

boundary. The obtained results confirm that the bounce-back boundary is a good and convenient choice for our simulations. It is also evidence that for some complex geometries, the bounce-back still offers us a good solution.

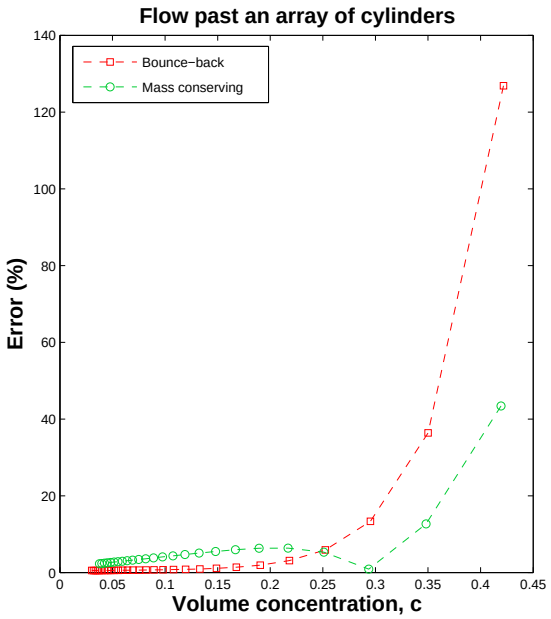

Figure 5.5: The accuracy of LB simulations using both bounce-back and mass conserving boundaries is obtained from a comparison with the Sangani solution for flow past an array of cylinder. Bounce-back (red) shows better convergence and accuracy than mass conserving (green).

5.3 Hydrodynamics of fractal aggregates in 2D

We now consider fractal aggregates in the flow instead of cylinders. The flow is simulated to pass through an array of fractal aggregates at small Reynolds numbers like before. We assume that the effect of the volume fraction in the case of fractal aggregates behaves similar to the case of cylinders. Therefore, at low volume fraction values, the total error in the simulation is small. In our simulations, fractal aggregates are composed of many elementary particles located on the lattice sites. They are obtained by simulating a lattice DLA (diffusion limited aggregation) process. For the sake of simplicity, we also assume that the particles making up the fractal aggregates are point-like and occupy one lattice site. For simulations with fractal aggregates, this assumption is comfortable enough because: (1) the fractal aggregates are well defined in the system; (2) the effect of elementary particle size of the fractal aggregates in lattice Boltzmann simulations is less important than the overall structure; simulations with an ideal fractal aggregate in which its elementary particle is point-like as shown in figure 5.6(a) has resulted in a difference of 5.9% in $\frac{F}{(\mu u)}$ compared to the same aggregate having elementary particles composed of 21-lattice points as shown in figure 5.6(b). (3)

an increment in size of the elementary particle will result in a huge increment in the simulation domain and makes the simulations beyond the CPU and memory limits of the computer.

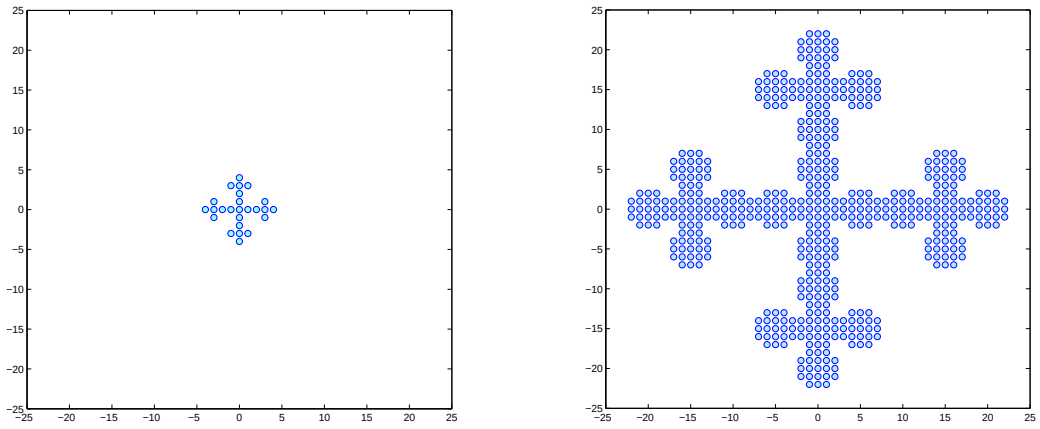

(a) (b)

Figure 5.6: Ideal fractal aggregates have their elementary particles composed of 1-lattice site and 21-lattice sites

And now we want to investigate the effect of fractal geometry on the drag force.

5.3.1 The role of external geometry of fractal aggregates

In the preliminary experiments, we consider small fractal objects, i.e. aggregates having 100 or 200 particles. Figure 5.7 shows the 100-particle fractal and its effect on the velocity of fluid. We proceed with our investigations by comparing

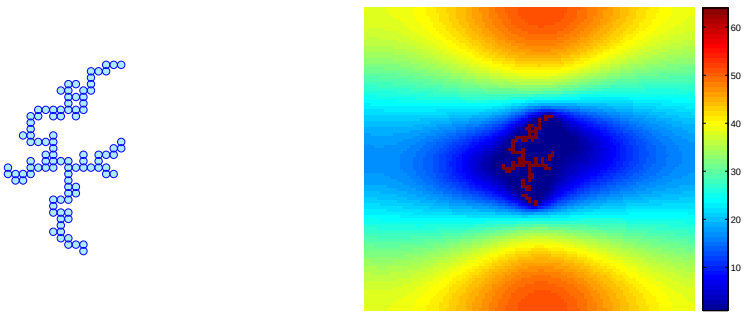

Figure 5.7: Fractal aggregate used for the simulation and the resulting intensity of the flow speed.

the drag force experienced by the aggregate as a function of its orientation with the main flow. We consider only four orientations, namely the reference position, the rotation by $\pi/2$, π and $3\pi/2$.
As before, we impose the drag force F_D on the system by applying a body force on the fluid and we measure the resulting average flow velocity u (which is computed by averaging the velocity vertically at the outlet) of the flow in the system. Figure 5.8 shows that the relation between F_D and u is almost linear, as expected for a low volume fraction c, but that the proportionality coefficient F_D/u depends on the orientation of the fractal object. In addition, we observe that the behaviour is the same whether the object is rotated by 180^o or not. The relation $F_D - u$ produced by rotating the fractal aggregate π falls exactly on that of the reference position. In other word, the hydrodynamic behaviour of the fractal aggregate is exactly the same for both reference position and rotated π position. However, it differs when we rotate the fractal aggregate $\pi/2$.
These results suggest that the hydrodynamic resistance of the fractal object to the fluid motion depends mostly on its cross section orthogonal to the flow direction. However, as shown in figure 5.9, results from simulations with a plate orthogonal to the flow direction and having the same width as the projection of the fractal aggregate do not show the same behaviour. A plate offers less resistance to the flow than the fractal object. This is due to the fact that the length of the obstacle along the flow direction also plays a role, but to a lesser extent than the perpendicular extension. Therefore, we also compare the drag force on rectangular objects having the same length and width as the fractal object. The plots shown in figure 5.9 indicate that the rectangle now over-estimates the drag force.

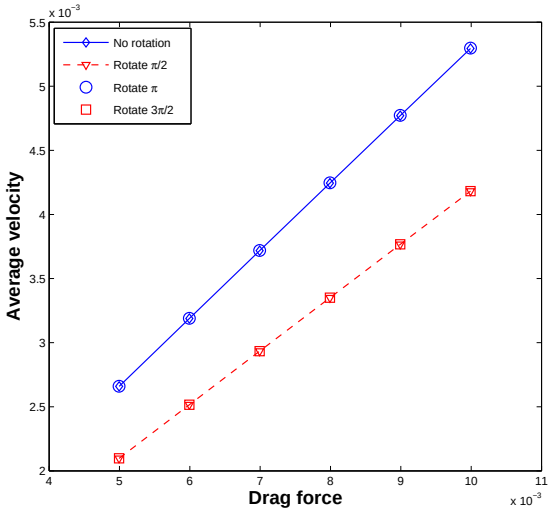

Figure 5.8: Velocity u versus the drag force F_D for different orientation of the fractal aggregate.

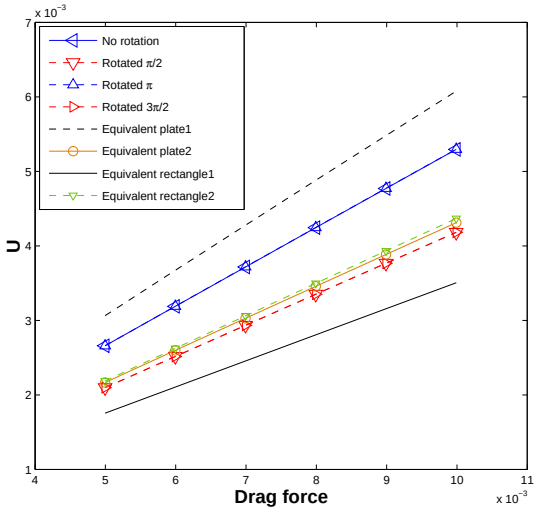

Figure 5.9: Variation of average velocity with drag force for various 2D objects.

Nevertheless, it clearly appears from the simulation that the speed of the fluid inside the aggregate is almost zero. Therefore, in 2D, the hydrodynamic properties of a fractal object are mostly determined by its outer shape and not its internal structure. We believe that, in 2D, the convex hull of the fractal object would give a good approximation of the hydrodynamic behaviour. This observation is also consistent with the results by A. Adrover and M. Giona [42].

5.3.2 Hydrodynamic radius

For a real fractal aggregate, the force F acting on it and the settling velocity u can be expressed in terms of the hydrodynamic radius R_h, which is in fact the radius of a sphere experiencing the same force while moving with the same velocity without any of the effects of boundaries. However, in 2D case, the definition of hydrodynamic radius for fractal aggregates is not defined. Usually, we can imitate the definition of the hydrodynamic radius for a 2D fractal aggregate as a radius of a 2D cylinder immersed in a fluid while experiencing the same force from flow and producing the same velocity. However, the presence of the Stokes paradox in 2D makes the effects of boundaries always visible, i.e. the size (or the volume fraction) of the cylinder in a domain has a very long range effect even when it is placed in a very large domain. It is also expressed in the solution of Sangani-Acrivos (5.5). Clearly, when volume fraction $c \to 0$ (the cylinder is placed in an infinite domain), then $\dfrac{F}{\mu u} \to 0$ does not show any information of hydrodynamic radius. In addition, the term $\log(c^{-1/2})$ does not give a meaningful value when $c = 0$, meaning that c should always be considered.
Here, we do not repeat the same definition of hydrodynamic radius of the fractal aggregate as in a 3D case. We specify that the radius of a 2D cylinder (or a disc), which experiences the same drag force F and produce the same velocity speed u in any simulation domain, is the hydrodynamic radius of the fractal aggregate. It is worth noting that, we do not idealise the definition in the infinite domain since the size of the cylinder is always meaningful in the system. Although the definition is not trivial, our results will show that the hydrodynamic radius can still be found from simulations.
Now, we introduce a procedure to determine numerically the hydrodynamic radius of fractal aggregates from our lattice Boltzmann simulations.
Recall the solution of Sangani-Acrivos for the case of cylinders, the relation of total force acting on the cylinder with the average velocity with volume fraction holds

$$\frac{F}{\mu u} = \frac{4\pi}{\ln c^{-1/2} - 0.738 + c - 0.887c^2 + 2.038c^3 + O(c^4)}$$

Figure 5.10(a) shows the $\dfrac{F}{\mu u}$ values obtained from the lattice Boltzmann simulation with the Sangani-Acrivos solution. For the fractal aggregates, the relation

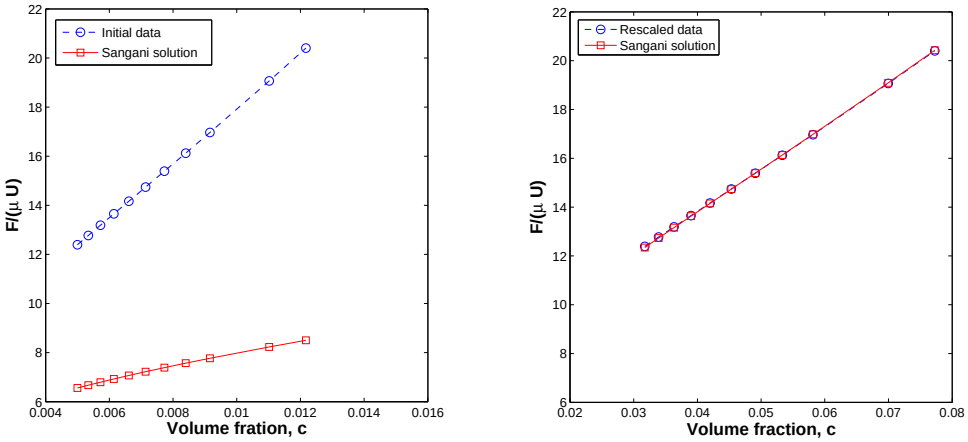

(a) (b)

Figure 5.10: (a) The LB simulation data for a RLA fractal aggregate (N=300). (b) Rescaling c results simulation data collapses on Sangani-Acrivos solution.

(5.5) is no longer obeyed. We see that $\frac{F}{\mu u}$ does not depend on the radius of cylinder but only on the volume fraction c. Thus, we introduce a rescaling defined by $c \rightarrow \beta c$. The goal is to optimise β so that the $\frac{F}{\mu u}$ values measured from simulation collapse on the Sangani-Acrivos solution. Let

$$\mathbf{K} = \frac{F}{\mu u}$$

be the data vector from simulation and

$$\mathbf{SA}(c) = \frac{4\pi}{\ln c^{-1/2} - 0.738 + c - 0.887c^2 + 2.038c^3}$$

the function of Sangani-Acrivos. The rescaling procedure now becomes a minimisation problem as

$$\min f = \sum \left| \mathbf{K} - \mathbf{SA}(\beta c) \right|^2 \tag{5.13}$$

can be found as

$$\frac{\partial f}{\partial \beta} = 0. \tag{5.14}$$

By solving the minimisation problem, an appropriate β can be found. Figure 5.10(b) shows the rescaled data to rest on the Sangani-Acrivos solution. Then, the hydrodynamic radius of the 2D fractal aggregate is determined from β as

$$c_{disc} = \beta c = \frac{\pi {R_h}^2}{V} \qquad \text{or} \qquad R_h = \sqrt{\frac{V \beta c}{\pi}} \tag{5.15}$$

where V denotes the volume of the system. The volume fraction c is defined as $c = \dfrac{V_f}{V}$ where V_f is the volume of the fractal aggregate. We have

$$R_h = \sqrt{\frac{V\beta\dfrac{V_f}{V}}{\pi}} = \sqrt{\frac{V_f\beta}{\pi}} \tag{5.16}$$

and the volume of the fractal aggregate can be written as

$$V_f = N_f\pi a^2 = \gamma_{out}\Big(\frac{R_{out}}{a}\Big)^{D_f}\pi a^2 \tag{5.17}$$

where a is the radius of elementary particles of the fractal aggregate. The hydrodynamic radius can be obtained from a numerical fit with Sangani-Acrivos solution. Coefficient β finally does not depend on V but may depend on the fractal dimension D_f.
In 2D, the value R_h also depends on the chosen orientation of the fractal aggregate, but seems to show strong variations for small fractal aggregates where their structures are less isotropic. For the 0-rotated and π-rotated orientations of a 200-particle fractal, we find $\dfrac{R_h}{R_g} = 1.139$ and 1.336, respectively. For larger fractal aggregates having more isotropic structures, we expect their R_h to be less dependent on orientations. Finally, we consider a larger DLA fractal aggregate with 500 particles which is more isotropic than the one in figure 5.7. In figure 5.11, we see that for all the four considered orientations, the $F_D - u$ relation is not much different. It also corresponds rather well with the drag on the cylinder which circumscribes the aggregate. In addition, a cylinder whose radius is equal to the gyration radius of the fractal experiences a drag force significantly smaller.

5.3.3 Effect of the compacity of fractal aggregates on hydrodynamic properties

In this part, we investigate the effect of another factor on the hydrodynamic properties, namely the compacity of fractal aggregates. This factor is quantified by using the sticking probability P_s in the cluster-cluster aggregation process [11]. The quantity P_s gives the probability that particles or clusters form bonds with the growing aggregate. Smaller sticking probabilities produce more compact structures since the particles can penetrate easily inside the aggregates. Consequently, the fractal dimension of an aggregate is higher when P_s is smaller, and the aggregation process is considered as a DLA (Diffusion Limited Aggregation) process.
Here we consider fractal objects of 1000-particles which are formed using sticking probabilities $P_s = 1.0,\ 0.1,\ 0.01$ and 0.001. The effect of P_s on the fractal

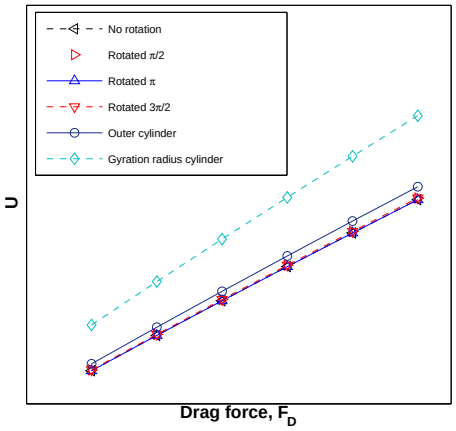

Figure 5.11: Average velocity versus drag force for the 500-particle DLA fractal. The hydrodynamic behaviour for all orientations and the one (solid line) of the circumscribing cylinder are similar. The upper dashed line is that obtained for a cylinder whose radius is the gyration radius of the fractal.

aggregate is investigated by considering the dependence of the ratio $\frac{R_h}{R_g}$ on the sticking probability P_s. As in the previous section, this relationship may depend on the orientation of the fractal aggregate with respect to the main flow. Here, we consider two positions: i.e. the reference position and the $\pi/2$-rotated position to the main flow. The results of $\frac{R_h}{R_g}$ are given in the table 5.1. It is interesting to see that, there is no clear evidence if the ratio of $\frac{R_h}{R_g}$ depends on the sticking probability or not, but does vary with the orientation. Since there is a relation between P_s and the fractal dimension D_f, then the results suggest that there

P_s	R_h/R_g rotated 0	R_h/R_g rotated $\pi/2$
1	1.46	1.57
0.1	1.44	1.59
0.01	1.44	1.51
0.001	1.43	1.58

Table 5.1: $\frac{R_h}{R_g}$ for 1000-particles WS aggregates formed under different sticking probability.

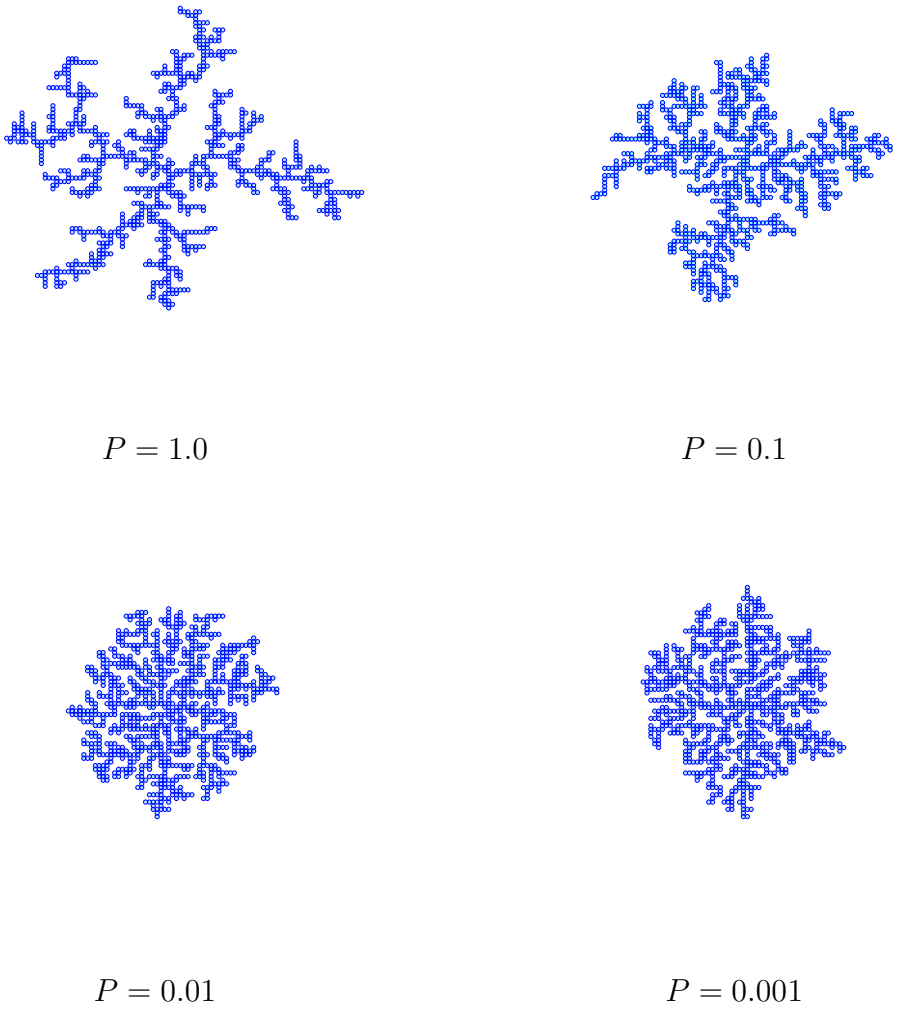

Figure 5.12: 1000-particles fractals formed with different sticking probabilities.

is no evidence that, in 2D, the ratio $\frac{R_h}{R_g}$ of fractal aggregates depends on the fractal dimension. The results also suggest that the hydrodynamics of 2D fractal aggregates depend, not only, on the convex hull but also on the orientation of the fractal aggregates to the main flow. These results may reflect the fact that the role of the third dimension is not visible. In 2D, R_g might not be a relevant factor to connect the outer structure of the aggregates with the hydrodynamics.

5.4 Summary and conclusion

In this chapter, we considered the lattice Boltzmann method to study slow flow past an array of impermeable cylinders in 2D. The analytical solution for this flow has been found by Sangani et al [80] for the case of dilute arrays, in which the role of the volume fraction c is considered. Our lattice Boltzmann simulation results show a very good agreement with this solution. We found that, up to a volume fraction $c < 0.25$, our lattice Boltzmann simulation can produce an agreement with an error of less than 5% compared to the analytical solution for both the bounce-back and the mass conserving boundary alternatives. We also analysed the accuracy of the bounce-back and the mass-conserving boundary alternatives in this expriment and observed that both boundaries agree well with the solution within its range of validity. However it turns out that the bounce-back boundary shows a better convergence and a better accuracy than that of the mass-conserving boundary. At the volume fraction $c = 0.1$, the bounce-back gives an error of less than 1% while the mass-conserving produces an error about $4 - 5\%$. Additionally, the bounce-back, obviously, requires less computational treatments due to the simplicity of the algorithm. The result, again, supports our choice of the bounce-back for our simulations performed with fractal aggregates.

The investigation into the hydrodynamic behaviour of fractal aggregates is then implemented using the lattice Boltzmann simulation of the flow past an array of fractal aggregates. We consider the simulations at very low volume fractions where the effects of the boundary condition and the finite size are small. The measurement of the flow speed versus the drag force is estimated. We find that the hydrodynamic behaviour of fractal aggregates in 2D depends only on the external shape where we believe the convex hull should give the best approximation. This conclusion is supported by the fact that inside the fractal aggregates, the velocity is almost zero.

We also estimate the hydrodynamic radius of the fractal aggregate in 2D, which we define as the radius of a cylinder giving the same hydrodynamic behaviour as the fractal aggregate itself (i.e. the same $\frac{F}{u}$). The definition of the hydrodynamic radius is non-trivial but we are still able to determine it thanks to the success of our scaling procedure. In fact, the definition does not require that the hydrodynamic radius must be defined in an infinite system. However, it does not depend on the size of the system but only on the given fractal aggregate itself.The ratio of $\frac{R_h}{R_g}$ has been calculated for several fractal aggregates and we found no clear evidence that the $\frac{R_h}{R_g}$ depends on the fractal dimension D_f. This ratio also exhibits a dependence on the orientation of the fractal aggregate to the main flow. This may be a reflection of the fact that the role of the third dimension is

missing. We expect that, in the 3D case, when considering the third dimension, the role of the fractal dimension and permeability will become more crucial in establishing the hydrodynamic properties of fractal aggregates.

Chapter 6

Hydrodynamics of fractal aggregates in 3D

6.1 Introduction

The 3D fractal aggregates are simulations of realistic ones and are expected to give answers to the hydrodynamic behaviour of real aggregates. As mentioned in chapter 2, the hydrodynamic properties of a fractal aggregate are investigated by looking at the hydrodynamic radius R_h and its ratio to the gyration radius R_g. This ratio is expected to depend on the fractal dimension D_f. The settling velocity of a fractal aggregate can, in practice, be estimated once the hydrodynamic radius is known. To determine the hydrodynamic properties, as in the 2D case, the idea is simple: put the fractal aggregate into a fluid and observe its behaviour which is expressed into hydrodynamic quantities such as: the velocity, the drag force, the viscosity, etc. with their relationships. 2D simulations have been conducted successfully and have shown that the hydrodynamic properties of the 2D fractal objects are mostly described by the outer shape of the objects. The fractal dimension does not exhibit a role. In the case of 3D fractal aggregates, we may expect the role of the fractal dimension to be more significant. Here, we employ the lattice Boltzmann model in 3D to advance our investigations into the hydrodynamic properties of 3D fractal aggregates. The fractal aggregates consist of DLA and CCA types, which are obtained from simulations using Witten Sander (WS) and Cluster-Cluster Aggregation models. As experienced in the 2D case, the finite size and the boundary conditions always influence the simulations. In 3D simulations, these effects apparently do not disappear. Therefore, in order to correctly measure the hydrodynamic quantities (such as the hydrodynamic radius), some special treatments are required. Therefore, a lattice Boltzmann model for the flow past an array of fractal aggregates in 3D is developed. We then introduce a semi-analytic method to calculate numerically the hydrodynamic radius of the fractal aggregate. This method actually employs the analytical solution of

Hasimoto and Sangani et al with a scaling procedure.
This chapter is organised as follows. Firstly, we revisit the problem of the flow past an array of impermeable spheres. The analytical solution for this problem is summarised for the case of a cubic array. Then we reproduce the problem using our lattice Boltzmann simulations and we estimate the errors of discretization and implementation in the simulations by comparing the simulation results with the analytical solution. For simulations using fractal aggregates, a scaling method is introduced to calculate the hydrodynamic radius of the fractal aggregates. This method is based on the analytical solution. Beside the hydrodynamic radius, we discover a new quantity namely R_β, which defines the boundary where, inside it, the flow is at rest. A range of simulations using various fractal aggregates is made. From the simulation results, a conclusion of the R_h/R_g relationship is made. We then further broaden our investigations into the artificial fractal objects which are generated using a simple mechanism. A new factor, *connectivity*, controlling the hydrodynamics of fractal aggregates is emerged from our results.Finally, we summarise our investigations with final conclusions on the hydrodynamic properties of fractal aggregates.

6.2 Slow flow past a cubic array of spheres

Unlike the disc in 2D case, the hydrodynamic behaviour of a sphere in a fluid can be determined, either theoretically or experimentally. When an impermeable sphere settles in a quiescent fluid (e.g. water), the governing equations lead to the traditional Stokes' law.

$$\mathbf{F} = -6\pi\mu R\mathbf{u} \tag{6.1}$$

Stokes' law calculates the frictional force $\mathbf{F}$ of a fluid having a viscosity μ acting on a sphere radius R and moving with a velocity $\mathbf{u}$. It is usually the central point in mathematical modelling for determining the hydrodynamics of other objects. Mentioned in chapter 2, some settling velocity models of fractal aggregates are often considered as derivations of the Stokes law. Nevertheless, building a numerical simulation to reproduce the settling of a single sphere in fluid is not an easy task since the simulation will experience boundary effects. Additionally, an analytical solution for the flow past an array of spheres has been determined. Therefore, like in 2D case, we use this solution as a reference to validate our numerical simulations. The analytical solution has been developed by Hasimoto [82] and extended later by Sangani and Acrivos [83]. Here, we give only the essentials of this solution but do not go into technical details. Further details can be found in [82, 83].

6.2.1 The analytical solution of flow past a cubic array of spheres

We consider a steady motion of viscous and incompressible fluid past an infinite array of small spheres. As in the 2D case, the flow has an average velocity u, passing spheres of radius a and exerting a total drag force F on the spheres. Traditionally, the continuity and the Stokes equation are the governing equations of the phenomena. By using the Taylor expansion, the velocity profile of the flow is extended in terms of periodic fundamental solution to the Stokes equation and its derivatives. By using some techniques for evaluating the solution satisfying the boundary conditions, an approximation of drag F, can be obtained. In the case of a dilute array (small spheres), when the volume fraction c of the spheres (defined by the ratio of the volume of a sphere over the volume of the unit cell) satisfies the condition $c << 1$, a numerical approximation of F led to a solution as

$$K^{-1} = 1 - 1.7601c^{1/3} + c - 1.5593c^2 + O(c^{8/3}) \tag{6.2}$$

where K is defined as

$$K = \frac{F}{6\pi\mu u a}. \tag{6.3}$$

The solution explains the effect induced by the presence of other spheres to a given one in the array, which is expressed in terms of the volume fraction c. Obviously, the solution converges to Stokes law in the case of infinite domain $c \to 0$. Nonetheless, when c approaches to a value approximately 0.2, K becomes negative.

To extend the solution to work for a complete range of volume fraction c, Sangani et al have improved the solution K in (6.3) by calculating additional terms. The expression for the velocity, in Hasimoto's work, is actually incomplete, so that some extra terms can be introduced to get the coefficients in equation (6.3) up to $0(c^{10/3})$. By using the periodic and boundary conditions, Sangani et al achieved the complete representation of velocity. Thus, unknown terms in the expression of K (6.3) were found using the same technique of Hasimoto. The enhanced K for the cubic array then read

$$K^{-1} = 1 - 1.7601c^{1/3} + c - 1.5593c^2 + 3.9799c^{8/3} - 3.0734c^{10/3} + O(c^{11/3}) \tag{6.4}$$

This expression appears to converge for a much larger range of volume fractions $0 < c/c_{max} < 0.85$ where c_{max} is the maximum volume fraction of spheres which corresponds to the situation when the spheres are touching each other and is equal to $\pi/6$. The range of the volume fraction is clearly larger than one in 2D, for flow past an array of square cylinders. Furthermore, a solution of the drag in case of $0.85 < c/c_{max} < 1$ can also be obtained, according to Sangani et al. However for our interests, the expression (6.4) is adequate.

6.2.2 Simulation of flow past a cubic array of spheres

We reproduce our lattice Boltzmann simulation for flow past a cubic array of spheres for two reasons: first, it is a validation of our fluid model as well as a cross-check with an analytical solution. Then, limits of simulation and errors of the model can be estimated so that we know quantitatively how to restrict the simulation parameters.
Our simulation of flow past an array of spheres has been developed using the model D_3Q_{19}. This model has successfully simulated Poiseuille flow in 3D (in chapter 4) and shown to be a good balance between numerical stability, accuracy and the cost of simulation. The domain of simulation is a cubic box having periodic boundary conditions along all three spatial dimensions. A sphere with radius a is centered in the box. Due to the periodic boundaries along all the dimensions, the simulation becomes that of flow past a cubic array of spheres. The surface of the sphere is governed by the bounce-back rule. The fluid is accelerated using a body force, $\mathbf{F_b} = (G, 0, 0)$, which initiates a flow to x direction. Again, as seen in the 2D case, the measurements of total force and flow velocity are implemented in the stationary regime. In the stationary regime, the total momentum injected in the fluid by the body force is exactly equal to the drag force F_D, acting on the sphere. This drag force is estimated similarly as in the equation (5.7)

$$F_D = \sum_{\mathbf{r_s}} \sum_{i}^{z} 2 f_i(\mathbf{r_s}) v_i \tag{6.5}$$

where $\mathbf{r_s}$ designates the lattice sites belonging to the surface of sphere. Since the sphere immersed in the fluid, it also experiences a buoyancy force F_{BC} due to the imposition of the body force. This phenomena is also seen in the 2D case with cylinders. Again, the buoyancy force is calculated as

$$F_{BC} = V_s F_b = \sum_{\mathbf{r_s}} F_b, \tag{6.6}$$

V_s is the volume of the sphere and $\mathbf{r_s}$ labels all the lattice sites representing the sphere. Thus, the total force acting on the sphere is

$$F = F_D + F_{BC} = \sum_{\mathbf{r_s}} \sum_{i}^{z} 2 f_i(\mathbf{r_s}) v_i + \sum_{\mathbf{r_s}} F_b \tag{6.7}$$

The average velocity of flow is defined as the average velocity on any perpendicular plane yz to the flow direction and we chose to measure it by averaging the velocity of all fluid particles at the outlet of the flow. The viscosity μ is estimated in the same manner, so as to obtain statistically good value.

Discretization of the sphere

We make our first simulation of the flow past an array of spheres using the lattice Boltzmann method. Our goal is to find out how the discretization of sphere behaves in our lattice Boltzmann simulations. First we choose to make our simulations at very low volume fraction e.g. $c = 0.05$, so that the error, due to the volume fraction in the analytical solution of Hasimoto-Sangani, can be negligible (less than 0.5%). Then the total error is assessed, mainly from the lattice Boltzmann simulation i.e. the dicretization and boundary conditions. The Reynolds number of the simulation is restricted to a rather low value (e.g. $Re \sim 0.2$). We want to obtain quantitatively the discretization effect of the sphere surface on the total error of simulation. Next, we make simulations with different sizes of spheres and simulation domains, while maintaining the volume fraction at $c = 0.05$. The radius of the sphere varies from 3.5 lattice spacing to 20 lattice spacing.
The error is estimated by the difference between the numerical simulation and the analytical solution, defined as

$$e = \Big| \frac{1}{1 - 1.7601c^{1/3} + c - 1.5593c^2 + 3.9799c^{8/3} - 3.0734c^{10/3}} - \frac{F}{6\pi\mu Ru} \Big| \quad (6.8)$$

where F, u, μ are measured from the simulations. The figure 6.1 shows the error

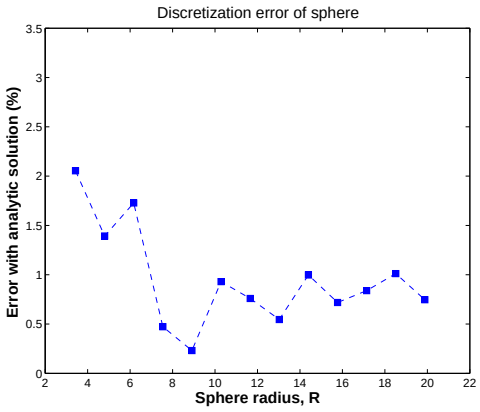

Figure 6.1: Discretization error of sphere.

between our simulations and the Hasimoto-Sangani solution. Results obtained reveal that the discretization error of the sphere is not very significant as it quickly converges with an increment of sphere size (radius). This fact can be explained as the fluid tends to smooth out the roughness of sphere surface. One can see that, with a radius of sphere larger than 8 lattice spacing, the error drops approximately to 1%.

Volume fraction effect

Having obtained the discretization effect of sphere, we now investigate the limit of the volume fraction of the sphere, below which our simulations still agree with the analytical solution of Hasimoto-Sangani. This time, we fix our sphere at a size large enough that discretization error is negligible, i.e. the radius of sphere is fixed at $r = 20$ lattice spacing, much larger than the limit $r = 8$ we learned from the previous simulation. We try various simulations for different volume fractions by changing the size of the simulation domain. Body force is imposed again to accelerate the fluid, while the Reynolds number is kept at about 0.1 or lower. The magnitude of the body force, in our 3D simulations, often remains at $10^{-7} \div 10^{-8}$ and the resulting velocity is of the order 10^{-5}. The spread of volume fraction is set to range from 0.03 to 0.4. Our simulation results appear to excellently agree with the Hasimoto-Sangani analytical solution in the dilute case. Figure 6.2 illustrates our results and error, compared with the analytical solution. The error is calculated as equation (6.8) and is shown on the right of

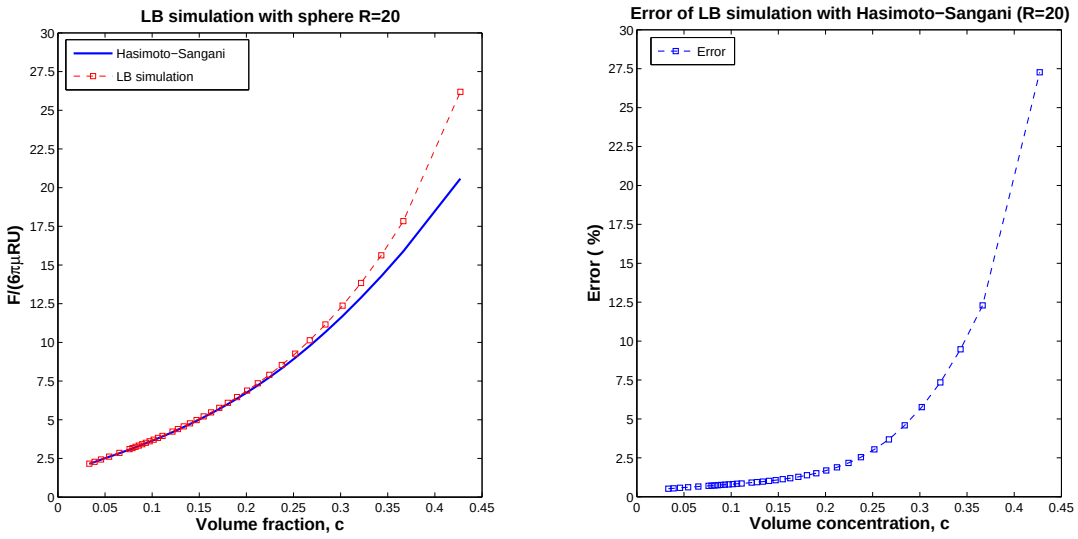

Figure 6.2: The lattice Boltzmann simulation compares to the Hasimoto-Sangani solution.

figure 6.2. At a volume fraction of about $c = 0.3$, the simulation deviates by about 5% from the analytical solution. This deviation is in fact due to the violation of the dilute condition $c << 1$. Eventually, we use this limit in our simulations with fractal aggregates to avoid the error. Practically, in latter simulations with fractal aggregates, the volume fraction is often limited to less than 0.1. This is not difficult when the volume of fractal aggregates is small compared to the total volume of the system.

6.3 A rescaling method to compute the hydrodynamic radius of fractal aggregates

Ideally, the hydrodynamic investigation of fractal aggregates should be made in an infinite or very large domain, where there are no effects of the boundary impact on the results. However, this is impossible, especially in 3D simulations as it will be beyond acceptable CPU and memory limits, even on massive parallel computers. To tackle the problem, like 2D case, we propose to use the following new approach.
We consider a simulation of flow past a cubic array of fractal aggregates. As in the case of the sphere, the simulation domain is a cubic box and made of periodic boundary conditions along the three spatial dimensions. The mass centre of fractal aggregates coincides with the centre of the simulation domain. The fractal aggregates, in the simulation, are composed of point-like elementary particles. Each elementary particle occupies one lattice site. The body force $F_b = (G, 0, 0)$ is imposed on each fluid particle again, to accelerate the fluid to direction x. As before, we consider the hydrodynamics of simulation in a stationary regime when the total momentum injected in the system is fully absorbed on the surface of the fractal aggregate. Thus, it equilibrates to the drag force F_D, measured on the fractal aggregate. We also use equation (6.5) to compute it in this simulation, where the sum is taken over the surface of the fractal aggregate. The fractal aggregate also experiences a buoyancy force F_{BC}, that is computed like equation (6.6); however, the volume V_s is replaced by the volume V_f of the fractal aggregate. We estimate the total force using equation (6.7) for the fractal aggregate. Average velocity u can be measured by averaging all the fluid particles on any yz plane and is chosen to be measured at the outlet plane of flow. The viscosity is also measured in the same manner, in order to reduce the compressibility error and obtain a statistically better value. Figure 6.3 shows the cross-sectional planes along x, y, z-axes of velocity intensity of flow in a simulation with a Witten Sander fractal aggregate of 10000-particles, $D_f = 2.49$.

For a fractal aggregate with an outer radius R_{out} (defined in equation (2.6)), the Hasimoto-Sangani relation (6.4) between volume fraction $c = V_{fractal}/V_{domain}$ and the quantity $K = F/(6\pi\mu u R_{out})$ is no longer obeyed. Figure 6.4 shows the value of K measured in the lattice Boltzmann simulation from F and u with different volume fraction c. We see that the numerical measurement does not correspond to the plot of equation (6.4). However, a very interesting property of the data holds. There exists a scaling $K \to \alpha K$ and $c \to \beta c$ so that the re-normalised data collapse perfectly on the Hasimoto-Sangani curve. The unknown coefficients α and β are obtained from the parameter fit procedure following.

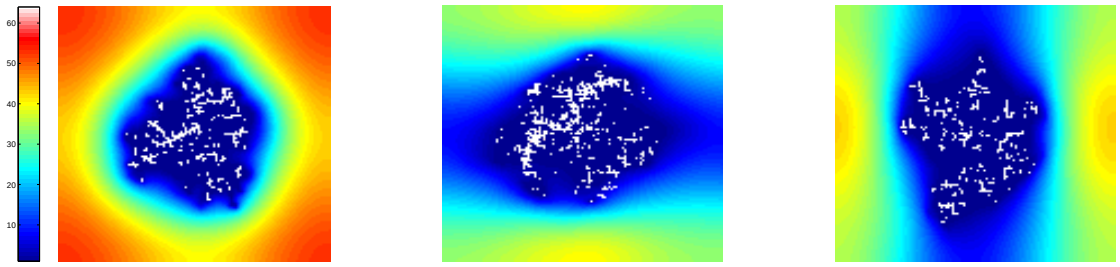

(a) (b) (c)

Figure 6.3: Cross-sectional planes along x, y, z axes of flow in a simulation with WS fractal aggregate of 10000-particles, $D_f = 2.49$. (a) yz plane, (b) xz plane, (c) xy plane.

$$\frac{F}{6\pi\mu u R_{out}} \to \alpha \frac{F}{6\pi\mu u R_{out}} = \frac{F}{6\pi\mu u \dfrac{R_{out}}{\alpha}} \tag{6.9}$$

$$c \to \beta c \tag{6.10}$$

Let $\mathbf{K}$ be the vector data obtained from the lattice Boltzmann simulation and $\mathbf{HS}$ is the Hasimoto-Sangani function (equation (6.4)). The rescaling procedure is to find α and β so that $\alpha\mathbf{K}$ collapses on $\mathbf{HS}(\beta c)$. Numerically, the problem can be formulated as a least-square minimisation:

$$\min f = \sum \left| \alpha\mathbf{K} - \mathbf{HS}(\beta c) \right|^2 \tag{6.11}$$

where α and β satisfy the conditions

$$\frac{\partial f}{\partial \alpha} = 0 \tag{6.12}$$

$$\frac{\partial f}{\partial \beta} = 0. \tag{6.13}$$

This problem is then solved using the simplex search method. Figure 6.5 now shows how the rescaled data well obey equation (6.4).
Two main results emerge from this rescaling of the data on the Hasimoto-Sangani solution for a sphere. Firstly, rescaling K actually amounts to rescaling the radius R_{out} by $1/\alpha$. Thus, as far as the drag force is concerned, the fractal aggregate behaves as a sphere of radius R_{out}/α, which is precisely the property of the hydrodynamic radius. Consequently we define

$$R_h = R_{out}/\alpha \tag{6.14}$$

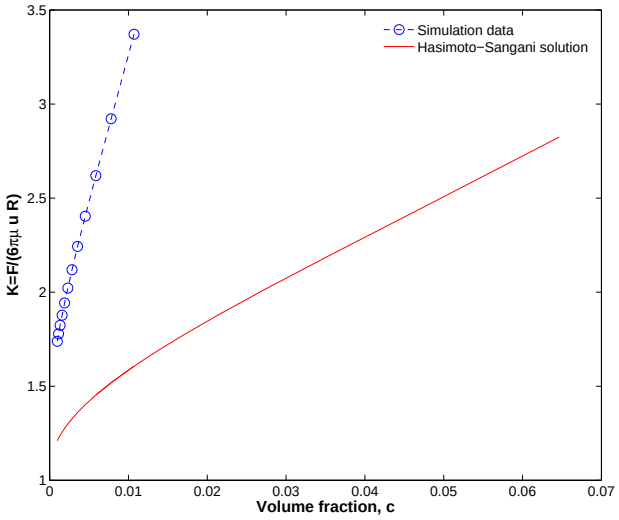

Figure 6.4: LB simulation data for a fractal aggregate (N=500, $D_f = 2.49$). The solid line is the Hasimoto-Sangani solution and the ∘ is the simulation data.

Secondly, from the β scaling of the volume fraction we learn that the fractal aggregate has an effective volume

$$V_{eff} = \beta V_f \tag{6.15}$$

Note that this effective volume is significantly larger than the actual volume of the aggregate. Assuming that a spherical shape, V_{eff} corresponds to a new radius R_β such that

$$V_{eff} = (4/3)\pi R_\beta^3 \tag{6.16}$$

It turns out that this new radius, R_β, is smaller than R_h. From the derivation of the Hasimoto-Sangani relation, it is clear that the quantity c reflects the fact that, inside the volume V_{eff} the fluid speed is zero (see figure 6.6(a)). Thus, following the same interpretation, we conjecture that R_β is the radius below which the flow inside the aggregate is vanishing. This interpretation is confirmed by the study of the simulated flow pattern in the fractal object, as displayed in figure 6.6.
Recall that the hydrodynamic radius of the fractal aggregate is that of the sphere experiences the same drag force under the same velocity flow in an infinite domain without boundary effect. Hence, in a given array of fractal aggregates, if we replace the fractal aggregate by the hydrodynamic sphere, we may not obtain the same hydrodynamics. The fact is that, with the same array (i.e. the same distance to periodic images), the hydrodynamic interactions with periodic images of the sphere may not be the same as one of the fractal aggregate. However, in another array, e.g. if the distance between objects is larger, the hydrodynamics can

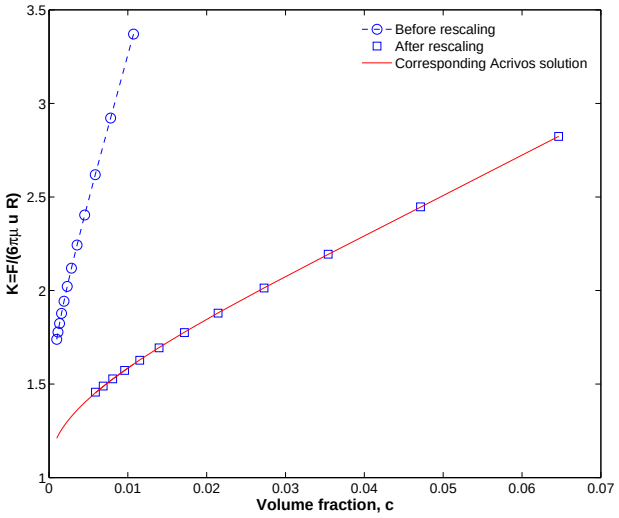

Figure 6.5: After an appropriate α and β rescaling along each axis, the numerical result agrees well with the Hasimoto-Sangani relationship.

again be found, when an appropriate distance between objects can compensates for the difference in interaction. This is illustrated in figure 6.7. Numerically, the method appears to fit rather well with the Hasimoto-Sangani solution. We observed the SSE [1] of numerical fit with the analytical solution is of the order of 10^{-6} on average and R-square is of 0.99. Using this method we can now compute R_h as well as R_β for our full set of fractal objects.

6.4 Results on hydrodynamics of 3D fractal aggregates

6.4.1 Hydrodynamic structure of fractal aggregates

The first result for the hydrodynamics of fractal aggregates comes from the emergence of R_β. By studying the velocity distribution of the fluid, R_β indicates the position where the velocity becomes important. Thus, it suggests that the fluid cannot actually penetrate deeply into the fractal aggregate through the whole structure below R_β but just flow through the outer region. Hydrodynamically, fractal aggregate structures can be modelled as an internal solid core with an external porous shell, as illustrated in figure 6.8

[1] Sum of Squared Error $= \sum_{i=1}^{n} (y_i(fit) - y_i(Sangani))^2$

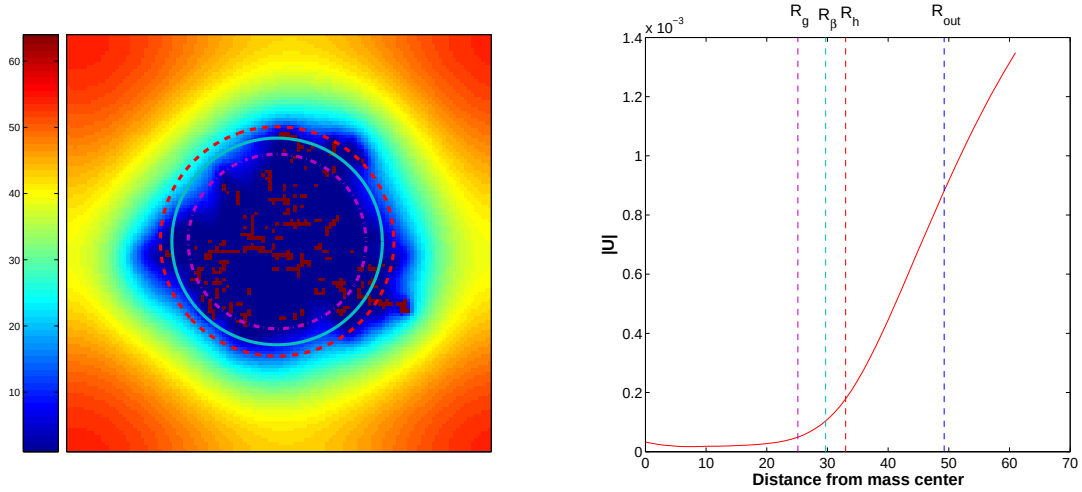

(a) (b)

Figure 6.6: (a)Velocity intensity on a cross-sectional yz plane through the mass centre of the aggregate. The yellow ring illustrates the gyration radius. The cyan ring shows the R_β and the red ring demonstrates the R_h. (b)The measured modulus of the flow speed as a function of the radius r measured from the centre of mass. We observe that above the value $r = R_\beta$, the speed increases significantly whereas, below R_β the fluid speed is negligible. Simulation is with a WS fractal aggregate of 10000 particles and $D_f = 2.49$.

6.4.2 The relation of $\frac{R_h}{R_g}$ to aggregate size N

We compute the R_h and R_β for several sets of two types of fractal aggregates, those obtained from the Witten and Sander (WS) model and those using the Cluster-Cluster Aggregation (CCA) process (see chapter 2). For each set of fractal aggregates, we have a range of different sizes $100 \leq N \leq 20000$ and five instances for each size. Due to the sensitivity of drag force to a given fractal aggregate, measurements are performed on those five aggregates to extract an averaging result. In total for each set of fractal aggregates, this makes up several hundreds of 3D simulations. It takes several months in computation time on parallel computers for each set of fractal aggregates.
The first result is that, asymptotically, R_h depends on N with the fractal dimension D_f in the same manner as R_g

$$N = {\gamma_h}^* (R_h)^{D_f} \tag{6.17}$$

where ${\gamma_h}^*$ is a coefficient which may depend on D_f. The result is illustrated in figure 6.9. The relation should suggest that $\frac{R_h}{R_g}$ is independent of aggregate size

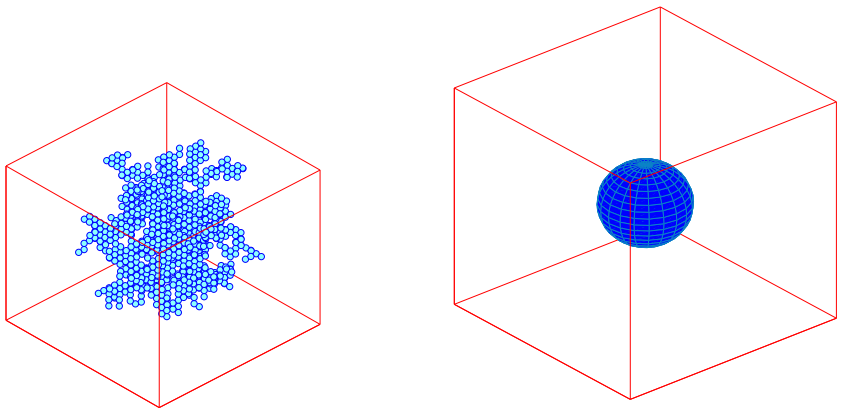

Figure 6.7: Equivalent hydrodynamics of fractal aggregates and a hydrodynamic sphere can be found in different simulation domain sizes. The difference in domain size is necessary to compensate for the difference in hydrodynamic interaction with their periodic images. In the infinite domain without the effect of boundary, the fractal aggregate and the sphere give the same hydrodynamics.

N, but only on D_f. Table 6.1 gives the simulation results for several types of fractal aggregate. Due to the fact that there are large variations in the structure of fractal aggregates, the results should be taken over a large population of the same type, i.e. R_g should be measured by averaging the ensemble of fractal aggregates. Nevertheless, we also observed fluctuations in our experiments and the final results have been obtained by using an appropriate statistical treatment. Detailed results for various fractal aggregates can be found in the appendix C.

Fractals	D_f	$\frac{Rh}{Rg}$
CCA	1.9855	0.981
WS	2.493	1.245
WS	3	1.29

Table 6.1: Ratio $\frac{R_h}{R_g}$ for several D_f.

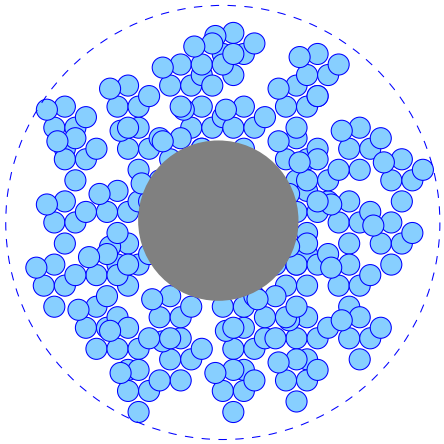

Figure 6.8: Modelling of fractal aggregate structure. The structure can be modelled with an internal solid core (black) and external porous shell.

6.4.3 The prefactor and the connectivity of fractal aggregates

By convention, equation (6.17) is expressed as

$$N = {\gamma_h}^* {R_h}^{D_f} = (\frac{\gamma_h}{a^{D_f}}){R_h}^{D_f} \tag{6.18}$$

where a is the radius of elementary particles making up the aggregate. Recall the equation (2.12), then we have

$$N = (\frac{\gamma_g}{a^{D_f}}){R_g}^{D_f} = (\frac{\gamma_h}{a^{D_f}}){R_h}^{D_f} = (\frac{\gamma}{a^{D_f}})R^{D_f} \tag{6.19}$$

where R is the outer radius and γ is the corresponding prefactor. Thus, we have

$$\frac{R_h}{R_g} = \left(\frac{\gamma_g}{\gamma_h}\right)^{1/D_f}. \tag{6.20}$$

Now, in our investigation of the hydrodynamic properties of fractal aggregates, the first question we want to answer that is *"Is D_f the only factor to control $\frac{R_h}{R_g}$?"*. In other words, does $\frac{R_h}{R_g}$ depend only on D_f?. It would mean that the ratio of prefactor $\frac{\gamma_h}{\gamma_g}$ is always the same for all fractal objects having the same fractal dimension. We will show in the following part that it is not true by generating fractal objects with the same D_f but a different γ_g and measuring the variation of R_h/R_g.

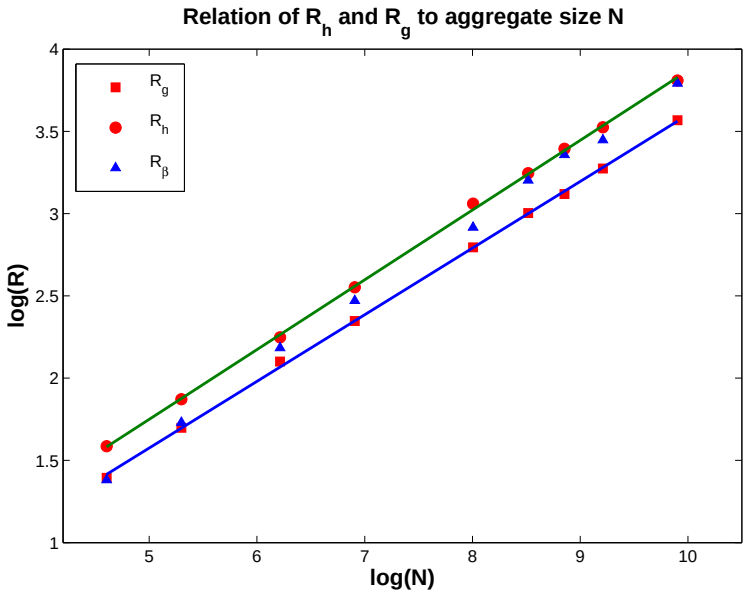

Figure 6.9: Relation of R_h to N and D_f is similar to R_g. The results obtained from the set of Witten Sander aggregates with $D_f = 2.49$.

As we know, common mechanisms to produce fractals are the particle-cluster aggregation (Witten and Sanders model) or cluster-cluster aggregation (CCA). By adjusting the aggregation probability, one can adjust, within some ranges, the resulting fractal dimension. The value of the prefactor γ is not controlled but is imposed by the building mechanism. Table 6.2 gives some values of D_f and γ_g obtained by fitting equation (6.19) on several computer generated aggregates of various sizes N.
In order to study how the hydrodynamic radius depends on γ, we need to independently adjust the values of D_f and γ. For this reason, we build artificial fractal objects which obey equation (6.19) with chosen D_f and γ. The process is the following:
We divide the fractal in many concentric spherical layers of radius r and thickness dr as illustrated in figure 6.10. In each of these layers, we randomly place $\Delta N(r)$ particles, assuming that the possible locations belong to an underlying mesh of spacing a. $\Delta N(r)$ is computed as

$$\Delta N(r) = \frac{\gamma}{a^{D_f}} \left[(r + dr)^{D_f} - r^{D_f} \right] \tag{6.21}$$

which then ensures that equation (6.19) holds for the given value of γ and D_f. In case an already occupied location is selected by the random process to place the next particle, a new location is chosen until a free site is obtained. Objects generated according to this process are illustrated in fig 6.11. It is worth noting

Fractals	D_f	γ_g
CCA 1	1.9855	0.80912
CCA 0.01	2.0647	0.80727
WS 1	2.493	0.54436
WS 0.8	2.515	0.50617
WS 0.4	2.5769	0.5074
WS 0.1	2.8135	0.39935
WS 0.01	3	0.233

Table 6.2: Numerically determined values of D_f and γ_g for Witten and Sanders (WS) and CCA fractal aggregates. The number following the WS or CCA acronym is the aggregation sticking probability.

that this mechanism does not ensure that each particle is connected to another one.

An interesting result is that, for $D_f = 3$ and some given γ, one does not recover the hydrodynamic radius of a compact sphere, for which $R_h/R_g = 1.291$. This is not so surprising since we generated homogeneously porous spheres. However, it is a first indication that fractal dimension is not enough to characterise R_h. With $\gamma = 0.125$, the ratio R_h/R_g varies between 1.23 and 1.25, for $N = 1968$ and $N = 9941$ particles respectively (see table C.8). It should be noted that for our artificial fractals, the size N affects R_h/R_g as opposed to what we had observed for fractal aggregates.

Another example of the role of γ is seen by choosing the $D_f = 1.98$, corresponding to that of CCA aggregates with an aggregation probability of 1, and the $\gamma = 2$ instead of 0.809 (for CCA). The resulting artificial fractal exhibits $R_h/R_g = 1.29$ instead of 0.99 for the CCA.

If now we consider an artificial fractal having the same D_f and the same γ as, for instance, a WS aggregate with $D_f = 2.49$ and $\gamma = 0.544$, we do not obtain the same R_h/R_g. The primary reason for that is the fact that R_h/R_g depends on N with the artificial fractal.

The conclusion is that D_f and γ are not enough to fully describe the hydrodynamic behaviour of a fractal object. This suggests that there is an extra hidden quantity that must be taken into account.

A closer look at the structure of our artificial fractal reveals that elementary inter-particle *connectivity* varies radially. Here, the connectivity is defined as the average number of neighbours a given particle is connected to, considering the topology induced by the 3D Cartesian grid. At most, a particle can have 18 particles as immediate neighbours. This connectivity in fact has a link with the permeability, discussed in chapter 7. Figure 6.12 shows that the connectivity behaves quite differently for a WS aggregate than it does for an artificial fractal

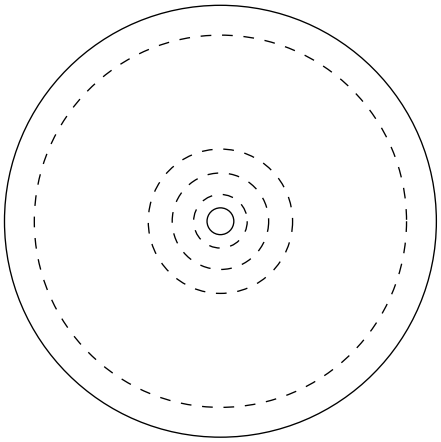

Figure 6.10: Illustration of concentric-layer building mechanism of artificial fractal aggregates.

having the same D_f and γ.
Note that it is very difficult to obtain artificial fractals having the same properties like fractal aggregates, i.e. the same D_f, the same γ and the same connectivity (at a given size that gives similar connectivity). Then, one has to choose to generate the artificial fractals at a given size to obtain the same average connectivity. Here we generate two artificial fractals having the same properties as WS aggregates with $D_f = 2.49$ and CCA aggregates with $D_f = 1.98$. Our results are presented in table 6.3 where we compare the ratio R_g/R_g for fractal aggregates and corresponding artificial fractals. Now, we find some similar values. These

Fractals	Aggregate	Artificial object	Aggregate	Artificial object
D_f	1.98	1.98	2.49	2.49
γ_g	0.809	0.809	0.544	0.544
Mean connectivity	5.47	5.27	6.07	6
$\frac{R_h}{R_g}$	0.99	1.09	1.238	1.25

Table 6.3: Comparison of R_h/R_g for artificial fractals and aggregates with the same fractal dimension and internal connectivity.

suggest that, in addition to D_f, the connectivity is actually a key quantity to characterise the hydrodynamic behaviour. The fact that R_h/R_g is independent of N in fractal aggregates can now be related to the fact that, in these types of fractal objects, the connectivity is almost constant as N increases.

$D_f = 2$ $D_f = 3$

Figure 6.11: Artificial fractals with $\gamma = 8$, $D_f = 2$ (left), and $\gamma = 0.2$, $D_f = 3$ (right). With appropriate values of γ, objects obtained for $D_f = 3$ become very porous in comparison to ones of $D_f = 2$.

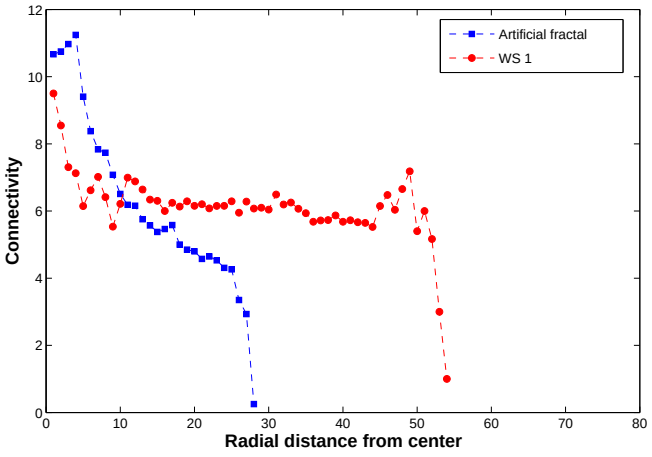

Figure 6.12: Connectivity as a function of radial distance for a WS fractal aggregate (P=1) of N=10000 particles and an artificial fractal with similar size N, the same D_f and prefactor γ. One can observe that while the connectivity of the fractal aggregate is almost constant, that of the artificial fractal decreases quickly as the distance increases

6.5 Summary and conclusion on the hydrodynamics of fractal aggregates

In this chapter we have made our investigation into the hydrodynamic properties of fractal aggregates using numerical simulations. To the best of our knowledge, this is the first investigation using accurate 3D simulations in determining hydrodynamic properties of fractal aggregates.

We have shown that, in the experiment of flow past an array of spheres, our fluid model agrees excellently with the analytical solution of Hasimoto-Sangani. We then proposed a method to calculate numerically the hydrodynamic radius and have successfully computed it for various fractal aggregates. This method consists of a rescaling procedure for numerical simulation data using the Hasimoto-Sangani solution.

Our first conclusion on the hydrodynamic properties of fractal aggregate is that, for a given type of fractal aggregates having the same D_f, the $\frac{R_h}{R_g}$ does not depend on the aggregate size (or mass) but only on the fractal dimension D_f. The relation of R_h to the aggregate size N has a similar form as that of R_g.

We also discovered a new hydrodynamic quantity namely R_β which gives quantitatively the boundary inside which the flow is at rest. Therefore, a fractal aggregate can be modelled as an object having a solid core and an external porous shell.

In addition, the prefactor γ is found to play a role in the hydrodynamic behaviour of fractal aggregates; however, this factor is implicitly imposed by the aggregation mechanism. For fractal aggregates, we obtain an unique value of γ for a given D_f. Further investigations with artificial fractals show that, even with the same D_f and the same γ, we cannot recover the same $\frac{R_h}{R_g}$ as that of fractal aggregates. It leads to the revelation of a hidden quantity, namely the connectivity. This quantity is expected to link with the permeability where we also find it to play a key role in the hydrodynamic properties of fractal aggregates. This factor was not mentioned in previous studies for fractal aggregates since, for a given type and a given D_f, it is a constant.

Finally, one can find that the figure 2.8, shown in chapter 2 in an attempt to establish a dependence of $\frac{R_h}{R_g}$ on D_f, now becomes irrelevant, since we have to compare fractal aggregates having the same γ and connectivity.

In summary, the $\frac{R_h}{R_g}$ of a fractal aggregate is quantified not only by fractal dimension D_f but also by the prefactor and the connectivity.

Chapter 7

Permeability of fractal aggregates and governing equations of the internal flow

7.1 Introduction

In chapter 6, we have calculated the hydrodynamic radius of fractal aggregates and its ratio with the gyration radius. The ratio is an important hydrodynamic quantity, but does not give any quantitative information about the flow inside fractal aggregates. Actually, the hydrodynamics of the flow inside fractal aggregates relates to the aggregate permeability.
A common way to determine how a flow behaves inside a fractal aggregate is to model the fractal aggregate as a porous medium. Nonetheless, the permeability of the aggregate cannot be modelled simply as a constant. Indeed, the medium is heterogeneous with more than one typical pore size. To model the phenomenon of the flow past a fractal aggregate, traditionally, the aggregate is divided into 2 regions:
1. The external region: is the region outside the fractal aggregate where the Stokes equation is assumed to govern the flow.
2. The internal region: is the porous part of the fractal aggregate where the fluid can go inside. The governing equation in this region can be either the Brinkman equation or Darcy's Law.
The existence of a radius R_β below which the fluid is at rest in the aggregate suggests another region in which the flow speed is zero. This gives the opportunity to apply a faster way to address the calculation of the hydrodynamic properties of a fractal aggregate immersed in an infinitely large fluid domain with a speed u_∞, far away from the obstacle. In this chapter, we investigate the hydrodynamics of fractal aggregates by studying the permeability of the fractal aggregates and its relation to the internal flow. First, we consider an existing model made by

Veerapaneni et al [30] in which we explicitly derive the solutions for the boundary condition equations. We then apply these solutions to our aggregates to find the hydrodynamic radius so that we can verify our lattice Boltzmann simulation results in another way. We show that, **with the same effective viscosity assumption and assuming the Happel model** holds for the permeability of the fractal aggregates, we obtain again the same hydrodynamic radius as compared to our simulation results. However, from the lattice Boltzmann simulation data, we are able to verify these assumptions.We employ our lattice Boltzmann simulation data to estimate numerically the radial permeability of the fractal aggregates and verify again the governing equation of the flow inside. The results obtained suggest that, Darcy's Law is actually the governing rule instead of the Brinkman equation.

7.2 The radially varying permeability model

The radially varying permeability model has emerged in several works [84, 85] in the case of flow through a porous sphere. Then, Veerapaneni et al [30] applied it to model the permeability of fractal aggregates. It is known that the porosity of fractal aggregates increases with size and usually presents a correlation with permeability. Hence, it is relevant to consider that the permeability of fractal aggregates varies radially from the center to outside. In the following we apply this model on our fractal aggregates with the same assumption of Veerapaneni, for the effective viscosity of the fluid to verify our calculation of the hydrodynamic radius.
We consider a fractal aggregate with the assumption that the permeability varies radially from the center to the outside, where the center is commonly chosen as the mass center of the aggregate. With the presence of R_β below which the fluid

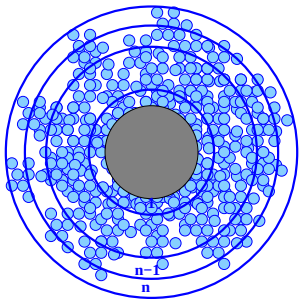

Figure 7.1: The fractal aggregate model for determining the permeability radially.

velocity is zero, it suggests that we can split the fluid-aggregate system into three regions. The first region is defined by a sphere centering at the mass center of the

aggregate and having the radius equal to R_β. This region is impermeable when the flow speed is zero $u = 0$. The second region is defined by a porous shell, enclosing the first region and having the outer boundary at the distance from the center equal to the outer radius R_{out}. A point at a radial distance r will belong to this region if $R_\beta < r \leq R_{out}$. This region of the aggregate behaves as a porous media and the Brinkman equation

$$-\mu_e \nabla^2 u + \frac{\mu}{K} u = \nabla P$$

should hold. The quantity K is the permeability of the fractal aggregate which depends on the local aggregate porosity, and thus the local solid concentration $\rho(r)$; μ_e is called the effective viscosity; ∇P is the pressure gradient which drives the flow; in our lattice Boltzmann simulation, this pressure gradient is induced by a body force F_b and we have

$$F_b = -\nabla P. \tag{7.1}$$

Several models have been proposed to relate K and ρ [30]. Finally, the third region is the region outside the fractal aggregate which extends to infinity. This region is defined at the radial distance (from the center) $r > R_{out}$. In this region, the Stokes equation $\mu \nabla^2 u = \nabla P$ applies (low Reynolds number and stationary flows). Following the method of Veerapaneni et al [30], we consider the problem in spherical coordinates and divide the second region in n concentric shells, thin enough that we can assume a constant porosity, thus a constant solid concentration ρ_i in each of them, $i = 1, ..., n$. In shell i we define

$$\rho_i = \frac{a^3 N_i}{\frac{4\pi}{3}(R_i^3 - R_{i-1}^3)}$$

with $R_0 = R_\beta$, $R_n = R_{out}$ and N_i is the number of elementary particles. The quantity a is the linear size of one elementary particle. Here, we assume that these elementary particles are little cubes that occupy exactly one elementary grid point, as in the case of the lattice Boltzmann simulation. Using the ansatz of the solution proposed in [30], the velocity field can be obtained by solving numerically the system of linear equations (see appendix D). It is worth noting that, in the ansatz, the effective viscosity is assumed to be the same as the fluid viscosity that is $\mu_e = \mu$. However, unlike the derivation in [30], we do not include the region $r < R_\beta$ as we know $u = 0$ to be a good approximation. In addition, we proceed in a semi-analytical way. We take the value of R_β and R_{out} from the numerical simulation and we do not assume any explicit expression for the permeability K_i in the ith layer. Instead, we consider the K_i's as free parameters whose values are optimised so that the theoretical calculation yields the same hydrodynamic radius R_h as the lattice Boltzmann simulation.

The results are shown in figure 7.2. The graph shows the permeability of each n

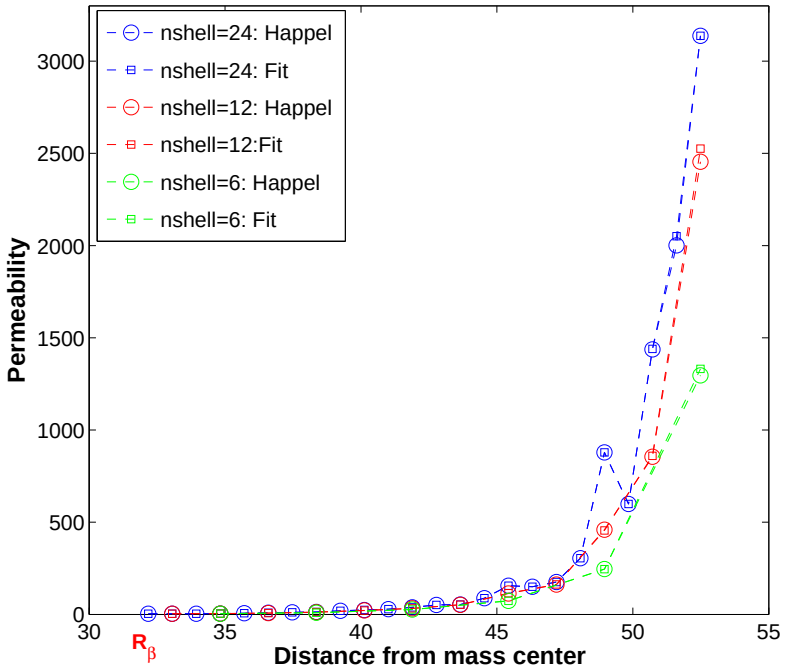

Figure 7.2: The values of the permeability K_i of layers between R_β and R_{out} for a WS aggregate: obtained from a fit of the analytical procedure to the numerical measurements. The dashed line corresponds to the relation $K_i = K_i(\rho_i)$ given by the Happel model.

layers resulting from the optimal fit procedure. For comparison, we plot on the same graph the value of K predicated by the Happel model

$$K = \frac{2a^2}{9\rho}\left(3 - \frac{9\rho^{1/3}}{2} + \frac{9\rho^{5/3}}{2} - 2\rho^2\right) \Big/ \left(3 + 2\rho^{5/3}\right)$$

where ρ is the solid concentration measured in the numerical simulation for each layer. We observe that the Happel model is in good agreement with the ideal permeability emerging from our calculations.
This implies that, using the model of Veerapaneni [30] with the same assumption: the Brinkman equation holds for the flow inside fractal aggregates, the effective viscosity is equal to the normal fluid viscosity $\mu_e = \mu$ and the Happel model controls the aggregate permeability, we then obtain results similar to our lattice Boltzmann simulation. As claimed by Veerapaneni, the Happel model was also used to give predictions of the permeability. The agreement provides a validation of the lattice Boltzmann results considering that: (i) Veerapaneni's assumption is correct and (ii) the Happel model is the right one for determining the perme-

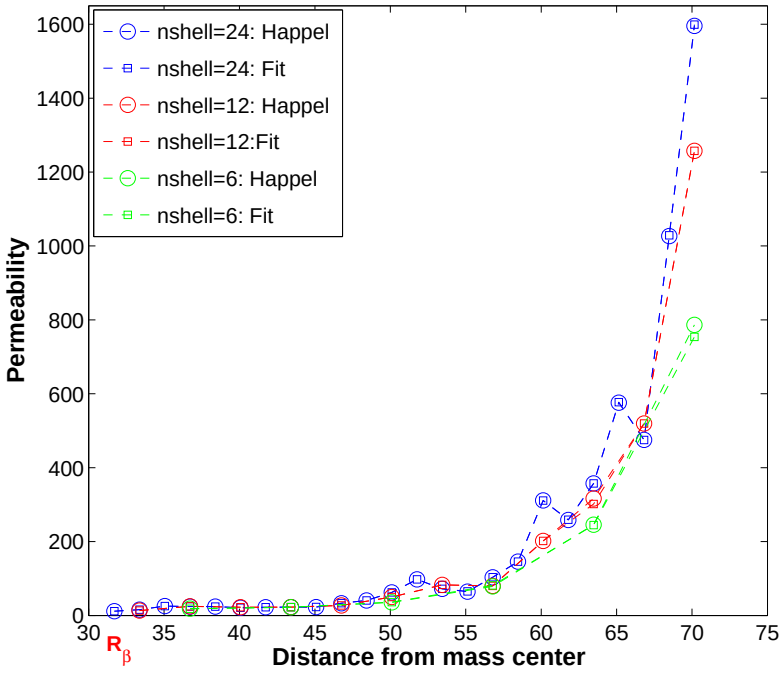

Figure 7.3: The values of the permeability K_i of layers between R_β and R_{out} for a CCA aggregate: obtained from a fit of the analytical procedure to the numerical measurements. The dashed line corresponds to the relation $K_i = K_i(\rho_i)$ given by the Happel model.

ability of aggregates.In our opinion, by imposing the effective viscosity equal to the normal viscosity of the fluid, one has already imposed a constraint on the governing equation of the flow inside. The effective viscosity (and the governing equation) should be determined with freedom. In addition, it is not clear whether the Happel model is the right one for fractal aggregates or not. From simulations, this quantity can be measured numerically. In the following part we shall measure numerically the effective viscosity and the radial permeability from the lattice Boltzmann simulation data.

7.3 Darcy's Law versus the Brinkman equation

In this section, we consider the permeability in another way. We shall measure the radial permeability of the aggregate by fitting our lattice Boltzmann flow velocity measurements $\vec{u}$ with the Brinkman equation. We still assume that the fluid-aggregate system is divided in three regions as before and also that the

Brinkman equation holds inside the porous part of the fractal aggregate. Now, we use our lattice Boltzmann data to fit the equation, thus obtaining effective viscosity μ_e and permeability K.
In order to fit lattice Boltzmann data, one has to estimate u and $\nabla^2 u$ numerically. The body force F (or pressure gradient) and fluid viscosity are known, while we estimate K and μ_e as a function of the radial distance r. As before, the flow is in the direction x. Here, we do not divide the fractal aggregate into spherical shells, as before, but divide it in rings of radius r', perpendicular to the flow direction as illustrated in figure 7.4. There are two reasons for us to proceed

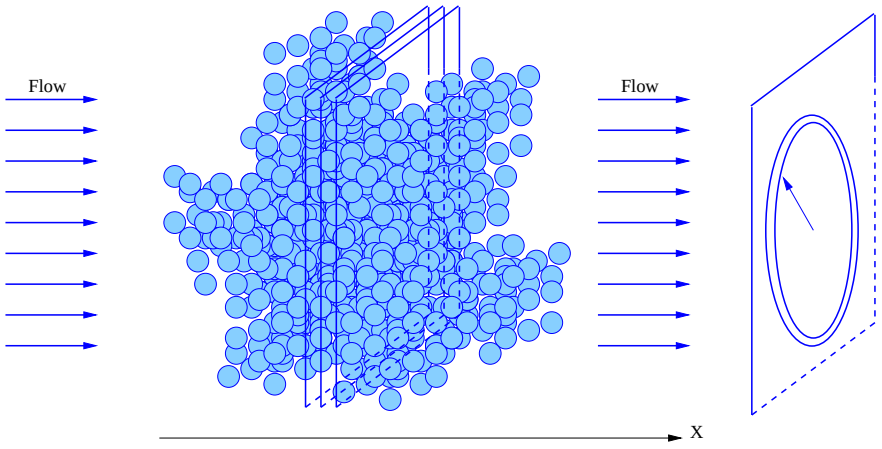

Figure 7.4: Estimation of permeability by fitting the Brinkman equation to the lattice Boltzmann simulation. u is averaged on each ring; then, $\nabla^2 u$ is estimated along flow direction x.

it in this way: First, the permeability of fractal aggregate is considered to vary isotropically in all directions, i.e. the variation along x direction should be similar to y and z directions. Therefore, the variation of permeability perpendicular to the flow direction is enough to represent the variation of the permeability of the fractal aggregate. Second, since the flow is set to x direction, by taking average velocity all over the spherical shell, one could destroy necessary information as the velocity field in the front side of the aggregate is much different with the one in the side behind. By considering the mean velocity on a plane perpendicular to the main flow, one can avoid this problem.
The thickness of these rings is selected large enough so that the average flow $\vec{u}$ obeys the Brinkman equation but thin enough so that the permeability can be assumed to be constant over each ring and ensure that the average of $\vec{u}$ over the ring is meaningful. Both $K(r)$ and $\mu_e(r)$ are assumed to vary slower than u and $\nabla^2 u$. $\nabla^2 u$ is obtained as follows. First we write $\nabla^2 u$ with its components in

Cartesian coordinates:

$$\nabla^2 u = \frac{\partial^2 u}{\partial x^2} + \frac{\partial^2 u}{\partial y^2} + \frac{\partial^2 u}{\partial z^2} \tag{7.2}$$

Consider on yz plane, the shell with radius r

$$r^2 = y^2 + z^2 \tag{7.3}$$

$$\left.\begin{aligned} \frac{\partial r}{\partial y} &= \frac{y}{r} \\ \frac{\partial r}{\partial z} &= \frac{z}{r} \end{aligned}\right\} \quad \left.\begin{aligned} \partial y &= \frac{r}{y}\partial r \\ \partial z &= \frac{r}{z}\partial r \end{aligned}\right\} \quad \begin{aligned} \frac{\partial}{\partial y} &= \frac{y}{r}\frac{\partial}{\partial r} \\ \frac{\partial}{\partial z} &= \frac{z}{r}\frac{\partial}{\partial r} \end{aligned} \tag{7.4}$$

$$\frac{\partial^2 u}{\partial y^2} = \frac{\partial}{\partial y}\Big(\frac{\partial u}{\partial y}\Big) = \frac{y}{r}\frac{\partial}{\partial r}\Big(\frac{y}{r}\frac{\partial u}{\partial r}\Big) \tag{7.5}$$

$$= \frac{y}{r}\Big(\frac{y}{r}\frac{\partial^2 u}{\partial r^2} + \frac{r\dfrac{\partial y}{\partial r} - y}{r^2}\cdot\frac{\partial u}{\partial r}\Big) \tag{7.6}$$

$$= \frac{y}{r}\Big(\frac{y}{r}\frac{\partial^2 u}{\partial r^2} + \frac{r^2 - y^2}{yr^2}\cdot\frac{\partial u}{\partial r}\Big) \tag{7.7}$$

$$= \frac{y^2}{r^2}\cdot\frac{\partial^2 u}{\partial r^2} + \frac{r^2 - y^2}{r^3}\cdot\frac{\partial u}{\partial r} \tag{7.8}$$

Similarly

$$\frac{\partial^2 u}{\partial z^2} = \frac{z^2}{r^2}\cdot\frac{\partial^2 u}{\partial r^2} + \frac{r^2 - z^2}{r^3}\cdot\frac{\partial u}{\partial r} \tag{7.9}$$

and we have

$$\frac{\partial^2 u}{\partial y^2} + \frac{\partial^2 u}{\partial z^2} = \frac{y^2 + z^2}{r^2}\cdot\frac{\partial^2 u}{\partial r^2} + \frac{2r^2 - (y^2 + z^2)}{r^3}\cdot\frac{\partial u}{\partial r} \tag{7.10}$$

Notice that

$$y^2 + z^2 = r^2 \tag{7.11}$$

Therefore, we have

$$\frac{\partial^2 u}{\partial y^2} + \frac{\partial^2 u}{\partial z^2} = \frac{\partial^2 u}{\partial r^2} + \frac{1}{r}\cdot\frac{\partial u}{\partial r} \tag{7.12}$$

The Laplacian of u can, then, be written as

$$\nabla^2 u = \frac{\partial^2 u}{\partial x^2} + \frac{\partial^2 u}{\partial r^2} + \frac{1}{r}\cdot\frac{\partial u}{\partial r} \tag{7.13}$$

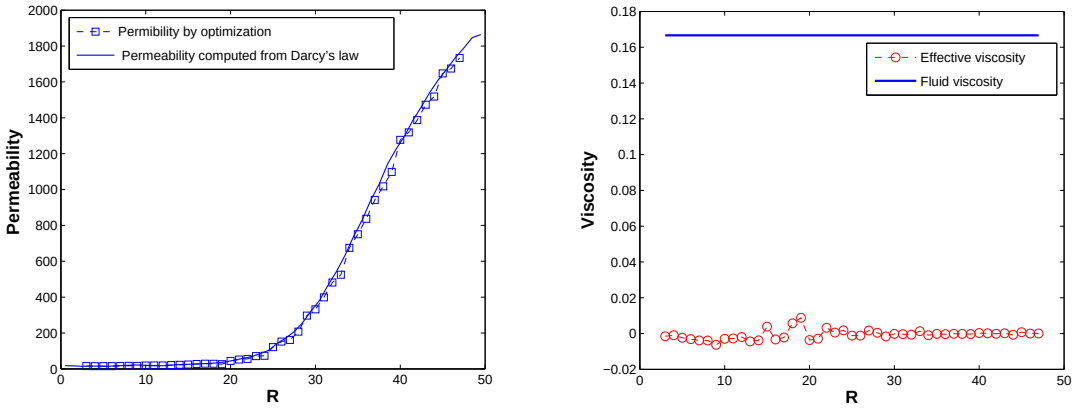

Figure 7.5: Values of the permeability $K(r)$ and effective viscosity $\mu_e(r)$ fitted from LB simulations, assuming that the Brinkman equation holds. The permeability $K(r)$ falls on that calculated using Darcy's Law (on the left).

Equation (7.13) can be easily estimated using the finite difference method, applied for each lattice site. In summary the procedure is as follows:
1. The velocity u is calculated by averaging the fluid velocity in the ring at radius r on the plane yz at x position.
2. $\dfrac{\partial^2 u}{\partial x^2}$ is estimated by taking velocities at the same ring r but on positions $x-1, x, x+1$
3. $\dfrac{\partial^2 u}{\partial r^2}$ and $\dfrac{\partial u}{\partial r}$ is estimated using successive rings $r-1, r, r+1$ on the same plane at x.
Assuming that K and μ_e vary smoothly compared to u and $\nabla^2 u$, we can make an interpolation in the sense of least-square for several successive rings (i.e. in our estimation 4 rings have been used). We, then, obtain a fit, as shown in the figure 7.5. An interesting observation results from these fits: the effective viscosity μ_e is found to be zero, which actually means that the Brinkman equation reduced to Darcy's Law inside the fractal, as opposed to the assumption of [30]. Finally, it turns out that the estimated permeability for fractal aggregates shows different behaviour versus porosity than that predicted by the Happel model (see figure 7.6).

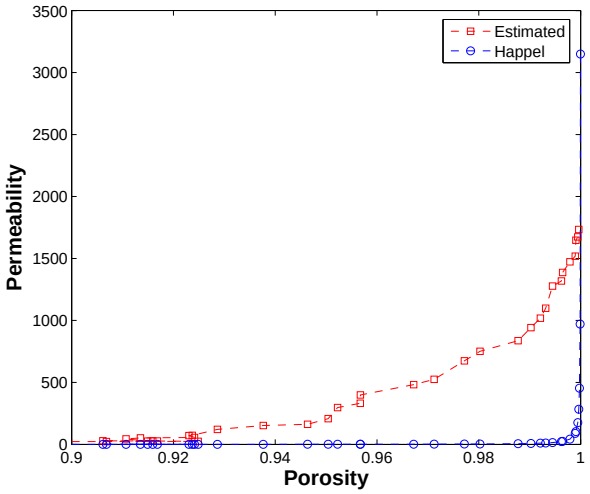

Figure 7.6: Comparison of the permeability derived from our numerical simulations of Witten Sander aggregate with $D_f = 2.49$ and Happel's model, where the value of $\rho(r)$ is estimated numerically.

7.4 Conclusion

As the porosity of fractal aggregates increases radially with their size, we assume that the permeability also varies radially. We have modelled the permeability of fractal aggregates using an existing model (Veerapaneni et al [30]) in which we estimate the porous part out of R_β where flow velocity is meaningful. In the Veerapaneni model, the Brinkman equation holds, for flow inside the fractal aggregate, with the effective viscosity equal to the fluid viscosity. The permeability is assumed to vary radially and obeys to the Happel model. With these assumptions, the estimated hydrodynamic radius is in good agreement with our lattice Boltzmann simulation results.

Although the results obtained do agree between the analytical model and simulations, the assumptions in the model of Veerapaneni may not be relevant. Firstly, in our opinion, the Brinkman equation should hold at a transition zone defined by a thin layer between the porous medium and the Stokes region. This is also mentioned by Brinkman in his paper [86] that the equation is expected to work at very large permeability (or very small volume fraction (density) of the medium, where the permeability $k \to \infty$). Further evidence is seen in the work of Durlofsky et al [87] in which they found that the validity of the Brinkman equation can only hold at rather low volume fractions (e.g. about 0.05). We may find that inside fractal aggregates the volume fraction could be higher. In addition, the assumption of the effective viscosity can be considered as a constraint of the model since it is not necessary to postulate it equal to the normal fluid viscosity.

Using the Happel model for permeability, an agreement between the Veerapaneni model and lattice Boltzmann simulation results for the hydrodynamic radius can be reached. However, at this stage the validity of the Happel model for fractal aggregates still remains to be established. Finally, we argue that both the effective viscosity and the permeability model should be determined with freedom. Our later numerical fit of the Brinkman equation using lattice Boltzmann simulation data actually do not impose any constraints on the viscosity and the permeability, but lets them fit the equation numerically. The procedure is then more relevant and we found that the effective viscosity does not play any role inside porous region of fractal aggregates. Consequently, it makes the Brinkman equation fall back to Darcy's Law to become the governing equation for the internal flow inside fractal aggregates. Numerical results also suggest that permeability does not obey Happel's model and a new model is necessary for fractal aggregates.

Chapter 8

Conclusion

The initial goal of this work was to calculate settling velocities of fractal aggregates in sedimentation processes. We used the lattice Boltzmann method to simulate the fluid flow around fractal aggregates and obtain their hydrodynamic behaviour. We have determined the settling velocity indirectly by measuring the hydrodynamic radius of fractal aggregates quantitatively, and made further investigations into other hydrodynamic factors of fractal aggregates.

In this work, there are two components motivating the investigations. Firstly, there is insufficient understanding of the hydrodynamic behaviour of fractal aggregates. Mathematical modelling of settling fractal aggregates resulted in a big difference with experiments. In addition, previous works gave controversial results of the behaviour of fractal aggregates in fluids. Some of them used the same theory (e.g. Kirkwood Riseman theory) but gave different results. Although they are mathematically correct, some details of the phenomenon are missing. Secondly, there are very few investigations using numerical modelling and simulations. The lattice Boltzmann method has demonstrated its ability to reproduce physical phenomena at a macroscopic level based on simulating the system at a mesoscopic level. It thus gives ways to create a model to obtain the hydrodynamic behaviour of fractal aggregates .

The first part of this thesis has reviewed the previous results from studies on the hydrodynamic properties of fractal aggregates. Apart from the quantitatively controversial results of R_h/R_g, a qualitative conclusion has been found: the ratio of R_h/R_g should be a function of D_f. At this stage, a way to calculate the hydrodynamic radius of fractal aggregates was still missing and numerical simulations were few.

The determination of the hydrodynamic radius of fractal aggregates in the lattice Boltzmann simulations is not simple and straightforward: external effects on the measurements have always been visible in both 2D and 3D simulations. Although the 2D simulations do not provide a realistic experiment, they give a good example to explore the effect of the fractal shape on hydrodynamic behaviour. The fractal dimension D_f, in 2D case, was found not to appear in the hydrodynamic

properties.
Our 3D simulation results have demonstrated that, R_h/R_g is a function of D_f, and does not depend on fractal size N (or the mass of the aggregate). However, D_f is not the only factor to control the value of R_h/R_g since the prefactor and the building mechanism also play their parts. Consequently, a new quantity, connectivity, was found. This quantity plays a key role in the hydrodynamic properties of fractal aggregates. Finally, by using lattice Boltzmann simulation data to determine the permeability model of fractal aggregates, we found that the governing equation of the flow inside fractal aggregates is Darcy's Law, not the Brinkman equation. This is in opposition to previous works.
As usual, when work has been done, new questions appear which open up further developments. The following points can be considered for further developments to make a better picture of the work.
A comparison of simulation and experimental results with exactly the same fractal aggregates is always desirable. To do this, one may need real physical properties of fractal aggregates and a conversion from simulation results to reality.
As seen in 2D simulations, the measured force acting on the fractal aggregate and its relation to the mean velocity depends on the orientation to the main flow. The dependence tends to decrease with the size of the aggregate, however in the 3D case, it is not yet clear whether the fluid senses the position of fractal aggregates or not. In an initial attempt, we have made simulations for several positions of a 3D fractal aggregate of medium size (i.e. N=1000) and found that the difference between the reference position and that of orthogonally rotated $\pi/2$ to the flow direction was rather small. However, more experiments can help to confirm the independence of results to the fractal aggregate position.
In the last part of the thesis, we have measured the permeability of fractal aggregates radially and found the Happel model is not the one for determining the permeability of fractal aggregates, thus one needs a new permeability model to explain it.
During the lattice Boltzmann simulations, fractal aggregates did not deform themselves under frictional forces due to very low Reynolds number flows. However, it would be very interesting to simulate the aggregates deforming and self-reconstructing under shear effects. To do it, moving boundary conditions may required to fulfill the work. The interaction of solid-solid is also an issue for development.
The last development to make the simulations more realistic is to make up the elementary particles of fractal aggregates as spheres. This may require a huge computational effort as well as complicated boundary treatments.

Finally, to the best of our knowledge, this is the first study to perform accurate 3D numerical simulations for the determination of the hydrodynamic properties of fractal aggregates. It is the first time such results are found with a detailed description. Compared to the initial goal, we consider our final results to be

very satisfactory. However, the way to reach the results is a long process, which requires the precision of every individual component. Thus, the more perfection we have, the more problems and directions appear. The journey onward is always difficult with many drawbacks but it is still worth going, as only the people on it will be enriched by the knowledge.

Appendix A

Characteristic radii

A.1 Radius of gyration of an impermeable disc (circular cylinder)

The definition of R_g is basically referred to as "A quantity with units of length obtained by dividing the moment of inertia I by the mass of the object M and taking the square root".

$$R_g = \sqrt{\frac{I}{M}} \tag{A.1}$$

However, if we consider a set of rigid objects (particles), gyration radius can be calculated as the square root of mass average of ${r_i}^2$, where ${r_i}^2$ is the square of distance of object ith to the mass centre. For special objects such as a circular disc, we can apply this definition for calculating the gyration radius as we already know that the mass centre coincides with the mass of the disc.

$${R_g}^2 = \frac{\sum\limits_i m_i {r_i}^2}{\sum\limits_i m_i} \tag{A.2}$$

We consider a small area formed at position r with the length of dr, a differential of r and a differential of arc dl made of a rotation of $d\phi$. dr and dl are small enough to consider this area as a rectangle. Its area is thus equal to $dr.dl$. Note that $dl = r.d\phi$ (see figure A.1).

We consider the density of the disc, ρ, to be equal to a constant. The mass of the differential area is then equal to $dm = \rho.r.dr.d\phi$. We write again the definition of R_g, but the sign $\sum_i$ is replaced with the sign $\int\limits_S$, where $\int\limits_S$ is taken over all the

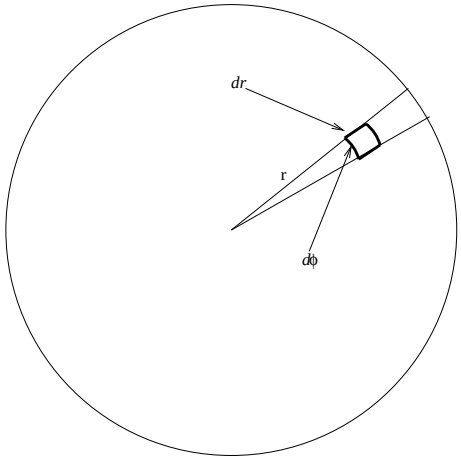

Figure A.1: A differential area of the disc.

area of the disc.

$$R_g{}^2 = \frac{1}{M}\int_S r^2.dm \tag{A.3}$$

where M is the mass of the disc, $M = \rho\pi R^2$, R is the radius of the disc.

$$R_g{}^2 = \frac{1}{M}\int_S r^2.dm = \frac{1}{M}\int_r r^2.r.dr \int_\phi d\phi = \frac{1}{M}\Big(\frac{1}{4}r^4\Big|_0^R \times \phi\Big|_0^{2\pi}\Big) \tag{A.4}$$

$$= \frac{1}{\rho\pi R^2}\frac{\rho 2\pi R^4}{4} = \frac{1}{2}R^2 \tag{A.5}$$

For a circular disc with radius R, the gyration radius is

$$\boxed{R_g = \sqrt{\frac{1}{2}}R}$$

A.2 Ratio of hydrodynamic radius to gyration radius for a sphere

For a sphere, the mass centre is also its centre. We can apply the definition (A.2) to calculate the gyration radius.
Consider a volume at position $A(r, \phi, \theta)$ that is small enough to become a cubic box with dimension l_1, l_2, l_3 where $l_1 = dr$: a differential along r; $l_2 = rd\theta$ and $l_3 = rsin\theta d\phi$ (see figure A.2) using formula (A.2) in this case, the sign $\sum_i$ will

be replaced by the $\int_V$ over the whole volume of the sphere. We denote M is the mass of the sphere, then we have

$$dm = r^2 \rho dr.rsin\theta d\phi.rd\theta \tag{A.6}$$

$$R_g^2 = \frac{1}{M}\int\limits_V r^2.\rho dr.rsin\theta d\phi.rd\theta = \frac{1}{M}\rho\int\limits_V r^2.dr.rsin\theta d\phi.rd\theta \tag{A.7}$$

where $M = \frac{4}{3}\pi R^3\rho$ and ρ is the density of mass of the sphere. The density is , in this case, considered a constant. The integral part in formula (A.7) can be expressed as:

$$\int\limits_V r^2 dr.rsin\theta d\phi.rd\theta = \int\limits_r r^4 dr \int\limits_\phi d\phi \int\limits_\theta sin\theta d\theta \tag{A.8}$$

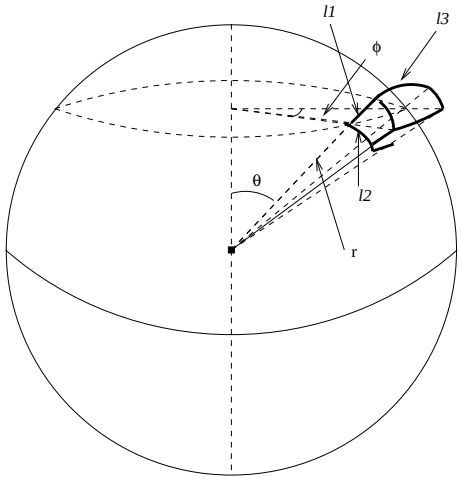

Figure A.2: A differential volume of sphere.

In the spherical coordinate, we have $r \ni [0, R]$, $\phi \ni [0, 2\pi]$ and $\theta \ni [0, \pi]$

$$\int\limits_r r^4 dr \int\limits_\phi d\phi \int\limits_\theta sin\theta d\theta = \int\limits_0^R r^4 dr \int\limits_0^{2\pi} d\phi \int\limits_0^{\pi} sin\theta d\theta \tag{A.9}$$

$$= \frac{1}{5}r^5\Big|_0^R \times \phi\Big|_0^{2\pi} \times (-cos\theta)\Big|_0^{\pi} = \frac{4\pi}{5}R^5 \tag{A.10}$$

Replace (A.10) in the equation (A.7), we have

$$R_g{}^2 = \frac{1}{M}\rho\frac{4\pi}{5}R^5 \tag{A.11}$$

Note that, the mass of the sphere M can be easily estimated $M = \frac{4}{3}\pi R^3\rho$, then we have

$$R_g{}^2 = \frac{1}{M}\rho\frac{4\pi}{5}R^5 = \frac{\rho\frac{4\pi}{5}R^5}{\rho\frac{4\pi}{3}R^3} = \frac{3}{5}R^2 \tag{A.12}$$

As the hydrodynamic radius of a sphere is the same as the radius of itself, we have the final ratio of hydrodynamic radius over the radius for a sphere as

$$\boxed{\frac{R_h^2}{R_g^2} = \frac{5}{3} \text{ or } \frac{R_h}{R_g} = \sqrt{\frac{5}{3}} \approx 1.291} \tag{A.13}$$

A.3 Derivation of outer radius for spherically symmetrical fractal aggregates

In this section, we derive the relationship between outer radius of a spherically symmetrical fractal aggregate and its gyration radius in 3D. The outer radius of a fractal aggregate is defined as the radius of the circumscribed sphere of the aggregate. For a spherically symmetrical fractal aggregate, the centre of mass can be supposed to coincide with the circumscribed sphere and when mentioning the centre of the fractal aggregate one would mean the centre of mass. Let's start with the distribution of particles of the fractal aggregate, with a certain sphere centred at the centre of the aggregate and having a radius r, the density of the particles of the aggregate is

$$c(r) = \frac{\text{Number of particles}}{\text{Volume}} = \frac{Br^{D_f}}{\frac{4}{3}\pi r^3} = \frac{3B}{4\pi}r^{D_f-3} = Ar^{D_f-3} \tag{A.14}$$

where B and A are some constants. D_f is the fractal dimension of the fractal aggregate.

Consider a differential distance dr making up a differential shell lying between r and $r + dr$. Number of particles within this shell is

$$dN = \frac{4}{3}\pi((r+dr)^3 - r^3).Ar^{D_f-3} \qquad \text{(A.15)}$$

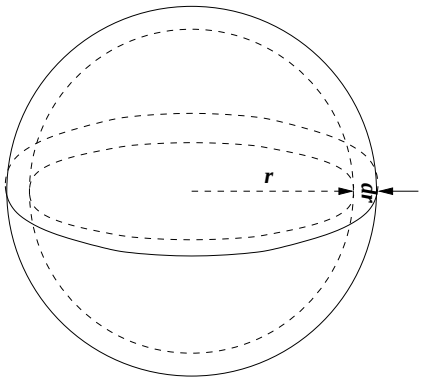

Expanding $((r+dr)^3 - r^3)$, we can safely ignore the second and third order of dr and we have:

$$\begin{aligned}(r+dr)^3 - r^3 &= r^3 + 3r^2dr + 3rdr^2 + dr^3 - r^3 \\ &= 3r^2dr + 3rdr^2 + dr^3 \approx 3r^2dr\end{aligned}$$

The equation (A.15) becomes

$$dN = \frac{4}{3}\pi.(3r^2)dr.Ar^{D_f-3} = 4\pi Ar^{D_f-1}dr \qquad \text{(A.16)}$$

Total number of particles of the fractal aggregate is

$$N = \int_0^{R_{out}} 4\pi Ar^{D_f-1}dr = \frac{4\pi A}{D_f}R_{out}^{D_f} \qquad \text{(A.17)}$$

where R_{out} is the outer radius of the fractal aggregate.
Now we look at the radius of gyration, by definition, gyration radius is

$${R_g}^2 = \frac{1}{N}\sum_{i=1}^{N} {r_i}^2 \qquad \text{(A.18)}$$

where r_i is the distance from the centre of the fractal aggregate to particle i. In fact, the gyration radius is the mean square of distances from the centre to particles of the aggregates, thus, we can estimate R_g using the density function of the particles $c(r)$ in (A.14). Again, the total square distance of particles in the differential shell dr is equal to r^2dN, then we have

$${R_g}^2 = \frac{1}{N}\int_0^{N} r^2 dN \qquad \text{(A.19)}$$

Replace (A.16) to (A.19) and change the differential variable to dr, we have

$${R_g}^2 = \frac{1}{N}\int_0^{R_{out}} r^2 4\pi Ar^{D_f-1}dr = \frac{1}{N}\int_0^{R_{out}} 4\pi Ar^{D_f+1}dr = \frac{1}{N}\frac{4\pi A}{D_f+2}R_{out}^{D_f+2} \qquad \text{(A.20)}$$

Now, we replace (A.17) to (A.20)

$$R_g{}^2 = \frac{\frac{4\pi A}{D_f+2}R_{out}^{D_f+2}}{\frac{4\pi A}{D_f}R_{out}^{D_f}} = \frac{D_f}{D_f+2}R_{out}^2 \tag{A.21}$$

So, for spherically symmetric fractal aggregates, outer radius is related to gyration radius as

$$\boxed{R_{out} = \sqrt{\frac{D_f+2}{D_f}}R_g} \tag{A.22}$$

Appendix B

Hydrodynamics of fractal aggregates in 2D

B.1 Accuracy comparison of bounce-back and mass-conserving boundaries

The table B.1 shows the numerically estimated errors of the Lattice Boltzmann simulation using bounce-back and mass-conserving boundaries with analytical solution of Sangani-Acrivos. The errors are defined as

$$e = \left| \frac{F}{\mu u} - \frac{4\pi}{log c^{1/2} - 0.738 + c - 0.887c^2 + 2.038c^3} \right| \tag{B.1}$$

Volume concentration	Bounce-back error (%)	Mass-conserving error (%)
0.42177275431291	126.867520960023	43.4167137004222
0.35012345679012	36.3806687898009	12.6846506078868
0.29529362765514	13.3383340245011	0.901535640613948
0.25240299038804	5.89539654214233	5.31390274862586
0.21822099107418	3.11896481519798	6.36637562664312
0.19054017737167	1.92564218021093	6.31599015015508
0.16781065088757	1.37642513013427	5.93690582882511
0.14891829447595	1.08623068038537	5.49144030675152
0.13304559954963	0.930017953820462	5.06609449292163
0.11958171698431	0.835048888492398	4.6856467999815
0.10806279530559	0.772381679899154	4.35319100536723
0.098131487889273	0.727793744182981	4.06463766546721
0.089508900391365	0.691270278906885	3.81406326712667
0.081974794773962	0.664595774098368	3.59561901716476
0.07535338505686	0.642373837855383	3.40413958892465
0.069502989902951	0.621746122413559	3.23525630195716
0.064308390022676	0.603990111154948	3.08533827865786
0.059675111522599	0.588507244443049	2.95138413866608
0.055525099851202	0.574929846855349	2.83090595828685
0.05179341076777	0.563038761781945	2.72182870474909
0.048425653985384	0.552715967658674	2.62240734427755
0.045376	0.543261491190551	2.53115503160118
0.042605612643471	0.535487777452213	2.44679060685329
0.040081406523828	0.529418208500466	2.36819149043059
0.037775054611327	0.524678875605842	2.29435906338513

Table B.1: The accuracy of bounce-back and mass-conserving boundary by comparison with the Sangani-Acrivos solution for flow past an array of cylinders

Appendix C

Hydrodynamics of fractal aggregates in 3D

C.1 Simulation results of 3D fractal aggregates

In this section, we present the hydrodynamic results of fractal aggregates obtained from our Lattice Boltzmann simulations. One can see from the simulation data that there is clear fluctuation in both measurements of R_h and R_g, thus making the R_h/R_g oscillate considerably. For fractal aggregates, even R_g is a geometrical factor and is not expected not to vary strongly for a given set of fractal aggregates generated in the same conditions, but obtained objects show an obvious fluctuation. For instance, the WS aggregates with $P = 0.01$, their theoretical $D_f = 3$, however, measurement of D_f from slope of $log(N) - log(R_g)$ gives D_f either up to 3.12 or 2.8 depending on the size of population we measure (e.g. we may argue that by excluding some small fractals from the measurement would give better results, but experimentally, the results obtained do not support this: D_f is bigger than 3). In order to obtain good results, statistical treatments are necessary.
As we have seen that R_h have the same scaling as R_g

$$N = \gamma_g(\frac{R_g}{a})^{D_f} = \gamma_h(\frac{R_h}{a})^{D_f} \tag{C.1}$$

Thus, it makes

$$\frac{R_h}{R_g} = (\frac{\gamma_g}{\gamma_h})^{\frac{1}{D_f}} \tag{C.2}$$

From the simulation results we see that variations of R_h goes accordingly with the variation of R_g. Then, we deduce that the correct R_h/R_g can be obtained if we find the correct γ_h, γ_g and D_f. The γ_g and D_f are usually found from intercept and slope of a linear fit in $log(N) - log(R_g)$. We know that the fit line of $log(N) - log(R_h)$ should give the same slope for the same D_f. Statistically,

the best γ_h can be obtained from the intercept of a fit line having the same slope as $log(N) - log(R_g)$ to $log(N) - log(R_h)$ data. This fit line is made by using the same slope of $log(N) - log(R_g)$ and having a minimized distance to the data of $log(N) - log(R_h)$. We implement this procedure to different populations of N until we find the convincing results. The following tables give the estimation

Fractals	D_f	$\frac{Rh}{Rg}$
CCA	1.9855	0.981
WS	2.493	1.245
WS	3	1.29

Table C.1: Ratio $\frac{R_h}{R_g}$ for several D_f

N	R_g	R_h	R_β	$\frac{R_h}{R_g}$
100	3.52	4.23	3.41	1.2036
200	4.51	5.36	4.76	1.1893
500	5.88	7.45	7.10	1.2674
1000	7.27	9.45	9.20	1.2998
3000	10.62	14.15	13.43	1.3324
5000	12.35	16.59	16.62	1.3438
7000	13.89	18.72	18.43	1.3477
10000	15.67	20.91	20.45	1.334

Table C.2: Hydrodynamic results of WS aggregates. The fractal aggregates are generated using sticking probability P=0.01 and having $D_f = 3$

N	R_g	R_h	R_β	$\frac{R_h}{R_g}$
100	4.03	4.81	3.98	1.193
200	5.464	6.18	5.64	1.131
500	8.17	9.47	8.88	1.16
1000	10.46	12.83	11.83	1.226
3000	16.36	21.34	18.47	1.304
5000	20.15	25.67	24.59	1.274
7000	22.63	29.78	28.73	1.316
10000	26.422	33.95	31.42	1.285
20000	35.42	45.11	44.34	1.273

Table C.3: Hydrodynamic results of WS aggregates. The fractal aggregates are generated using sticking probability P=1 and having $D_f = 2.49$

N	R_g	R_h	R_β	$\frac{R_h}{Rg}$
100	5.52794	4.97976	4.3213	0.901
200	8.42374	7.46712	6.57988	0.8864
500	13.550948	12.33686	10.42838	0.9104
1000	18.5144	17.99492	15.03406	0.9719
2000	25.9239	26.283033	21.5946	1.0138
3000	32.5325	31.9573	27.30735	0.9823
5000	41.83288	45.60672	31.82128	1.0902
7000	47.785075	53.58185	37.31272	1.1213

Table C.4: Hydrodynamic results of CCA aggregates. The fractal aggregates are generated using sticking probability P=1 and having $D_f = 1.98$

Number of fit points, N	$\frac{R_h}{R_g}$	Corresponding D_f	Theoretical D_f
8	1.2901	3.078	3
7	1.301	3.1174	3
6	1.3206	3.0499	3
5	1.3314	3.0167	3
4	1.3395	3.0824	3
3	1.3418	2.9077	3
2	1.3408	2.9565	3

Table C.5: WS fractals with $P = 0.01$: Using slope of $log(N) - log(R_g)$, a fit line is made to $log(N) - log(R_h)$. N is cut down toward the biggest sizes of fractal aggregates (e.g. $N = 2$ using the data of 7000 and 10000 particles)

Number of fit points	$\frac{R_h}{R_g}$	Corresponding D_f	Theoretical D_f
9	1.2409	2.4686	2.5
8	1.2446	2.4934	2.5
7	1.2617	2.5134	2.5
6	1.2797	2.4703	2.5
5	1.2905	2.4635	2.5
4	1.2869	2.432	2.5
3	1.2914	2.3453	2.5
2	1.2792	2.3639	2.5

Table C.6: WS fractals with $P = 1$: Using slope of $log(N) - log(R_g)$, a fit line is made to $log(N) - log(R_h)$. N is cut down toward the biggest sizes of fractal aggregates (e.g. $N = 2$ using the data of 7000 and 10000 particles)

Number of fit points	$\frac{R_h}{R_g}$	Corresponding D_f	Theoretical D_f
8	0.9813617	1.98556	2
7	0.9934388	2.038379	2
6	1.012488	2.054546	2
5	1.034239	2.020564	2
4	1.050427	2.041337	2
3	1.06291	2.188655	2
2	1.105651	2.529282	2

Table C.7: CCA fractals with $P = 1$: Using slope of $log(N) - log(R_g)$, a fit line is made to $log(N) - log(R_h)$. N is cut down toward the biggest sizes of fractal aggregates (e.g. $N = 2$ using the data of 7000 and 10000 particles)

C.2 Numerical simulations with artificial fractal aggregates

In this section, we present the results obtained with artificial fractal aggregates:
- The results of artificial aggregates $D_f = 3$ and $D_f = 1.98$ having different γ than that of real fractal aggregates.
- The results of artificial aggregates having the same $D_f = 2.49$ and $\gamma = 0.544$ as fractal aggregates (WS with $P = 1$).

N	R_g	R_h	R_β	R_{out}	$\frac{R_h}{R_g}$
1968	10.8675	13.3716	13.3661	14.5149	1.2304
2941	12.4159	15.3808	15.3494	16.6483	1.2388
4190	13.9568	17.393	17.3836	18.5679	1.2462
5750	15.5217	19.4066	19.4128	20.6032	1.2503
7655	17.0607	21.3935	21.3812	22.6462	1.254
9941	18.6133	23.4115	23.421	24.7553	1.2578

Table C.8: Artificial fractal with $D_f = 3$ and $\gamma = 0.125$

N	R_g	R_h	R_b	R_{out}	$\frac{R_h}{R_g}$
1542	11.928	14.8019	14.7465	16.5928	1.2409
2699	14.9135	18.7042	18.66	20.641	1.2542
4262	17.9109	22.7733	22.5488	24.6497	1.2715
6270	20.8845	26.6128	26.4658	28.5524	1.2743
8759	23.8613	30.6776	30.4047	32.5659	1.2857
11762	26.844	34.6777	34.3595	36.6982	1.2918

Table C.9: Artificial fractal with $Df = 2.49$, $\gamma = 0.544$

Appendix D

Permeability models for fractal aggregates

D.1 Radially varying permeability model

In this part, we present the mathematical solution of the radially varying permeability model of Veerapaneni and Wiesner [30], where we consider the fractal aggregates with an internal solid core. We start by formulating the problem mathematically again. First, the fractal aggregate is divided into 3 regions as in figure D.1

Stokes region

$$\mu\nabla^2 u = \nabla p \qquad R_{out} \leq r < \infty \tag{D.1}$$

$$\nabla . u = 0 \qquad R_{out} \leq r < \infty \tag{D.2}$$

Porous region

$$\nabla p^* = -\frac{\mu}{k_i} u^* + \mu^* \nabla^2 u^* \qquad r_{i-1} \leq r \leq r_i \tag{D.3}$$

and

$$\nabla . u^* = 0 \qquad r_{i-1} \leq r \leq r_i \tag{D.4}$$

Impermeable region

$$u = 0 \qquad r \leq R_\beta \tag{D.5}$$

The subscript i denotes the values within i-shell and the superscript (*) denotes any macroscopically averaged quantity pertaining specially to the given shell.

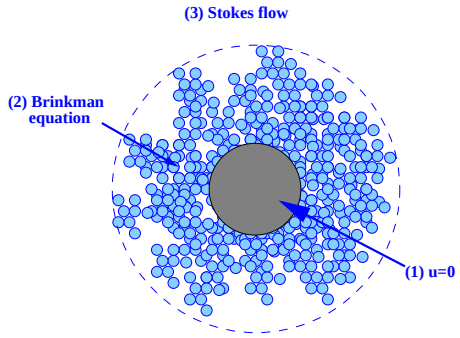

Figure D.1: Flow through a fractal aggregate

Boundary conditions

The boundary conditions are composed of the following components:
- The velocity far from the fractal aggregate ($r \to \infty$)is uniform and equal to u_∞
- At the boundaries between spherical shells, the tangential components of fluid velocity and stress tensor are continuous. It is the same as the outermost shell boundary.
- At the surface of solid core, fluid velocity is zero.
Mathematically the boundary conditions are written as:

$$u(r \to \infty, \theta) = -u_\infty i_z \tag{D.6}$$

$$u^*(R_{out}, \theta) = u(R_{out}, \theta) \tag{D.7}$$

$$\tau^*_{rr}(R_{out}, \theta) = \tau_{rr}(R_{out}, \theta) \tag{D.8}$$

$$\tau^*_{r\theta}(R_{out}, \theta) = \tau_{r\theta}(R_{out}, \theta) \tag{D.9}$$

$$u^*(r_{i-1}, \theta) = u(r_i, \theta) \tag{D.10}$$

$$\tau^*_{rr}(r_{i-1}, \theta) = \tau_{rr}(r_i, \theta) \tag{D.11}$$

$$\tau^*_{r\theta}(r_{i-1}, \theta) = \tau_{r\theta}(r_i, \theta) \tag{D.12}$$

$$u^*(R_\beta, \theta) = 0 \tag{D.13}$$

where the r_i is the radius from the mass centre to the outer boundary of the shell i. The components of stress tensor in spherical coordinates are expressed as:

$$\tau_{rr}(r,\theta) = p - 2\mu(\frac{\partial u_r}{\partial r}) \tag{D.14}$$

$$\tau_{r\theta}(r,\theta) = \mu(\frac{1}{r}\frac{\partial u_r}{\partial \theta} + \frac{\partial u_\theta}{\partial r} - \frac{u_\theta}{r}) \tag{D.15}$$

$$\tau^*_{rr}(r,\theta) = p^* - 2\mu^*(\frac{\partial {u_r}^*}{\partial r}) \tag{D.16}$$

$$\tau^*_{r\theta}(r,\theta) = \mu^*(\frac{1}{r}\frac{\partial {u_r}^*}{\partial \theta} + \frac{\partial {u_\theta}^*}{\partial r} - \frac{{u_\theta}^*}{r}) \tag{D.17}$$

where p is the pressure. We can safely assume that the pressure to be satisfied the continuity condition, that is

$$p^*(r_i,\theta) = p^*(r_{i+1},\theta) \tag{D.18}$$

$$p(R_{out},\theta) = p^*(R_{out},\theta) \tag{D.19}$$

Method of solution

Due to the axisymmetry of the flow, we can introduce stream functions Ψ and Ψ^* for the Stokes and porous regions respectively. They are related to the velocities of the corresponding flow as following definitions:

$$u_r = \frac{-1}{r^2\sin\theta}\frac{\partial \Psi}{\partial \theta} \tag{D.20}$$

$$u_\theta = \frac{1}{r\sin\theta}\frac{\partial \Psi}{\partial r} \tag{D.21}$$

$${u_r}^* = \frac{-1}{r^2\sin\theta}\frac{\partial \Psi^*}{\partial \theta} \tag{D.22}$$

$${u_\theta}^* = \frac{1}{r\sin\theta}\frac{\partial \Psi^*}{\partial r}. \tag{D.23}$$

By taking the curl of the Stokes equation D.1 and Brinkman equation D.3 we arrive at the equations:

$$E^4\Psi = 0 \qquad R_{out} \le r < \infty \tag{D.24}$$

$$E^4\Psi^* - \frac{1}{k}\frac{\mu}{\mu^*}E^2\Psi^* = 0 \qquad R_{out} \le r \le R_\beta \tag{D.25}$$

where

$$E^2 = \frac{\partial^2}{\partial r^2} + \frac{\sin\theta}{r^2}\frac{\partial}{\partial\theta}(\frac{1}{\sin\theta}\frac{\partial}{\partial\theta}) \tag{D.26}$$

In equation D.25, k is the permeability. We can replace $\frac{1}{k}\frac{\mu}{\mu^*}$ by $\frac{1}{K}$, and obtain

$$K = \frac{k}{\frac{\mu}{\mu^*}} = \frac{k}{\sigma} \tag{D.27}$$

where

$$\sigma = \frac{\mu}{\mu^*} \tag{D.28}$$

The general solution of equations D.24 and D.25 is given below [85]:

$$\Psi(\xi,\theta) = -\frac{K_n u_\infty \sin^2\theta}{2}[\frac{A1}{\xi} + A2\xi + A3\xi^2 + A4\xi^4] \tag{D.29}$$

$$\frac{R_{out}}{\sqrt{K_n}} \leq \xi < \infty$$

$$\Psi_i{}^*(\xi_i,\theta) = -\frac{K_i u_\infty \sin^2\theta}{2}[\frac{B1_i}{\xi_i} + B2_i{\xi_i}^2 + B3_i(\frac{\cosh\xi_i}{\xi_i} - \sinh\xi_i) + B4_i(\frac{\sinh\xi_i}{\xi_i} - \cosh\xi_i)] \tag{D.30}$$

$$\frac{r_{i-1}}{\sqrt{K_i}} \leq \xi_i \leq \frac{r_i}{\sqrt{K_i}}$$

where $\xi = \frac{r}{K}$ and $A1, A2, A3, A4$ and $B1_i, B2_i, B3_i, B4_i$ are constants.
In this model, the drag force F of fluid exerted on the fractal is calculated as follows:

$$F = \int_0^{2\pi} d\phi \int_0^{\pi} d\theta a^2 sin\theta dF \tag{D.31}$$

dF is computed from stress tensor τ_{rr} and $\tau_{r\theta}$ as:

$$dF = \tau_{rr}(R_{out},\theta)cos\theta - \tau_{r\theta}(R_{out},\theta)sin\theta \tag{D.32}$$

The drag force on the fractal aggregate is then expressed as:

$$F = 6\pi\mu u R_{out}\Omega \tag{D.33}$$

where Ω is defined as the ratio of force exerted by fluid on the fractal aggregate with radius R_{out} over the force exerted on an impermeable sphere of radius R_{out}.

$$\Omega = \frac{2A2\sqrt{K_n}}{3R_{out}} \tag{D.34}$$

The hydrodynamic radius of fractal aggregate is then connected to Ω and outer radius R_{out} as

$$R_h = \Omega.R_{out} \tag{D.35}$$

Solving the problem mathematically

Our goal is to estimate the coefficients $A1, A2, A3, A4$ and $B1_i, B2_i, B3_i, B4_i$ from the system of equations, formulated using boundary conditions, then estimate the hydrodynamic radius R_h using equation (D.35).

We start with solving the problem by deriving $\frac{\partial\Psi}{\partial r}$, $\frac{\partial\Psi}{\partial\theta}$. As the stream functions are written as a function of ξ, then the derivatives with respect to r can be taken with respect to ξ and multiplied with derivative of ξ taken respect to r as we have

$$\frac{\partial\Psi}{\partial r} = \frac{\partial\Psi}{\partial\xi}.\frac{\partial\xi}{\partial r}$$
$$\frac{\partial\xi}{\partial r} = \frac{1}{\sqrt{K}}$$

We use the first boundary condition (D.6) to find two coefficients of Ψ as it helps to simplify the mathematical expressions in later equations.
For the Stokes region, we always have

$$\frac{\partial\xi}{dr} = \frac{1}{\sqrt{K_n}}$$
as
$$K = K_n$$

Taking the derivatives of stream function and plugging them to obtain u_r and u_θ we have

$$\frac{\partial \Psi}{\partial \theta} = -K_n u_\infty \sin\theta \cos\theta (\frac{1}{\xi} A1 + \xi A2 + \xi^2 A3 + \xi^4 A4) \tag{D.36}$$

$$\frac{\partial \Psi}{\partial r} = \frac{-K_n u_\infty \sin^2\theta}{2} (-\frac{1}{\xi^2} A1 + A2 + 2\xi A3 + 4\xi^3 A4). \frac{\partial \xi}{\partial r} = \frac{-\sqrt{K_n} u_\infty \sin^2\theta}{2} (-\frac{1}{\xi^2} A1 + A2 + 2\xi A3 + 4\xi^3 A4) \tag{D.37}$$

$$u_r = -\frac{1}{r^2 \sin\theta} \frac{\partial \Psi}{\partial \theta} = K_n u_\infty \cos\theta \frac{1}{r^2} (\frac{1}{\xi} A1 + \xi A2 + \xi^2 A3 + \xi^4 A4) \tag{D.38}$$

$$u_\theta = \frac{1}{r \sin\theta} \frac{\partial \Psi}{\partial r} = -\frac{K_n u_\infty \sin\theta}{2} \frac{1}{r} (-\frac{1}{\xi^2} A1 + A2 + 2\xi A3 + 4\xi^3 A4). \frac{\partial \xi}{\partial r} = -\frac{\sqrt{K_n} u_\infty \sin\theta}{2} \frac{1}{r} (-\frac{1}{\xi^2} A1 + A2 + 2\xi A3 + 4\xi^3 A4) \tag{D.39}$$

As the boundary condition in equation (D.6) can be written down in 2 components r and θ as

$$u_r = u_\infty \cos\theta$$
$$u_\theta = -u_\infty \sin\theta$$

We substitute equation (D.38) and equation (D.39) to this boundary condition and obtain

$$K_n u_\infty \cos\theta \frac{1}{r^2} (\frac{1}{\xi} A1 + \xi A2 + \xi^2 A3 + \xi^4 A4) = u_\infty \cos\theta$$
$$-\frac{\sqrt{K_n} u_\infty \sin\theta}{2} \frac{1}{r} (-\frac{1}{\xi^2} A1 + A2 + 2\xi A3 + 4\xi^3 A4) = -u_\infty \sin\theta$$

or

$$K_n \frac{1}{r^2}(\frac{1}{\xi}A1 + \xi A2 + \xi^2 A3 + \xi^4 A4) = 1$$
$$\frac{\sqrt{K_n}}{2}\frac{1}{r}(-\frac{1}{\xi^2}A1 + A2 + 2\xi A3 + 4\xi^3 A4) = 1$$

Replace $\xi = \dfrac{r}{\sqrt{K_n}}$ in these two equations. We have

$$K_n(\frac{\sqrt{K_n}}{r^3}A1 + \frac{1}{r\sqrt{K_n}}A2 + \frac{1}{K_n}A3 + \frac{r^2}{{K_n}^2}A4) = 1$$
$$\frac{\sqrt{K_n}}{2}(-\frac{K_n}{r^3}A1 + \frac{\sqrt{K_n}}{r}A2 + \frac{2}{\sqrt{K_n}}A3 + \frac{4r^2}{K_n\sqrt{K_n}}A4) = 1$$

Note that these coefficients must satisfy the condition $r \to \infty$, it is easily seen that both equations can be satisfied only if $A4 = 0$ and $A3 = 1$.
So the stream function Ψ for Stokes region has been simplified to

$$\Psi = -\frac{K_n u_\infty \sin^2\theta}{2}(\frac{1}{\xi}A1 + \xi A2 + \xi^2) \tag{D.40}$$

Model of 1 porous shell with a solid core

We first consider the simplest case: the fractal aggregate is described with a solid core and only one porous shell. This is the case of n=1. In this model, we have boundary conditions at 2 surfaces: $r = R_{out}$ and $r = R_\beta$. The coefficients of stream functions Ψ and Ψ^* can be estimated by setting up a system of linear equations from the boundary conditions, given that permeability of the porous shell and viscosity are known and, hence, Ω can be estimated. It is then possible to estimate the hydrodynamic radius from Ω. For that, we start writing down all the equations (D.7)→(D.13) and from those, a system of linear equations would be formed where the variables are the coefficients $A1, A2, B1, B2, B3, B4$. For this model, we have 6 unknown coefficients in stream functions Ψ and Ψ^*. To avoid any mistakes which can happen during mathematical deriving, we express, step by step, all the terms to build up the appropriate quantities before joining them together to formulate the complete equations. As mentioned before, all the derivatives taken with respect to r will be taken by taking with respect to ξ as we have

$$\frac{\partial \Psi}{\partial r} = \frac{\partial \Psi}{\partial \xi}\frac{\partial \xi}{\partial r}$$

$$\frac{\partial \xi}{\partial r} = \frac{1}{\sqrt{K_n}}$$

The solutions, for stream functions Ψ and Ψ^*, are expressed respectively as follows

$$\Psi = -\frac{K_n u_\infty \sin^2\theta}{2}(\frac{1}{\xi}A1 + \xi A2 + \xi^2) \tag{D.41}$$

$$\Psi^* = -\frac{K_n u_\infty \sin^2\theta}{2}[\frac{1}{\xi}B1 + \xi^2 B2 + (\frac{\cosh\xi}{xi} - \sinh\xi)B3 + (\frac{\sinh\xi}{\xi} - \cosh\xi)B4] \tag{D.42}$$

And we construct u_r, u_θ and $\tau_{rr}, \tau_{r\theta}$ as:

$$\frac{\partial\Psi}{\partial\theta} = -K_n u_\infty \sin\theta\cos\theta[\frac{1}{\xi}A1 + \xi A2 + \xi^2] \tag{D.43}$$

$$\frac{\partial\Psi}{\partial r} = \frac{\partial\Psi}{\partial\xi}\frac{\partial\xi}{\partial r} = -\frac{\sqrt{K_n}u_\infty \sin^2\theta}{2}[-\frac{1}{\xi^2}A1 + A2 + 2\xi] \tag{D.44}$$

$$u_r = -\frac{1}{r^2\sin\theta}\frac{\partial\Psi}{\partial\theta} = K_n u_\infty \cos\theta\frac{1}{r^2}[\frac{1}{\xi}A1 + \xi A2 + \xi^2) \tag{D.45}$$

$$u_\theta = \frac{1}{r\sin\theta}\frac{\partial\Psi}{\partial r} = -\frac{\sqrt{K_n}u_\infty \sin\theta}{2}\frac{1}{r}[-\frac{1}{\xi^2}A1 + A2 + 2\xi] \tag{D.46}$$

$$\frac{\partial u_r}{\partial r} = K_n u_\infty \cos\theta\frac{1}{r^2}[-\frac{2}{r}(\frac{1}{\xi}A1 + \xi A2 + \xi^2) + \frac{1}{\sqrt{K_n}}(-\frac{1}{\xi^2}A1 + A2 + 2\xi)] \tag{D.47}$$

$$= K_n u_\infty \cos\theta\frac{1}{r^2}[(-\frac{2}{r.\xi} - \frac{1}{\xi^2\sqrt{K_n}})A1 + (\frac{1}{\sqrt{K_n}} - \frac{2\xi}{r})A2 + (\frac{2\xi}{\sqrt{K_n}} - \frac{2\xi^2}{r})] \tag{D.48}$$

Then the component τ_{rr} of stress tensor is

$$\tau_{rr} = p - 2\mu\frac{\partial u_r}{\partial r} = p - 2\mu K_n u_\infty \cos\theta \frac{1}{r^2}[(-\frac{2}{r.\xi} - \frac{1}{\xi^2\sqrt{K_n}})A1 + (\frac{1}{\sqrt{K_n}} - \frac{2\xi}{r})A2 + (\frac{2\xi}{\sqrt{K_n}} - \frac{2\xi^2}{r})] \tag{D.49}$$

$$\frac{\partial u_r}{\partial \theta} = -K_n u_\infty \sin\theta \frac{1}{r^2}[\frac{1}{\xi}A1 + \xi A2 + \xi^2] \tag{D.50}$$

$$\frac{1}{r}\cdot\frac{\partial u_r}{\partial \theta} = -\frac{K_n u_\infty \sin\theta}{2}\frac{1}{r}[\frac{2}{r^2}(\frac{1}{\xi}A1 + \xi A2 + \xi^2)] \tag{D.51}$$

$$\frac{\partial u_\theta}{\partial r} = -\frac{\sqrt{K_n}u_\infty \sin\theta}{2}[-\frac{1}{r^2}(-\frac{1}{\xi^2}A1 + A2 + 2\xi) + \frac{1}{r}\frac{1}{\sqrt{K_n}}(\frac{2}{\xi^3}A1 + 2)] \tag{D.52}$$

$$= -\frac{\sqrt{K_n}u_\infty \sin\theta}{2}\frac{1}{r}[(\frac{1}{r\xi^2} + \frac{2}{\sqrt{K_n}\xi^3})A1 - \frac{1}{r}A2 + (\frac{2}{\sqrt{K_n}} - \frac{2\xi}{r})] \tag{D.53}$$

$$\tau_{r\theta} = \mu(\frac{1}{r}\frac{\partial u_r}{\partial \theta} + \frac{\partial u_\theta}{\partial r} - \frac{u_\theta}{r}) \tag{D.54}$$

$$= -\mu\frac{\sqrt{K_n}u_\infty \sin\theta}{2}\frac{1}{r}[(\frac{2\sqrt{K_n}}{r^2\xi} + \frac{2}{r\xi^2} + \frac{2}{\xi^3\sqrt{K_n}})A1 + (\frac{2\xi\sqrt{K_n}}{r^2} - \frac{2}{r})A2 + (\frac{2\xi^2\sqrt{K_n}}{r^2} + \frac{2}{\sqrt{K_n}} - \frac{4\xi}{r})] \tag{D.55}$$

The formation of u_r^*, u_θ^* and $\tau_{rr}^*, \tau_{r\theta}^*$ is constructed in the same way:

$$\frac{\partial \Psi^*}{\partial \theta} = -K_n u_\infty \sin\theta\cos\theta[\frac{1}{\xi}B1 + \xi^2 B2 + (\frac{\cosh\xi}{\xi} - \sinh\xi)B3 + (\frac{\sinh\xi}{xi} - \cosh\xi)B4] \tag{D.56}$$

$$\frac{\partial \Psi^*}{\partial r} = -\frac{\sqrt{K_n} u_\infty \sin^2\theta}{2}[-\frac{1}{\xi^2}B1 + 2\xi B2 + (\frac{\xi\sinh\xi - \cosh\xi}{\xi^2} - \cosh\xi)B3 + (\frac{\xi\cosh\xi - \sinh\xi}{\xi^2} - \sinh\xi)B4] \tag{D.57}$$

$$u_r^* = -\frac{1}{r^2\sin\theta}\frac{\partial \Psi^*}{\partial \theta} \tag{D.58}$$

$$= K_n u_\infty \cos\theta \frac{1}{r^2}[\frac{1}{\xi}B1 + \xi^2 B2 + (\frac{\cosh\xi}{\xi} - \sinh\xi)B3 + (\frac{\sinh\xi}{xi} - \cosh\xi)B4] \tag{D.59}$$

$$u_\theta^* = \frac{1}{r\sin\theta}\frac{\partial \Psi^*}{\partial r} \tag{D.60}$$

$$= -\frac{\sqrt{K_n} u_\infty \sin\theta}{2}\frac{1}{r}[-\frac{1}{\xi^2}B1 + 2\xi B2 + (\frac{\xi\sinh\xi - \cosh\xi}{\xi^2} - \cosh\xi)B3 + (\frac{\xi\cosh\xi - \sinh\xi}{\xi^2} - \sinh\xi)B4] \tag{D.61}$$

$$\frac{\partial u_r^*}{\partial r} = K_n u_\infty \cos\theta[-\frac{2}{r^3}(\frac{1}{\xi}B1 + \xi^2 B2 + (\frac{\cosh\xi}{\xi} - \sinh\xi)B3 + (\frac{\sinh\xi}{xi} - \cosh\xi)B4) \tag{D.62}$$

$$+ \frac{1}{r^2\sqrt{K_n}}(-\frac{1}{\xi^2}B1 + 2\xi B2 + (\frac{\xi\sinh\xi - \cosh\xi}{\xi^2} - \cosh\xi)B3 + (\frac{\xi\cosh\xi - \sinh\xi}{\xi^2} - \sinh\xi)B4)] \tag{D.63}$$

$$= K_n u_\infty \cos\theta \frac{1}{r^2}\times \tag{D.64}$$

$$[(-\frac{2}{r\xi} - \frac{1}{\xi^2\sqrt{K_n}})B1 + (\frac{2\xi}{\sqrt{K_n}} - \frac{2\xi^2}{r})B2 + [\frac{1}{\sqrt{K_n}}(\frac{\xi\sinh\xi - \cosh\xi}{\xi^2} - \cosh\xi) - \frac{2}{r}(\frac{\cosh\xi}{\xi} - \sinh\xi)]B3 \tag{D.65}$$

$$+ [\frac{1}{\sqrt{K_n}}(\frac{\xi\cosh\xi - \sinh\xi}{\xi^2} - \sinh\xi) - \frac{2}{r}(\frac{\sinh\xi}{\xi} - \cosh\xi)]B4] \tag{D.66}$$

$$\tau^*_{rr} = p^* - 2\mu^* \frac{\partial u^*_r}{\partial r} = p^* - 2\mu^* K_n u_\infty \cos\theta \frac{1}{r^2} \times \tag{D.67}$$

$$[(-\frac{2}{r\xi} - \frac{1}{\xi^2\sqrt{K_n}})B1 + (\frac{2\xi}{\sqrt{K_n}} - \frac{2\xi^2}{r})B2 + [\frac{1}{\sqrt{K_n}}(\frac{\xi\sinh\xi - \cosh\xi}{\xi^2} - \cosh\xi) - \frac{2}{r}(\frac{\cosh\xi}{\xi} - \sinh\xi)]B3 \tag{D.68}$$

$$+ [\frac{1}{\sqrt{K_n}}(\frac{\xi\cosh\xi - \sinh\xi}{\xi^2} - \sinh\xi) - \frac{2}{r}(\frac{\sinh\xi}{\xi} - \cosh\xi)]B4] \tag{D.69}$$

$$\frac{\partial u^*_\theta}{\partial r} = -\frac{\sqrt{K_n}u_\infty \sin\theta}{2} \times \tag{D.70}$$

$$[(-\frac{1}{r^2})(-\frac{1}{\xi^2}B1 + 2\xi B2 + (\frac{\xi\sinh\xi - \cosh\xi}{\xi^2} - \cosh\xi)B3 + (\frac{\xi\cosh\xi - \sinh\xi}{\xi^2} - \sinh\xi)B4) \tag{D.71}$$

$$+ \frac{1}{r\sqrt{K_n}}(\frac{2}{\xi^3}B1 + 2B2 + (\frac{\xi^2\cosh\xi - 2\xi\sinh\xi + 2\cosh\xi}{\xi^3} - \sinh\xi)B3 + (\frac{\xi^2\sinh\xi - 2\cosh\xi + 2\sinh\xi}{\xi^3} - \cosh\xi)B4)] \tag{D.72}$$

$$= -\frac{\sqrt{K_n}u_\infty \sin\theta}{2}\frac{1}{r} \times \tag{D.73}$$

$$[(\frac{1}{r\xi} + \frac{2}{\xi^3\sqrt{K_n}})B1 + (\frac{2}{\sqrt{K_n}} - \frac{2\xi}{r})B2 + [\frac{1}{\sqrt{K_n}}(\frac{\xi^2\cosh\xi - 2\xi\sinh\xi + 2\cosh\xi}{\xi^3} - \sinh\xi) - \frac{1}{r}(\frac{\xi\sinh\xi - \cosh\xi}{\xi^2} - \cosh\xi)]B3 \tag{D.74}$$

$$+ [\frac{1}{\sqrt{K_n}}(\frac{\xi^2\sinh\xi - 2\xi\cosh\xi + 2\sinh\xi}{\xi^3} - \cosh\xi) - \frac{1}{r}(\frac{\xi\cosh\xi - \sinh\xi}{\xi^2} - \sinh\xi)]B4] \tag{D.75}$$

then

$$\frac{\partial u_\theta^*}{\partial r} - \frac{u_\theta^*}{r} = -\frac{\sqrt{K_n}u_\infty \sin\theta}{2}\frac{1}{r} \times [(\frac{2}{r\xi^2} + \frac{2}{\xi^3\sqrt{K_n}})B1 + (\frac{2}{\sqrt{K_n}} - \frac{4\xi}{r})B2 \tag{D.76}$$

$$+ [\frac{1}{\sqrt{K_n}}(\frac{\xi^2\cosh\xi - 2\xi\sinh\xi + 2\cosh\xi}{\xi^3} - \sinh\xi) - \frac{2}{r}(\frac{\xi\sinh\xi - \cosh\xi}{\xi^2} - \cosh\xi)]B3 \tag{D.77}$$

$$+ [\frac{1}{\sqrt{K_n}}(\frac{\xi^2\sinh\xi - 2\xi\cosh\xi + 2\sinh\xi}{\xi^3} - \cosh\xi) - \frac{2}{r}(\frac{\xi\cosh\xi - \sinh\xi}{\xi^2} - \sinh\xi)]B4] \tag{D.78}$$

$$\frac{\partial u_r^*}{\partial \theta} = -\frac{K_n u_\infty \sin\theta}{2}[\frac{2}{r^2\xi}B1 + \frac{2\xi^2}{r^2}B2 + \frac{2}{r^2}(\frac{\cosh\xi}{\xi} - \sinh\xi)B3 + \frac{2}{r^2}(\frac{\sinh\xi}{\xi} - \cosh\xi)B4] \tag{D.79}$$

and

$$\frac{1}{r}\frac{\partial u_r^*}{\partial \theta} = -\frac{K_n u_\infty \sin\theta}{2}\frac{1}{r}[\frac{2}{r^2\xi}B1 + \frac{2\xi^2}{r^2}B2 + \frac{2}{r^2}(\frac{\cosh\xi}{\xi} - \sinh\xi)B3 + \frac{2}{r^2}(\frac{\sinh\xi}{\xi} - \cosh\xi)B4] \tag{D.80}$$

$$\tau_{r\theta}^* = \mu^*(\frac{1}{r}\frac{\partial u_r^*}{\partial\theta} + \frac{\partial u_\theta^*}{\partial r} - \frac{u_\theta^*}{r}) = -\mu^*\frac{K_n u_\infty \sin\theta}{2}\frac{1}{r}\times \tag{D.81}$$

$$[(\frac{2}{r^2\xi} + \frac{2}{r\xi^2} + \frac{2}{\xi^3\sqrt{K_n}})B1 + (\frac{2\sqrt{K_n}\xi^2}{r^2} - \frac{4\xi}{r} + \frac{2}{\sqrt{K_n}})B2 \tag{D.82}$$

$$+ [\frac{1}{\sqrt{K_n}}(\frac{\xi^2\cosh\xi - 2\xi\sinh\xi + 2\cosh\xi}{\xi^3} - \sinh\xi) - \frac{2}{r}(\frac{\xi\sinh\xi - \cosh\xi}{\xi^2} - \cosh\xi) + \frac{2\sqrt{K_n}}{r^2}(\frac{\cosh\xi}{\xi} - \sinh\xi)]B3 \tag{D.83}$$

$$+ [\frac{1}{\sqrt{K_n}}(\frac{\xi^2\sinh\xi - 2\xi\cosh\xi + 2\sinh\xi}{\xi^3} - \cosh\xi) - \frac{2}{r}(\frac{\xi\cosh\xi - \sinh\xi}{\xi^2} - \sinh\xi) + \frac{2\sqrt{K_n}}{r^2}(\frac{\sinh\xi}{\xi} - \cosh\xi)]B4 \tag{D.84}$$

Having found the necessary quantities, we would plug them to the boundary equations. The order of variables in the system of linear equations is kept as $X = (B1, B2, B3, B4, A1, A2)$, thus the system of linear equation would have the form of

$$\begin{aligned} m_{11}B1 + m_{12}B2 + \ldots + m_{15}A1 + m_{16}A2 &= n1 \\ m_{21}B1 + m_{22}B2 + \ldots + m_{25}A1 + m_{26}A2 &= n2 \\ &\vdots \\ m_{61}B1 + m_{62}B2 + \ldots + m_{65}A1 + m_{66}A2 &= n6 \end{aligned}$$

where

$$M = \begin{pmatrix} m_{11} & m_{12} & \ldots \\ m_{21} & m_{22} & \ldots \\ \vdots & \vdots & \ddots \end{pmatrix}$$

is the matrix with its values, which would be estimated numerically. We start equating the quantities in boundary conditions with (D.7)

$$u^*(R_{out}, \theta) = u(R_{out}, \theta)$$

$$\begin{aligned} u_r^*(R_{out}, \theta) &= u_r(R_{out}, \theta) \\ u_\theta^*(R_{out}, \theta) &= u_\theta(R_{out}, \theta) \end{aligned}$$

$$u_r^*(R_{out}, \theta) - u_r(R_{out}, \theta) = 0 \tag{D.85}$$

$$u_\theta^*(R_{out}, \theta) - u_\theta(R_{out}, \theta) = 0 \tag{D.86}$$

Replace $u_r^*, u_r, u_\theta^*, u_\theta$ from (D.59),(D.45),(D.61) and (D.46), observe that the terms $K_n, u_\infty, \cos\theta, \sin\theta$ which appear at the beginning, can be cancelled

$$\frac{1}{\xi}B1 + \xi^2 B2 + (\frac{\cosh\xi}{\xi} - \sinh\xi)B3 + (\frac{\sinh\xi}{\xi} - \cosh\xi)B4 - \frac{1}{\xi}A1 + \xi A2 = \xi^2 \tag{D.87}$$

$$-\frac{1}{\xi^2}B1 + 2\xi B2 + (\frac{\xi\sinh\xi - \cosh\xi}{\xi^2} - \cosh\xi)B3 + (\frac{\xi\cosh\xi - \sinh\xi}{\xi^2} - \sinh\xi)B4 + \frac{1}{\xi^2}A1 - A2 = 2\xi \tag{D.88}$$

where

$$r = R_{out}, \xi = \frac{R_{out}}{\sqrt{K_n}}$$

Equating two components of stress tensor at $r = R_{out}$ and $\xi = \frac{R_{out}}{\sqrt{K_n}}$: the equations (D.49) are equated with (D.69) and equation (D.55) with (D.84). Note that we suppose that the viscosity of fluid inside the fractal aggregate μ^* is not the same as the viscosity μ of that in the Stokes region. So we can have

$$\tau^*_{rr} = p^* - 2\mu^*\frac{\partial u^*_r}{\partial r} = p - 2\mu\frac{\partial u_r}{\partial r} = \tau_{rr}$$
$$\tau^*_{r\theta} = \mu^*(\frac{1}{r}\frac{\partial u^*_r}{\partial\theta} + \frac{\partial u^*_\theta}{\partial r} - \frac{u^*_\theta}{r}) = \mu(\frac{1}{r}\frac{\partial u_r}{\partial\theta} + \frac{\partial u_\theta}{\partial r} - \frac{u_\theta}{r}) = \tau_{r\theta}$$

The pressure terms p^* and p cancel each other as they are equal, due to the continuity condition. Then we have

$$\frac{\partial u^*_r}{\partial r} - \frac{\mu}{\mu^*}\frac{\partial u_r}{\partial r} = 0$$
$$\frac{1}{r}\frac{\partial u^*_r}{\partial\theta} + \frac{\partial u^*_\theta}{\partial r} - \frac{u^*_\theta}{r} - \frac{\mu}{\mu^*}(\frac{1}{r}\frac{\partial u_r}{\partial\theta} + \frac{\partial u_\theta}{\partial r} - \frac{u_\theta}{r}) = 0$$

or

$$\frac{\partial u_r^*}{\partial r} - \sigma \frac{\partial u_r}{\partial r} = 0 \tag{D.89}$$

$$\frac{1}{r}\frac{\partial u_r^*}{\partial \theta} + \frac{\partial u_\theta^*}{\partial r} - \frac{u_\theta^*}{r} - \sigma(\frac{1}{r}\frac{\partial u_r}{\partial \theta} + \frac{\partial u_\theta}{\partial r} - \frac{u_\theta}{r}) = 0 \tag{D.90}$$

where

$$\sigma = \frac{\mu}{\mu^*}$$

Plugging the appropriate terms we formulated above to these equations, we obtain

$$\begin{aligned}
&(-\frac{2}{r\xi} - \frac{1}{\xi^2\sqrt{K_n}})B1 + (\frac{2\xi}{\sqrt{K_n}} - \frac{2\xi^2}{r})B2 + [\frac{1}{\sqrt{K_n}}(\frac{\xi\sinh\xi - \cosh\xi}{\xi^2} - \cosh\xi) - \frac{2}{r}(\frac{\cosh\xi}{\xi} - \sinh\xi)]B3 \\
&+ [\frac{1}{\sqrt{K_n}}(\frac{\xi\cosh\xi - \sinh\xi}{\xi^2} - \sinh\xi) - \frac{2}{r}(\frac{\sinh\xi}{\xi} - \cosh\xi)]B4 - \sigma(-\frac{2}{r.\xi} - \frac{1}{\xi^2\sqrt{K_n}})A1 - \sigma(\frac{1}{\sqrt{K_n}} - \frac{2\xi}{r})A2 = \sigma(\frac{2\xi^2}{r} - \frac{2\xi}{\sqrt{K_n}})
\end{aligned} \tag{D.91}$$

$$\begin{aligned}
&(\frac{2}{r^2\xi} + \frac{2}{r\xi^2} + \frac{2}{\xi^3\sqrt{K_n}})B1 + (\frac{2\sqrt{K_n}\xi^2}{r^2} - \frac{4\xi}{r} + \frac{2}{\sqrt{K_n}})B2 \\
&+ [\frac{1}{\sqrt{K_n}}(\frac{\xi^2\cosh\xi - 2\xi\sinh\xi + 2\cosh\xi}{\xi^3} - \sinh\xi) - \frac{2}{r}(\frac{\xi\sinh\xi - \cosh\xi}{\xi^2} - \cosh\xi) + \frac{2\sqrt{K_n}}{r^2}(\frac{\cosh\xi}{\xi} - \sinh\xi)]B3 \\
&+ [\frac{1}{\sqrt{K_n}}(\frac{\xi^2\sinh\xi - 2\xi\cosh\xi + 2\sinh\xi}{\xi^3} - \cosh\xi) - \frac{2}{r}(\frac{\xi\cosh\xi - \sinh\xi}{\xi^2} - \sinh\xi) + \frac{2\sqrt{K_n}}{r^2}(\frac{\sinh\xi}{\xi} - \cosh\xi)]B4 \\
&- \sigma(\frac{2\sqrt{K_n}}{r^2\xi} + \frac{2}{r\xi^2} + \frac{2}{\xi^3\sqrt{K_n}})A1 - \sigma(\frac{2\xi\sqrt{K_n}}{r^2} - \frac{2}{r})A2 = \sigma(\frac{4\xi}{r} - \frac{2\xi^2\sqrt{K_n}}{r^2} - \frac{2}{\sqrt{K_n}})
\end{aligned} \tag{D.92}$$

The last boundary equation (D.13) applied on the surface of the solid core can be written with 2 components as:

$$u_r^*(R_\beta, \theta) = 0 \tag{D.93}$$
$$u_\theta^*(R_\beta, \theta) = 0 \tag{D.94}$$

or

$$\frac{1}{\xi}B1 + \xi^2 B2 + (\frac{\cosh\xi}{\xi} - \sinh\xi)B3 + (\frac{\sinh\xi}{xi} - \cosh\xi)B4 = 0 \tag{D.95}$$

$$-\frac{1}{\xi^2}B1 + 2\xi B2 + (\frac{\xi\sinh\xi - \cosh\xi}{\xi^2} - \cosh\xi)B3 + (\frac{\xi\cosh\xi - \sinh\xi}{\xi^2} - \sinh\xi)B4 = 0 \tag{D.96}$$

where

$$r = R_\beta, \xi = \frac{R_\beta}{\sqrt{K_n}}$$

The following page will be the summary of the system of linear equations we have constructed:

$$\frac{1}{\xi}B1 + \xi^2 B2 + (\frac{\cosh\xi}{\xi} - \sinh\xi)B3 + (\frac{\sinh\xi}{\xi} - \cosh\xi)B4 - \frac{1}{\xi}A1 + \xi A2 = \xi^2 \tag{D.97}$$

$$-\frac{1}{\xi^2}B1 + 2\xi B2 + (\frac{\xi\sinh\xi - \cosh\xi}{\xi^2} - \cosh\xi)B3 + (\frac{\xi\cosh\xi - \sinh\xi}{\xi^2} - \sinh\xi)B4 + \frac{1}{\xi^2}A1 - A2 = 2\xi \tag{D.98}$$

$$\begin{aligned}&(-\frac{2}{r\xi} - \frac{1}{\xi^2\sqrt{K_n}})B1 + (\frac{2\xi}{\sqrt{K_n}} - \frac{2\xi^2}{r})B2 + [\frac{1}{\sqrt{K_n}}(\frac{\xi\sinh\xi - \cosh\xi}{\xi^2} - \cosh\xi) - \frac{2}{r}(\frac{\cosh\xi}{\xi} - \sinh\xi)]B3\\ &+ [\frac{1}{\sqrt{K_n}}(\frac{\xi\cosh\xi - \sinh\xi}{\xi^2} - \sinh\xi) - \frac{2}{r}(\frac{\sinh\xi}{\xi} - \cosh\xi)]B4 - \sigma(-\frac{2}{r.\xi} - \frac{1}{\xi^2\sqrt{K_n}})A1 - \sigma(\frac{1}{\sqrt{K_n}} - \frac{2\xi}{r})A2 = \sigma(\frac{2\xi^2}{r} - \frac{2\xi}{\sqrt{K_n}})\end{aligned} \tag{D.99}$$

$$\begin{aligned}&(\frac{2}{r^2\xi} + \frac{2}{r\xi^2} + \frac{2}{\xi^3\sqrt{K_n}})B1 + (\frac{2\sqrt{K_n}\xi^2}{r^2} - \frac{4\xi}{r} + \frac{2}{\sqrt{K_n}})B2\\ &+ [\frac{1}{\sqrt{K_n}}(\frac{\xi^2\cosh\xi - 2\xi\sinh\xi + 2\cosh\xi}{\xi^3} - \sinh\xi) - \frac{2}{r}(\frac{\xi\sinh\xi - \cosh\xi}{\xi^2} - \cosh\xi) + \frac{2\sqrt{K_n}}{r^2}(\frac{\cosh\xi}{\xi} - \sinh\xi)]B3\\ &+ [\frac{1}{\sqrt{K_n}}(\frac{\xi^2\sinh\xi - 2\xi\cosh\xi + 2\sinh\xi}{\xi^3} - \cosh\xi) - \frac{2}{r}(\frac{\xi\cosh\xi - \sinh\xi}{\xi^2} - \sinh\xi) + \frac{2\sqrt{K_n}}{r^2}(\frac{\sinh\xi}{\xi} - \cosh\xi)]B4\\ &- \sigma(\frac{2\sqrt{K_n}}{r^2\xi} + \frac{2}{r\xi^2} + \frac{2}{\xi^3\sqrt{K_n}})A1 - \sigma(\frac{2\xi\sqrt{K_n}}{r^2} - \frac{2}{r})A2 = \sigma(\frac{4\xi}{r} - \frac{2\xi^2\sqrt{K_n}}{r^2} - \frac{2}{\sqrt{K_n}})\end{aligned} \tag{D.100}$$

where

$$r = R_{out}, \qquad \xi = \frac{R_{out}}{\sqrt{K_n}}$$

$$\frac{1}{\xi}B1 + \xi^2 B2 + (\frac{\cosh\xi}{\xi} - \sinh\xi)B3 + (\frac{\sinh\xi}{xi} - \cosh\xi)B4 + 0.A1 + 0.A2 = 0 \tag{D.101}$$

$$-\frac{1}{\xi^2}B1 + 2\xi B2 + (\frac{\xi\sinh\xi - \cosh\xi}{\xi^2} - \cosh\xi)B3 + (\frac{\xi\cosh\xi - \sinh\xi}{\xi^2} - \sinh\xi)B4 + 0.A1 + 0.A2 = 0 \tag{D.102}$$

where

$$r = R_\beta, \qquad \xi = \frac{R_\beta}{\sqrt{K_n}}$$

These linear equations can be solved, given that all the input values are known: R_{out}, R_β, K_n and σ (the ratio of viscosities). Remember that K_n is the effective permeability related to the real permeability as

$$K_n = \frac{k}{\sigma}$$

where k is the real permeability of the porous shell, which can be estimated by using a permeability model for the fractal aggregate.
Having found the coefficients, Ω can be estimated using formula (D.34) and thus the hydrodynamic radius is calculated from Ω as equation (D.35).

Model of n-shells with a solid core

The procedure to obtain the coefficients of the equation system is the same as for the model with 1-shell. With n-shells model, we have 4n+2 unknowns including $A1, A2,\ B1_i, B2_i, B3_i, B4_i$ where $i \in [1; n]$. Repeating again the procedure, we establish the system of equation as follows with explicit coefficients which we can easily compute.
r_i is the distance from the centre to shell i.
K_i is the permeability of shell i.
$\xi_i = \dfrac{r_i}{\sqrt{K_i}}$ and $\xi_{i+1} = \dfrac{r_i}{\sqrt{K_{i+1}}}$
Consider $\sigma = \dfrac{\mu}{\mu^*} = 1$, final equations are presented as follows:

$$\frac{1}{\xi_i}B1_i + {\xi_i}^2 B2_i + \Big(\frac{\cosh\xi_i}{\xi_i} - \sinh\xi_i\Big)B3_i + \Big(\frac{\sinh\xi_i}{\xi_i} - \cosh\xi_i\Big)B4_i = 0 \tag{D.103}$$

$$-\frac{1}{{\xi_i}^2}B1_i + 2\xi_i B2_i + \Big(\frac{\xi_i\sinh\xi_i - \cosh\xi_i}{{\xi_i}^2} - \cosh\xi_i\Big)B3_i + \Big(\frac{\xi_i\cosh\xi_i - \sinh\xi_i}{{\xi_i}^2} - \sinh\xi_i\Big)B4_i = 0 \tag{D.104}$$

Then we have $4n-4$ equations corresponding to continuity equations of velocity and stress tensor

$$\begin{aligned}&\frac{K_i}{\xi_i}B1_i + K_i{\xi_i}^2 B2_i + K_i\Big(\frac{\cosh\xi_i}{\xi_i} - \sinh\xi_i\Big)B3_i + K_i\Big(\frac{\sinh\xi_i}{\xi_i} - \cosh\xi_i\Big)B4_i - \\ &-\frac{K_{i+1}}{\xi_{i+1}}B1_{i+1} - K_{i+1}{\xi_{i+1}}^2 B2_{i+1} - K_{i+1}\Big(\frac{\cosh\xi_{i+1}}{\xi_{i+1}} - \sinh\xi_{i+1}\Big)B3_{i+1} - K_{i+1}\Big(\frac{\sinh\xi_{i+1}}{\xi_{i+1}} - \cosh\xi_{i+1}\Big)B4_{i+1} = 0\end{aligned} \tag{D.105}$$

$$\begin{aligned}&-\frac{\sqrt{K_i}}{{\xi_i}^2}B1_i + 2\xi_i\sqrt{K_i}B2_i + \sqrt{K_i}\Big(\frac{\xi_i\sinh\xi_i - \cosh\xi_i}{{\xi_i}^2} - \cosh\xi_i\Big)B3_i + \sqrt{K_i}\Big(\frac{\xi_i\cosh\xi_i - \sinh\xi_i}{{\xi_i}^2} - \sinh\xi_i\Big)B4_i + \\ &+\frac{\sqrt{K_{i+1}}}{{\xi_{i+1}}^2}B1_{i+1} - 2\xi_{i+1}\sqrt{K_{i+1}}B2_{i+1} - \sqrt{K_{i+1}}\Big(\frac{\xi_{i+1}\sinh\xi_{i+1} - \cosh\xi_{i+1}}{{\xi_{i+1}}^2} - \cosh\xi_{i+1}\Big)B3_{i+1} - \\ &-\sqrt{K_{i+1}}\Big(\frac{\xi_{i+1}\cosh\xi_{i+1} - \sinh\xi_{i+1}}{{\xi_{i+1}}^2} - \sinh\xi_{i+1}\Big)B4_{i+1} = 0\end{aligned} \tag{D.106}$$

$$\sqrt{K_i}\Big(\frac{2}{r_i{\xi_i}^2}+\frac{2}{\sqrt{K_i}{\xi_i}^3}+\frac{2\sqrt{K_i}}{\xi_i{r_i}^2}\Big)B1_i+\sqrt{K_i}\Big(\frac{2}{\sqrt{K_i}}-\frac{4\xi_i}{r_i}+\frac{2\sqrt{K_i}{\xi_i}^2}{{r_i}^2}\Big)B2_i+$$
$$+\sqrt{K_i}\Big[\frac{1}{\sqrt{K_i}}\Big(\frac{{\xi_i}^2\cosh\xi_i-2\xi_i\sinh\xi_i+2\cosh\xi_i}{{\xi_i}^3}-\sinh\xi_i\Big)-\frac{2}{r_i}\Big(\frac{\xi_i\sinh\xi_i-\cosh\xi_i}{{\xi_i}^2}-\cosh\xi_i\Big)+\frac{2\sqrt{K_i}}{{r_i}^2}\Big(\frac{\cosh\xi_i}{\xi_i}-\sinh\xi_i\Big)\Big]B3_i+$$
$$+\sqrt{K_i}\Big[\frac{1}{\sqrt{K_i}}\Big(\frac{{\xi_i}^2\sinh\xi_i-2\xi_i\cosh\xi_i+2\sinh\xi_i}{{\xi_i}^3}-\cosh\xi_i\Big)-\frac{2}{r_i}\Big(\frac{\xi_i\cosh\xi_i-\sinh\xi_i}{{\xi_i}^2}-\sinh\xi_i\Big)+\frac{2\sqrt{K_i}}{{r_i}^2}\Big(\frac{\sinh\xi_i}{\xi_i}-\cosh\xi_i\Big)\Big]B4_i-$$
$$-\sqrt{K_{i+1}}\Big(\frac{2}{r_{i+1}{\xi_{i+1}}^2}+\frac{2}{\sqrt{K_{i+1}}{\xi_{i+1}}^3}+\frac{2\sqrt{K_{i+1}}}{\xi_{i+1}{r_{i+1}}^2}\Big)B1_{i+1}-\sqrt{K_{i+1}}\Big(\frac{2}{\sqrt{K_{i+1}}}-\frac{4\xi_{i+1}}{r_{i+1}}+\frac{2\sqrt{K_{i+1}}{\xi_{i+1}}^2}{{r_{i+1}}^2}\Big)B2_{i+1}-$$
$$-\sqrt{K_{i+1}}\Big[\frac{1}{\sqrt{K_{i+1}}}\Big(\frac{{\xi_{i+1}}^2\cosh\xi_{i+1}-2\xi_{i+1}\sinh\xi_{i+1}+2\cosh\xi_{i+1}}{{\xi_{i+1}}^3}-\sinh\xi_{i+1}\Big)-\frac{2}{r_{i+1}}\Big(\frac{\xi_{i+1}\sinh\xi_{i+1}-\cosh\xi_{i+1}}{{\xi_{i+1}}^2}-\cosh\xi_{i+1}\Big)+$$
$$+\frac{2\sqrt{K_{i+1}}}{{r_{i+1}}^2}\Big(\frac{\cosh\xi_{i+1}}{\xi_{i+1}}-\sinh\xi_{i+1}\Big)\Big]B3_{i+1}-$$
$$-\sqrt{K_{i+1}}\Big[\frac{1}{\sqrt{K_{i+1}}}\Big(\frac{{\xi_{i+1}}^2\sinh\xi_{i+1}-2\xi_{i+1}\cosh\xi_{i+1}+2\sinh\xi_{i+1}}{{\xi_{i+1}}^3}-\cosh\xi_{i+1}\Big)-\frac{2}{r_{i+1}}\Big(\frac{\xi_{i+1}\cosh\xi_{i+1}-\sinh\xi_{i+1}}{{\xi_{i+1}}^2}-\sinh\xi_{i+1}\Big)+$$
$$+\frac{2\sqrt{K_{i+1}}}{{r_{i+1}}^2}\Big(\frac{\sinh\xi_{i+1}}{\xi_{i+1}}-\cosh\xi_{i+1}\Big)\Big]B4_{i+1}=0 \tag{D.107}$$

$$K_i\Big(-\frac{2}{\xi_i r_i}-\frac{1}{\sqrt{K_i}{\xi_i}^2}\Big)B1_i+K_i\Big(\frac{2\xi_i}{\sqrt{K_i}}-\frac{2{\xi_i}^2}{r_i}\Big)B2_i+K_i\Big[\frac{1}{\sqrt{K_i}}\Big(\frac{\xi_i\sinh\xi_i-\cosh\xi_i}{{\xi_i}^2}-\cosh\xi_i\Big)-\frac{2}{r_i}\Big(\frac{\cosh\xi_i}{\xi_i}-\sinh\xi_i\Big)\Big]B3_i+$$
$$+K_i\Big[\frac{1}{\sqrt{K_i}}\Big(\frac{\xi_i\cosh\xi_i-\sinh\xi_i}{{\xi_i}^2}-\sinh\xi_i\Big)-\frac{2}{r_i}\Big(\frac{\sinh\xi_i}{\xi_i}-\cosh\xi_i\Big)\Big]B4_i+K_{i+1}\Big(\frac{2}{\xi_{i+1}r_{i+1}}+\frac{1}{\sqrt{K_{i+1}}{\xi_{i+1}}^2}\Big)B1_{i+1}-$$
$$-K_{i+1}\Big(\frac{2\xi_{i+1}}{\sqrt{K_{i+1}}}-\frac{2{\xi_{i+1}}^2}{r_{i+1}}\Big)B2_{i+1}-K_{i+1}\Big[\frac{1}{\sqrt{K_{i+1}}}\Big(\frac{\xi_{i+1}\sinh\xi_{i+1}-\cosh\xi_{i+1}}{{\xi_{i+1}}^2}-\cosh\xi_{i+1}\Big)-\frac{2}{r_{i+1}}\Big(\frac{\cosh\xi_{i+1}}{\xi_{i+1}}-\sinh\xi_{i+}\Big)\Big]B3_{i+1}-$$
$$-K_{i+1}\Big[\frac{1}{\sqrt{K_{i+1}}}\Big(\frac{\xi_{i+1}\cosh\xi_{i+1}-\sinh\xi_{i+1}}{{\xi_{i+1}}^2}-\sinh\xi_{i+1}\Big)-\frac{2}{r_{i+1}}\Big(\frac{\sinh\xi_{i+1}}{\xi_{i+1}}-\cosh\xi_{i+1}\Big)\Big]B4_{i+1}=0 \tag{D.108}$$

$$\frac{1}{\xi_n}B1_n+{\xi_n}^2B2_n+\Big(\frac{\cosh\xi_n}{\xi_n}-\sinh\xi_n\Big)B3_n+\Big(\frac{\sinh\xi_n}{\xi_n}-\cosh\xi_n\Big)B4_n-\frac{1}{\xi_n}A1-\xi_nA2={\xi_n}^2 \tag{D.109}$$

$$-\frac{1}{{\xi_n}^2}B1_n+2\xi_nB2_n+\Big(\frac{\xi_n\sinh\xi_n-\cosh\xi_n}{{\xi_n}^2}-\cosh\xi_n\Big)B3_n+\Big(\frac{\xi_n\cosh\xi_n-\sinh\xi_n}{{\xi_n}^2}-\sinh\xi_n\Big)B4_n+\frac{1}{{\xi_n}^2}A1+A2=-2\xi_n \tag{D.110}$$

$$\Big(-\frac{2}{\xi_nR_{out}}-\frac{1}{\sqrt{K_n}{\xi_n}^2}\Big)B1_n+\Big(\frac{2\xi_n}{\sqrt{K_n}}-\frac{2{\xi_n}^2}{R_{out}}\Big)B2_n+\Big[\frac{1}{\sqrt{K_n}}\Big(\frac{\xi_n\sinh\xi_n-\cosh\xi_n}{{\xi_n}^2}-\cosh\xi_n\Big)-\frac{2}{R_{out}}\Big(\frac{\cosh\xi_n}{\xi_n}-\sinh\xi_n\Big)\Big]B3_n+$$
$$+\Big[\frac{1}{\sqrt{K_n}}\Big(\frac{\xi_n\cosh\xi_n-\sinh\xi_n}{{\xi_n}^2}-\sinh\xi_n\Big)-\frac{2}{R_{out}}\Big(\frac{\sinh\xi_n}{\xi_n}-\cosh\xi_n\Big)\Big]B4_n+\Big(\frac{2}{R_{out}\xi_n}+\frac{1}{{\xi_n}^2\sqrt{K_n}}\Big)A1+\Big(\frac{2\xi_n}{R_{out}}-\frac{1}{\sqrt{K_n}}\Big)A2=$$
$$\frac{2\xi_n}{\sqrt{K_n}}-\frac{2{\xi_n}^2}{R_{out}} \tag{D.111}$$

$$\sqrt{K_n}\Big(\frac{2}{R_{out}{\xi_n}^2}+\frac{2}{\sqrt{K_n}{\xi_n}^3}+\frac{2\sqrt{K_n}}{\xi_n{R_{out}}^2}\Big)B1_n+\sqrt{K_n}\Big(\frac{2}{\sqrt{K_n}}-\frac{4\xi_n}{R_{out}}+\frac{2\sqrt{K_n}{\xi_n}^2}{{R_{out}}^2}\Big)B2_n+$$
$$+\sqrt{K_n}\Big[\frac{1}{\sqrt{K_n}}\Big(\frac{{\xi_n}^2\cosh\xi_n-2\xi_n\sinh\xi_n+2\cosh\xi_n}{{\xi_n}^3}-\sinh\xi_n\Big)-\frac{2}{R_{out}}\Big(\frac{\xi_n\sinh\xi_n-\cosh\xi_n}{{\xi_n}^2}-\cosh\xi_n\Big)+$$
$$+\frac{2\sqrt{K_n}}{{R_{out}}^2}\Big(\frac{\cosh\xi_n}{\xi_n}-\sinh\xi_n\Big)\Big]B3_n+\sqrt{K_n}\Big[\frac{1}{\sqrt{K_n}}\Big(\frac{{\xi_n}^2\sinh\xi_n-2\xi_n\cosh\xi_n+2\sinh\xi_n}{{\xi_n}^3}-\cosh\xi_n\Big)-$$
$$-\frac{2}{R_{out}}\Big(\frac{\xi_n\cosh\xi_n-\sinh\xi_n}{{\xi_n}^2}-\sinh\xi_n\Big)+\frac{2\sqrt{K_n}}{{R_{out}}^2}\Big(\frac{\sinh\xi_n}{\xi_n}-\cosh\xi_n\Big)\Big]B4_n-\Big(\frac{2\sqrt{K_n}}{{R_{out}}^2\xi_n}+\frac{2}{R_{out}{\xi_n}^2}+\frac{2}{{R_{out}}^3\sqrt{K_n}}\Big)A1-$$
$$-\Big(\frac{2\xi_n\sqrt{K_n}}{{R_{out}}^2}-\frac{2}{R_{out}}\Big)A2=\frac{2{\xi_n}^2\sqrt{K_n}}{{R_{out}}^2}+\frac{2}{\sqrt{K_n}}-\frac{4\xi_n}{R_{out}} \tag{D.112}$$

Bibliography

[1] B. B. Mandelbrot. How long is the coast of great britain, statistical self similarity and fractional dimension. *Science*, 155, 1967.

[2] B. B. Mandelbrot. *Les Objets Fractals: Forme, Hasard et Dimension*. Flammarion, Paris, 1975.

[3] Emma Carberry. Introduction to dynamical systems.

[4] B. B. Mandelbrot. *The Fractal Geometry of Nature*. W.H. Freeman and Company, New York, 1983.

[5] K. Wilkinson, S. Stoll, and J. Buffle. Characterization of nom-colloid aggregates in surface waters: Coupling transmission electron microscopy staining techniques and mathematical modelling. *Fresenius J. Anal. Chem*, 351:54–61, 1995.

[6] S. Stoll and J. Buffle. Computer simulation of bridging flocculation processes: The role of colloid to polymer concentration ratio on aggregation kinetics. *J.Colloid Interface Sci*, 205:290–306, 1998.

[7] H. J. V. Tyrell and K. R. Harris. *Diffusion in Liquids*. Butterworths, London, 1984.

[8] P. Meakin. Fractal aggregates. *Adv.Colloid Interface Sci*, 28(4):249–282, 1988.

[9] Greame Bushell. *Primary particle polydispersity in fractal aggregates*. PhD thesis, The University of New South Wales, 1998.

[10] C. M. Sorensen and G. C. Roberts. The prefactor of fractal aggregates. *J.Colloid Interface Sci*, 186:447–452, 1997.

[11] R. Jullien and R. Botet. *Aggregation and Fractal Aggregates*. World Scientific, 1987.

[12] T. A. Witten and L. M. Sander. Diffusion-limited aggregation, a kinetic critical phenomenon. *Phys.Rev.Lett*, 47(19):1400–1403, 1981.

[13] M. Kolb, R. Botet, and R. Jullien. Scaling of kinetically growing clusters. *Phys.Rev.Lett*, 51(13):1123–1126, 1983.

[14] P. Meakin. Formation of fractal clusters and networks by irreversible diffusion-limited aggregation. *Phys.Rev.Lett*, 51(13):1119–1122, 1983.

[15] S. Stoll. Computer simulation of colloid/polymer mixtures and aggregate formation. In *Proceedings of The Society for Computer Simulation International on Environmental Modeling and Simulation*, pages 35–40, Jan 2000.

[16] J. G. Kirkwood and J. Riseman. The intrinsic viscosities and diffusion constants of flexible macromolecules in solution. *J.Chem.Phys*, 16(6):565–573, 1948.

[17] V. Bloomfield, W. O. Dalton, and K. E. Van Holde. Frictional coefficients of multisubunit structures. i. theory. *Biopolymers*, 5(2):135–148, 1967.

[18] M. Lattuada, H. Wu, and M. Morbidelli. Hydrodynamic radius of fractal clusters. *J.Colloid Interface Sci*, 268:96–105, 2003.

[19] Z. Chen, J.M.Deutch, and P. Meakin. Translational friction coefficient of diffusion limited aggregates. *J.Chem.Phys*, 80(6):2982–2983, 1983.

[20] Beatriz Carrasco and Jose Garcia de la Torree. Hydrodynamic properties of rigid particles: Comparison of different modeling and computational proceduresan. *Biophysical Journal*, 75(3044):3057, 1999.

[21] Wim VAN SAARLOOS. On the hydrodynamic radius of fractal aggregates. *Physica*, 147A:280–296, 1987.

[22] P. Wiltzius. Hydrodynamics behavior of fractal aggregates. *Phys.Rev.Lett*, 58(7):710–713, 1987.

[23] W. Hess, H. L. Frisch, and R. Klein. On the hydrodynamic behavior of colloidal aggregates. *Z.Phys. B - Condensed Matter*, 64:65–67, 1986.

[24] Z. Chen, P. Meakin, and J. M. Deutch. Comment on hydrodynamic behavior of fractal aggregates. *Phys.Rev.Lett*, 59(18):2121, 1987.

[25] Z. Chen and P.C Weakliem. Hydrodynamic radii of diffusion-limited aggregates and bond-percolation clusters. *J.Chem.Phys*, 89(9):5887–5889, 1988.

[26] Z.Y.Chen, J.M.Deutch, and P.Meakin. Translational friction coefficient of diffusion limited aggregates. *J.Chem.Phys*, 80(6):2982–2983, 1984.

[27] S.N.Rogak and R.C.Flagan. Stokes drag on self-similar clusters of spheres. *J.Colloid Interface Sci*, 134:206–218, 1990.

[28] S.Chellam and M.R.Wiesner. Research note: Fluid mechanics and fractal aggregates. *Wat.Res*, 27(9):1493–1496, 1993.

[29] P.B.Warren. Hydrodynamics of fractal aggregates. *Il Nuovo Cimento*, 16 D(8):1231–1236, 1994.

[30] S.Veerapaneni and M.R.Wiesner. Hydrodynamics of fractal aggregates with radially varying permeability. *J.Colloid Interface Sci*, 177:45–57, 1996.

[31] Lech Gmachowski. Hydrodynamics of aggregated media. *J.Colloid Interface Sci*, 178:80–86, 1996.

[32] M.Vanni. Creeping flow over spherical permeable aggregates. *Chemical Engineering Science*, 55:685–698, 2000.

[33] A.V.Filippov. Drag and torque on clusters of n arbitrary spheres at low reynolds number. *J.Colloid Interface Sci*, 229:184–195, 2000.

[34] A.S.Kim and R.Yuan. Hydrodynamics of an ideal aggregate with quadratically increasing permeability. *J.Colloid Interface Sci*, 285(2):627–633, 2005.

[35] H. C. Brinkman. A calculation of the viscous force exerted by a flowing fluid on a dense swarm of particles. *Appl.Sci.Res*, 1(1), 1949.

[36] G. Ooms, P. F. Mijnlieff, and H. L. Beckers. Frictional force exerted by a flowing fluid on a permeable particle, with particular reference to polymer coils. *J.Chem.Phys*, 53(11), 1970.

[37] G. Neale, N. Epstein, and W. Nader. Creeping flow relative to permeable spheres. *Chemical Engineering Science*, 28, 1973.

[38] J. H. Masliyah, G. Neale, K. Malysa, and T. G. M. van de Ven. Creeping flow over a composite sphere: solid core with porous shell. *Chemical Engineering Science*, 42(2), 1987.

[39] B. S. Bhatt and N. C. Sacheti. Flow past a porous spherical shell using the brinkman model. *J. Phys. D: Appl. Phys.*, 27, 1994.

[40] J. Happel. Viscous flow in multiparticle systems: Slow motion of fluids relative to beds of spherical particles. *AIChE J*, 4:197–201, 1958.

[41] P. M. Adler. Hydrodynamic properties of fractal flocs. *Faraday Discuss.Chem.Soc*, 83:145–152, 1983.

[42] A. Adrover and M. Giona. Hydrodynamic properties of fractal: application of lattice boltzmann equation to tranverse flow past an array of fractal objects. *Int.J.Multiphase Flow*, 23(1):25–35, 1999.

[43] D. Coelho, J.-F. Thovert, R. Thouy, and P. M. Adler. Hydrodynamic drag on suspensions of fractal aggregates. *Fractals [Complex Geometry, Patterns, and Scaling in Nature and Society]*, 5(3):507–522, 1996.

[44] C. Binder, C. Freichtinger, H-J. Schmid, N. Thurey, W. Peukert, and U. Rude. Simulation of the hydrodynamic drag of aggregated particles. *J.Colloid Interface Sci*, 301:155–167, 2006.

[45] P.N.Pusey, J.G.Rarity, R.Klein, and D.A.Weitz. Comment on hydrodynamic behavior of fractal aggregates. *Physical Review Letters*, 59(18):2122, 1987.

[46] Y. H. Rim and K. Nahm. Hydrodynamic behavior of colloidal aggregates. *Journal of the Korean Physical Society*, 25(6):580–583, 1992.

[47] G. M. Wang and C. M. Sorensen. Diffusive mobility of fractal aggregates over the entire knudsen number range. *Phys. Rev. E*, 60(3):3036–3044, 1999.

[48] C. P. Johnson, X. Li, and B. E. Logan. Settling velocities of fractal aggregates. *Environ.Sci.Technol*, 30:1911–1918, 1996.

[49] R. Zwangzig, J. Kiefer, and G. H. Weiss. On the validity of the kirkwood riseman theory. In *proceedings of the National Academy of Sciences of the United States of America*, volume 60, pages 381–386, 1968.

[50] E. M. Lifshitz and L. D. Landau. *Fluid Mechanics*. Butterworth-Heinemann, 1987.

[51] D. J. Tritton. *Physical Fluid Dynamics*. Clarendon Press, 1988.

[52] JR John D. Anderson. *Computational Fluid Dynamics: The Basics with Applications*. McGraw-Hill, Inc., 1995.

[53] Batien Chopard and Michel Droz. *Cellular Automata Modeling of Physical Systems*. Cambridge University Press, 1998.

[54] Sauro Succi. *The Lattice Boltzmann Equation for Fluid Dynamics and Beyond*. Oxford University Press, 2001.

[55] Y. H. Qian, S. Succi, and S. A. Orszag. Recent Advances in Lattice Boltzmann Computing. *Annu. Rev. Fluid Mech*, 3:195–242, 1995.

[56] Shiyi Chen and Gary D. Doolean. Lattice Boltzmann Method For Fluid Flows. *Annu. Rev. Fluid Mech*, 30:329–364, 1998.

[57] B. Chopard, A. Dupuis, A. Masselot, and P. Luthi. Cellular Automata and Lattice Boltzmann techniques: An approach to model and simulate complex systems. *Advances in Complex Systems*, 5:103–246, 2002.

[58] J. Hardy, Y. Pomeau, and O. de Pazzis. Time evolution of a two-dimensional model system. I. Invariant states and time correlation functions. *J. Math. Phys*, 14(12):1746–1759, 1973.

[59] Alexandre Dupuis. *From a Lattice Boltzmann model to a parallel and reusable implementation of a virtual river*. PhD thesis, University of Geneva, 2002.

[60] U. Frisch, B. Hasslacher, and Y. Pomeau. Lattice-Gas Automata for the Navier-Stokes Equation. *Phys. Rev. Lett*, 56(14):1505–1508, 1986.

[61] F. Higuera, J. Jimenez, and S. Succi. Boltzmann approach to lattice gas simulations. *Europhys. Lett*, 9:663, 1989.

[62] F. Higuera, J. Jimenez, and S. Succi. Lattice Gas dynamics with enhanced collision. *Europhys. Lett*, 9:345, 1989.

[63] Y. Qian, D. d'Humières, and P. Lallemand. Lattice BGK models for Navier-Stokes equation. *Europhys. Lett*, 17:470–84, 1992.

[64] B. Chopard, A. Masselot, and M. Droz. Multiparticle Lattice Gas for a Fluid: Application to Ballistic Annihilation. *Phys. Rev. Lett*, 81(9):1845–1848, 1998.

[65] H. Chen, S. Chen, and W. H. Matthaeus. Recovery of the Navier-Stokes equations using a Lattice-Gas Boltzmann method. *Phys. Rev. A*, 45(8):R5339–R5342, 1992.

[66] M. B. Reider and J. D. Sterling. Accuracy of Discrete-Velocity BGK models for the simulation of the incompressible Navier-Stokes equations. *Comput. fluids*, 24(4):459–467, 1995.

[67] Z. Guo, C. Zheng, and B. Shi. Discrete lattice effects on the forcing term in the lattice boltzmann method. *Phys. Rev. E*, 65(4):046308, 2002.

[68] X. He, Q. Zu, L.-S. Luo, and M. Dembo. Analytic solutions of simple flows and analysis of nonslip boundary conditions for the lattice boltzmann bgk model. *J. Stat. Phys*, 87(1-2):115–136, 1997.

[69] P. A. Skordos. Initial and boundary conditions for the lattice boltzmann method. *Phys. Rev. E*, 48(6):4823 – 4842, 1993.

[70] T. Inamuro, M. Yoshino, and F. Ogino. A non-slip boundary condition for lattice boltzmann simulations. *Phys. Fluids*, 7(12):2928–2930, 1995.

[71] B. Chopard and A. Dupuis. A mass conserving boundary condition for lattice boltzmann models. *International Journal of Modern Physics B*, 17(01-02):103–107, 2003.

[72] R. Mei, L.-S. Luo, and W. Shyy. An accurate curved boundary treatment in the lattice boltzmann method. *Journal of Computational Physics*, 155(2):307 – 330, 1999.

[73] M. A. Gallivan, D. R. Noble, J. G. Georgiadis, and R. O. Buckius. An evaluation of the bounce-back boundary condition for lattice boltzmann simulations. *International Journal for Numerical Methods in Fluids*, 25:249–263, 1997.

[74] R. Mei, W. Shyy, D. Yu, and Li-Shi Luo. Lattice boltzmann method for 3-d flows with curved boundary. *Journal of Computational Physics*, 161(2):680–699, 2000.

[75] P. Lallemand and L.-S. Luo. Lattice boltzmann method for moving boundaries. *Journal of Computational Physics*, 184(2):406–421, 2003.

[76] D. Kandhai, A. Koponen, A. Hoekstra, M. Kataja, J. Timonen, and P. M. Sloot. Implementation aspects of 3d lattice-bgk: Boundaries, accuracy, and a new fast relaxation method. *J. Stat. Phys*, 150:482–501, 1999.

[77] Robert W. Fox, Alan T. McDonald, and Philip J. Pritchard. *Introduction to Fluid Mechanics*. Wiley, 1999.

[78] J. M. Buick and C. A. Greated. Gravity in a lattice boltzmann model. *Phys. Rev. E*, 61(5):5307 – 5320, 2000.

[79] S. Hou, Q. Zou, S. Chen, G. Doolen, and A. C. Cogley. Simulation of Cavity Flow by the Lattice Boltzmann Method. *J. Stat. Phys*, 118(2):329–347, 1995.

[80] A.S.Sangani and A.Acrivos. Slow flow past periodic array of cylinders with application to heat transfer. *Int.J.Multiphase Flow*, 8(3):193–206, 1982.

[81] M. Rohde, J. J. Derksen, and H. E. A. Van den Akker. Volumetric method for calculating the flow around moving objects in lattice-boltzmann schemes. *Phys. Rev. E*, 65(5):056701, 2002.

[82] H. Hasimoto. On the periodic fundamental solutions of the stokes equations and their application to viscous flow past a cubic array of spheres. *J. Fluid Mech*, 5:317–328, 1959.

[83] A.S.Sangani and A.Acrivos. Slow flow through a periodic array of sphere. *Int.J.Multiphase Flow*, 8(4):343–360, 1982.

[84] G. Ooms, P.F.Mijinlieff, and H.L.Beckers. Frictional force exerted by a flowing fluid on a permeable particle, with a particular reference to polymer coils. *J.Chem.Phys*, 53(11):4123–4130, 1970.

[85] J.H.Masliyah, G.Neale, K.Malysa, and Theodorus G.M.Van de ven. Creeping flow over a composite sphere: solid core with porous shell. *J.Chem.Eng*, 42(2):245–253, 1987.

[86] H. C. Brinkman. A calculation of the viscous force exterted by a flowing fluid on a dense swarm of particles. *Applied Scientific Research*, 1(1):27–34, 1949.

[87] L. Durlofsky and J.F. Brady. Analysis of the brinkman equation as a model for flow in porous media. *Physics of Fluid*, 30(11):3329–3341, 1987.

[88] A.S.Kim and R.Yuan. A new model for calculating specific resistance of aggregated colloidal cake layers in membrane filtration processes. *Journal of Membrane Science*, 249:89–101, 2005.

[89] H. C. Brinkman. On the permeability of media consisting of closely packed porous particles. *Appl.Sci.Res*, 1(1), 1949.

[90] L. Durlofsky and J. F. Brady. Analysis of the brinkman equation as a model for flow in porous media. *Phys.Fluids*, 30(11), 1987.

[91] Dieter A. Wolf-Gladrow. *Lattice-Gas Cellular Automata and Lattice Boltzmann Models: An Introduction*. Springer, 2000.

[92] Xiaoyi He and Li-Shi Luo. Lattice Boltzmann Model for the Impressible Navier-Stokes Equation. *J. Stat. Phys*, 88:927–944, 1997.

[93] D. Ziegler. Boundary conditions for lattice boltzmann simulations. *J. Stat. Phys*, 71(5-6):1171–1177, 1993.